

1994

Polarization transfer coefficient measurements in the deuteron breakup reaction hydrogen-1(polarized deuteron,polarized proton)X at 2.1 GeV

Naipor Eric Cheung
College of William & Mary - Arts & Sciences

Follow this and additional works at: <https://scholarworks.wm.edu/etd>



Part of the [Physics Commons](#)

Recommended Citation

Cheung, Naipor Eric, "Polarization transfer coefficient measurements in the deuteron breakup reaction hydrogen-1(polarized deuteron,polarized proton)X at 2.1 GeV" (1994). *Dissertations, Theses, and Masters Projects*. Paper 1539623846.

<https://dx.doi.org/doi:10.21220/s2-by3q-es73>

This Dissertation is brought to you for free and open access by the Theses, Dissertations, & Master Projects at W&M ScholarWorks. It has been accepted for inclusion in Dissertations, Theses, and Masters Projects by an authorized administrator of W&M ScholarWorks. For more information, please contact scholarworks@wm.edu.

INFORMATION TO USERS

This manuscript has been reproduced from the microfilm master. UMI films the text directly from the original or copy submitted. Thus, some thesis and dissertation copies are in typewriter face, while others may be from any type of computer printer.

The quality of this reproduction is dependent upon the quality of the copy submitted. Broken or indistinct print, colored or poor quality illustrations and photographs, print bleedthrough, substandard margins, and improper alignment can adversely affect reproduction.

In the unlikely event that the author did not send UMI a complete manuscript and there are missing pages, these will be noted. Also, if unauthorized copyright material had to be removed, a note will indicate the deletion.

Oversize materials (e.g., maps, drawings, charts) are reproduced by sectioning the original, beginning at the upper left-hand corner and continuing from left to right in equal sections with small overlaps. Each original is also photographed in one exposure and is included in reduced form at the back of the book.

Photographs included in the original manuscript have been reproduced xerographically in this copy. Higher quality 6" x 9" black and white photographic prints are available for any photographs or illustrations appearing in this copy for an additional charge. Contact UMI directly to order.

U·M·I

University Microfilms International
A Bell & Howell Information Company
300 North Zeeb Road, Ann Arbor, MI 48106-1346 USA
313/761-4700 800/521-0600



Order Number 9433580

**Polarization transfer coefficient measurements in the deuteron
breakup reaction $^1\text{H}(\vec{d}, \vec{p})\text{X}$ at 2.1 GeV**

Cheung, Naipor Eric, Ph.D.

The College of William and Mary, 1994

U·M·I
300 N. Zeeb Rd.
Ann Arbor, MI 48106



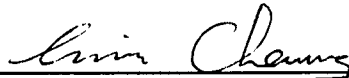
POLARIZATION TRANSFER COEFFICIENT MEASUREMENTS
IN THE DEUTERON BREAKUP REACTION ${}^1\text{H}(\vec{d}, \vec{p})\text{X}$
AT 2.1 GEV

A Dissertation
Presented to
The Faculty of the Physics Department
The College of William and Mary in Virginia

in Partial Fulfillment
of the Requirements for the Degree of
Doctor of Philosophy

by
Naipor E. Cheung
February 1994

This dissertation is submitted in partial fulfillment of
the requirements for the degree of
Doctor of Philosophy



Naipor E. Cheung

Approved, February 1994



C.F. Perdrisat



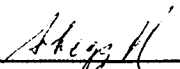
H.O. Funsten



W.J. Kossler



F.L. Gross



R. Abegg
TRIUMF

Table of Contents

Acknowledgements	v
List of Tables	vi
List of Figures	vii
Abstract	x
1 Introduction	2
2 Experimental Set-up	9
2.1 Accelerator	10
2.1.1 Ion sources	10
2.1.2 Injectors	14
2.1.3 Synchrotron	14
2.2 Spectrometer	15
2.3 Polarimeter	19
2.4 POMME calibration	22
2.5 Deuteron Beam Polarimeter	23
2.6 Electronics	27
2.6.1 SPES4	27
2.6.2 POMME	28
2.7 Data Acquisition	30
3 Data Analysis	33
3.1 Data Structure	33

3.2	POMME	34
3.3	SPES4	42
3.4	Event Selection	46
3.4.1	On-line	46
3.4.2	Off-line	47
3.5	Fourier Analysis	57
3.6	Polarimeter Calibration	61
3.7	Polarization Transfer	67
3.7.1	Proton Polarization	67
3.7.2	Polarization Transfer Coefficient	71
4	Results and Discussion	76
4.1	Non-relativistic Deuteron Wave Function	76
4.2	Proton Spectator Approximation	78
4.3	Interpretations	83
4.3.1	Non-relativistic view	83
4.3.2	Relativistic Effect	95
4.4	Conclusion	104
A	The Madison Convention	109
B	Dead-time correction for the deuteron beam polarimeter	118
	References	122
	VITA	125

Acknowledgements

I would like to thank my advisor, Charles Perdrisat, for his guidance throughout my graduate career in Physics. I appreciated his mastery of the art of experimental physics and his physical insights. I am forever indebted to him for all that he taught me, and the time he spent with me.

I also like to thank my collaborators on SATURNE experiment EXP202, whose enthusiasm made the experiment so successful. Special thanks go to Rainer Siebert, Jacques Yonnet and Michel Boivin, who explained all the hardware and software of the experiment to me patiently; to Rudolf Abegg and Egle Tomasi-Gustafsson for their genuine care and friendship.

I am grateful for the helps of Christopher Lyndon and Rahman Pourang, who answered all my questions about computers. I also enjoyed all those fruitful discussions I had with Vina Punjabi and Charles during the data analysis.

I am very thankful to Herbert Funsten, William Kossler, Franz Gross, Charles and Rudolf for reading the manuscript, and for their helpful comments. A big thank to Herbert, who showed me the first taste of experimental physics and all its fun. Further, I thank the entire Physics Department for providing a stimulating scientific and intellectual environment.

A very special thanks to all my friends here, especially Tak Yan Tse, David Garren, Douglas Baker, Jon Gotze, Alan Greer and Harris Hoke, for the many good times we have had. I would like to express my deepest appreciation to my parents for their encouragement and unconditional love. Finally, I acknowledge my wife, Meiyee, for her sacrifice and understanding on those days; but most importantly I thank her for her daily help and encouragement, and for her love.

List of Tables

1-1	Main properties of deuteron.	3
2-1	The p/z SPES4 settings and the experimental conditions for the eight data points.	19
2-2	The p/z SPES4 settings during the POMME calibration.	23
3-1	The z -coordinates of the chambers from a fixed reference point.	38
3-2	The geometrical offset parameters for the chambers.	40
3-3	The transport coefficients of SPES4.	45
3-4	The number of rejections by individual tests and cuts for every hundred proton-events.	54
3-5	The proton polarization measured at the two extraction ports, SD2 and SD3, during the double extraction verification procedure.	61
3-6	The measured proton beam polarization during the POMME calibration.	61
3-7	The 124 point data base used for the proton-carbon analyzing power parameterization.	62
3-8	The parameters for the analytical fit of the pC analyzing power.	63
3-9	The figure of merit of POMME and the estimated statistical uncertainty of the measured proton polarization.	67
3-10	The measured proton polarization for each data point.	71
3-11	Asymmetry measurements from the Deuteron Beam Polarimeter.	72
3-12	Polarization transfer coefficient, κ_o	74
4-1	Polarization transfer coefficient for different values of q	83
A-1	Comparison of ϕ between the Madison Convention and the usual spherical coordinates.	114

List of Figures

2-1	Floor plan of Saturne II.	11
2-2	The polarized ion source Hyperion.	12
2-3	The magnetic spectrometer SPES4.	17
2-4	The target cell and collimator of SPES4.	18
2-5	The polarimeter POMME	21
2-6	The double extraction settings during the POMME calibration (a), and during the verification (b).	24
2-7	The low energy deuteron beam polarimeter.	26
2-8	The readout system of the wire chambers.	29
2-9	The structure of the event trigger.	29
2-10	Flow chart of the on-line data reduction program.	32
3-1	The position spectrum of a small chamber (a), a large chamber (b). . .	37
3-2	The deviation between the straight line and the position readout from the y -coordinate of chamber C_4	39
3-3	The spatial resolution of the small and the large chambers.	41
3-4	The TOF spectrum for the data point with $p/z = 1.75$ GeV/c (a), and the data point with $p/z = 2.61$ GeV/c (b).	44
3-5	The proton momentum spectrum of dp backward elastic scattering. . .	46
3-6	The θ -distribution of the 1% sampling events.	48
3-7	The x - and y -coordinates of the proton-carbon scattering vertex	51
3-8	The z -coordinates of the proton-carbon scattering vertex (a) and the distance of the closest approach between the trajectories in the front and the rear chambers (b).	52
3-9	The 2-dimensional histogram of Θ_T vs δ (a), and Φ_T vs δ (b).	53

3-10	The x - and y -coordinates where the particle intercepted the plane of the last wire chamber before (a) and after (b) the cone test.	55
3-11	Same histograms as figure 3-10, but with the incoming particle trajectories overlapping each other.	56
3-12	The overall fit of the data base for the pC analyzing power.	64
3-13	The pC analyzing power fit between $T_p=1.0$ and 1.8 GeV.	65
3-14	P_y and P_x of the data point with SPES4 setting of 1.75 GeV/c.	70
3-15	Measured beam vector polarization.	73
3-16	Polarization transfer coefficient, κ_o	75
4-1	Impulse approximation calculation for κ_o using the Paris wave function.	86
4-2	Impulse approximation calculation for T_{20} using the Paris wave function.	87
4-3	Impulse approximation calculation for the invariant cross section using the Paris wave function.	88
4-4	Impulse approximation predictions for κ_o and T_{20}	89
4-5	The six Feynman diagrams for the non-relativistic multiple scattering calculation.	90
4-6	Non-relativistic multiple scattering calculation for κ_o using the Paris wave function.	92
4-7	Non-relativistic multiple scattering calculation for T_{20} using the Paris wave function.	93
4-8	Relativistic impulse approximation calculation for κ_o using the Gross wave function.	98
4-9	Relativistic impulse approximation calculation for T_{20} using the Gross wave function.	99
4-10	Relativistic impulse approximation calculation for the invariant cross section using the Gross wave function.	100

4-11 A Feynman diagram with 3 vertices and its 6 corresponding time-ordered diagrams.	101
4-12 The diagrams for the infinite momentum frame (IMF) calculation.	103
4-13 Calculation for κ_0 in the infinite momentum frame, using the Paris wave function and the light cone variables.	105
4-14 Calculation for T_{20} in the infinite momentum frame, using the Paris wave function and the light cone variables.	106
4-15 Calculation for the invariant cross section in the infinite momentum frame, using the Paris wave function and the light cone variables.	107
A-1 Relationship between the projectile helicity frame (x,y,z) , the outgoing reactant helicity frame (x',y',z') and the lab. frame $(x_{lab},y_{lab},z_{lab})$	113
B-1 Ratio between the true asymmetry, ϵ , and the measured asymmetry, x_m	120

ABSTRACT

The polarization of the protons emerging at 0° from the inclusive deuteron breakup reaction $^1\text{H}(\vec{d}, \vec{p})\text{X}$ was measured using a deuteron beam with kinetic energy of 2.1 GeV. The momentum of the protons was selected by the magnetic spectrometer SPES4 and the polarization was measured with the polarimeter POMME. This experiment was performed at eight different proton momenta. When those momenta are Lorentz transformed to the deuteron rest frame, they corresponded to values from 0.00 to 0.34 GeV/c. The result of the measurements is expressed in terms of polarization transfer coefficient which is defined as the ratio of the measured proton polarization P_p to the deuteron beam vector polarization P_Z : $\kappa_o = P_p/P_Z$. The values of κ_o decreased from 0.995 to -0.320 across the proton momentum range of this experiment. The trend of κ_o is in general agreement with the expected behavior arising from the D state in the deuteron wave function. The impulse approximation predicts quite well the general shape of κ_o . Multiple scattering and relativistic effect based on different models of reaction mechanism are discussed.

POLARIZATION TRANSFER COEFFICIENT MEASUREMENTS

IN THE DEUTERON BREAKUP REACTION ${}^1\text{H}(\vec{d}, \vec{p})X$

AT 2.1 GEV

Chapter 1

Introduction

The interaction between two nucleons is one of the central questions in nuclear physics. Hans Bethe once said in a 1953 Scientific American article [Bet53] that “in the past quarter century physicists have devoted a huge amount of experimentation and mental labour to this problem – probably more man-hours than have been given to any other scientific question in the history of mankind.” Forty years after Bethe wrote these words, even more effort has been expended on the topic and some progress has been made.

The theory of nuclear physics is different from the theory of atomic physics in the sense that the principal force between the electrons and nuclei, the electromagnetic force, was well known when the theory of the atomic system got under way, and the problem was to find the proper mechanics to describe the system under the given force. Quantum mechanics is the solution to this problem. In nuclear physics, there are good reasons to believe that the concept of quantum mechanics is still the correct way to describe the system, but the forces acting between the constituent particles are still not completely understood.

In investigating the nuclear force, one crucial test of the theory is the deuteron, which is the simplest stable compound nucleus. The position of the deuteron problem in nuclear theory is similar to that of the problem of the hydrogen atom in atomic theory. It tests the theory without aggravating the computational situation which is already complicated enough for the simplest nucleus.

The deuteron, the only bound system of two nucleons, is unique in many respects. It is loosely bound and its binding energy, 1.1 MeV per nucleon, is much less than

rest mass	M_d	1 875.613 39(57)	$MeV c^{-2}$
binding energy	E_B	2.224 573 12(22)	MeV
spin and parity	J^π	1^+	
isospin	T	0	
magnetic dipole moment	μ_d	0.857 406(1)	μ_N
electric quadrupole moment	Q_d	0.285 90(30)	$e fm^2$
radius	r_d	1.963(4)	fm

Table 1-1: Main properties of deuteron.

the average value, 7-9 MeV per nucleon, in other stable nuclei. Partly because of this small binding energy, the deuteron has no bound excited state. Due to its fundamental importance, many careful and sophisticated measurements have been carried out on the deuteron. We know that the binding energy of the deuteron is 2.224 573 12(22) MeV from radiative capture of a slow neutron by hydrogen, $n + p \rightarrow \gamma + d$ [G⁺86]. Some important measured quantities of the deuteron are listed in Table 1-1 [Won90].

Since the masses of proton and neutron are so close in value, it is postulated that they are the same particle in two different quantum states. This idea was first suggested by Heisenberg [Hei32], who used the Pauli spin matrices to represent the attribute that we call isospin. Isospin was introduced originally to simplify calculations involving the interactions among protons and neutrons through nuclear forces. In the isospin formalism, the proton and neutron are treated as though they were two different quantum-mechanical states of the same entity, the nucleon. A proton is distinguished from a neutron by the value of its isospin projection quantum number, I_3 : the value $I_3 = 1/2$ is arbitrarily assigned to the proton and $I_3 = -1/2$ to the neutron. So, the proton is defined as

$$|I = \frac{1}{2}, I_3 = \frac{1}{2}\rangle \equiv p \quad (1-1)$$

and the neutron as

$$|I = \frac{1}{2}, I_3 = -\frac{1}{2}\rangle \equiv n. \quad (1-2)$$

I is the isospin. For a two-nucleon system, we have

$$\begin{aligned}
 & |I = 1, I_3 = 1 \rangle = pp \\
 \text{isospin triplet} \quad & |I = 1, I_3 = 0 \rangle = \frac{1}{\sqrt{2}}(pn + np) \\
 & |I = 1, I_3 = -1 \rangle = nn \\
 \\
 \text{isospin singlet} \quad & |I = 0, I_3 = 0 \rangle = \frac{1}{\sqrt{2}}(pn - np).
 \end{aligned} \tag{1-3}$$

Since both the pp and the nn systems are unbound and assuming that the nuclear force itself is charge independent, one concludes that the deuteron is the isospin singlet state with $I = 0$.

The slow neutron capture experiment mentioned above not only gives the deuteron binding energy, but also reveals the parity of the deuteron wave function. Because of the low energy nature of the neutrons in this reaction, the angular momentum, L , of the initial two-body state is 0. The relationship between parity and L is given by

$$\text{parity} = (-1)^L \tag{1-4}$$

This gives the initial state an even parity. The photons from this radiation capture reaction are from magnetic dipole transitions (M1) [Lev60]. This transition selects out from the photon field the part that contains one unit of angular momentum and even parity. Assuming that strong interactions conserve parity. This means that the deuteron bound state wave function must have an even parity.

Deuteron has total spin $J = 1$. In a non-relativistic picture, it is made up of a proton and a neutron. Since the nucleon has spin $1/2$, the intrinsic spin of the deuteron can only be $S = 0, 1$. One has

$$\vec{J} = \vec{L} + \vec{S}, \tag{1-5}$$

and the only possible LS combinations for the deuteron are

$$\begin{array}{ll}
 S = 0 & S = 1 \\
 L = 1 & L = 0, 1, 2.
 \end{array}$$

Since we know that the deuteron has even parity, this confines the possible values of L to even integers. In this case, L can only be 0 or 2. Thus we can conclude that the ground state of the deuteron has total angular momentum $J = 1$, intrinsic spin $S = 1$, isospin $I = 0$ and even parity. There remain, however, two possibilities of orbital angular momentum, $L=0$ and $L=2$. In spectroscopic notation, the $L=0, S=1$ state is represented as 3S_1 (S -triplet state) and the $L=2, S=1$ as 3D_1 (D -triplet state).

Let us assume $L = 0$ for the deuteron for a moment; its wave function is then spherically symmetric and the angular momentum of the nucleus is entirely attributable to the spin of the nucleons. The deuteron spin of 1 implies that the proton and the neutron spins are parallel. In such a case the magnetic moments should also add:

$$\begin{aligned} \text{proton moment} &= 2.7928 \mu_N \\ \text{neutron moment} &= -1.9130 \mu_N \\ \text{sum of the two moments} &= 0.8798 \mu_N \\ \text{deuteron moment} &= 0.8574 \mu_N \end{aligned}$$

It is seen that the deuteron moment almost agrees with the sum of the moments of proton and neutron. This suggests that the dominant part of the deuteron is the 3S_1 state. The very small but non zero electric quadrupole moment of the deuteron indicates the existence of a small component of a 3D_1 state in deuteron. This mixture of states with different orbital angular momentum signals that there is a non-central force, namely the tensor force, acting between the two nucleons. A detailed study of the deuteron nuclear structure can provide more information about the tensor force in this two body system and brings us one step closer to the understanding of the nuclear forces.

One way to study the deuteron structure is by an electromagnetic probe. The deuteron being of spin 1, its electromagnetic properties are described by three form factors: the electric monopole (or charge) G_C , the electric quadrupole G_Q and the magnetic dipole G_M form factors [BS57]. With an electron beam of a few hundreds MeV, the de Broglie wave length of the electrons is about the same size as the nuclear

dimensions of a few fm , and the nucleus no longer looks like a point particle. The charge and magnetization density distributions in the nucleus become “visible” to the incident electrons. The scattering results are sensitive to the charge and current densities inside the deuteron nucleus. All observables of the electron-deuteron scattering are bilinear combinations of the three form factors above. The determination of those quantities is among the most fundamental in nuclear physics.

Since the interaction between an electron and a nucleus is primarily electromagnetic in nature, the density distribution observed through electron scattering is predominantly the distribution of protons which carry the nuclear charge. In principle, strong interaction mechanisms can be used to deduce the nucleon distribution of both the protons and the neutrons.

A hadronic probe with momentum between 100 to 1000 MeV/c has a wave length comparable to or smaller than the size of a nucleon. At this energy, the coherent scattering from the nucleus is lost and the scattering takes place essentially from individual nucleons. The fact that the deuteron has a small binding energy, with its two nucleons spending most of their time far away from each other, also favours this quasi-elastic scattering condition. As a result, the scattering is sensitive to the nucleon density distribution.

Quasi-elastic scattering is different from elastic scattering off free nucleons. The nucleons in a nucleus are continuously moving around with respect to the nuclear center of mass and this motion is known as the Fermi motion. Hadron-deuteron scattering experiments can provide information on the single nucleon momentum distribution of a bound nucleon inside a deuteron.

No study of the deuteron structure is complete without polarization measurements and the availability of the high energy polarized deuteron beam provides one such opportunity. The simplest experiment of this kind is to measure the analyzing powers

of the polarized deuteron scattered at a target. The differential cross section depends on both the vector and tensor polarization of the beam, as well as the analyzing powers themselves. As shown in Appendix A, in general there are three vector and five tensor analyzing powers for this reaction. In terms of spherical tensor representation, they are equivalent to three first-rank tensors, T_{11}, T_{10}, T_{1-1} , and five second-rank tensors, $T_{22}, T_{21}, T_{20}, T_{2-1}, T_{2-2}$. The conservation of parity reduces their number to four, namely $T_{11}, T_{20}, T_{21}, T_{22}$. These analyzing powers can be measured experimentally by manipulating the beam polarization states. An excellent review on this subject was given by Gerald G. Ohlsen [Ohl72].

An example of this type of experiment is the scattering of a polarized deuteron from a hydrogen target and detecting the forward going protons. Both elastic ${}^1H(\vec{d}, p)d$ [P⁺93] and inelastic ${}^1H(\vec{d}, p)X$ [PP90] scattering experiments have been done. When the polarization symmetry axis is perpendicular to the beam momentum direction and the outgoing proton is measured at 0° , all analyzing powers except T_{20} vanish. The impulse approximation assumes that the measured protons predominantly come from the deuteron nuclei and are spectators of the deuteron breakup reaction. Under this assumption, the measured value of T_{20} can be expressed in terms of a ratio between the amplitudes of D and S states of the deuteron wave function as demonstrated in Chapter 4.

The next logical step is to also measure the polarization of the outgoing protons in the (\vec{d}, \vec{p}) reaction at 0° . In proton spectator assumption, the polarization transfer coefficient, κ_o , from the deuteron to the proton can also be expressed in terms of the same D/S ratio.

A series of deuteron experiments is under way both at Saclay and Dubna. It is hoped that we can collect enough information to determine in what energy region the impulse approximation description of the reaction is valid. In the region where the

proton spectator description no longer dominates, we would like to find out what other kind of reaction mechanisms contribute to the process. Such mechanisms can be final states interactions, Δ -resonances excitation or quark-gluon effects. The ultimate goal is to determine the deuteron wave function experimentally and to provide a solid testing ground for all the theories of the nuclear force.

The experiment reported in this dissertation was performed at the synchrotron Saturne II at Saclay in the Summer of 90. It consisted of two parts. The first part of the experiment was to measure the polarization transfer coefficient in the deuteron breakup reaction ${}^1H(\vec{d}, \vec{p})X$; the second part was a calibration of the proton polarimeter used in this experiment.

In Chapter 2, the details of the hardware and experimental set-up are given, especially for the polarimeter and the spectrometer. The event selection and data analysis are discussed in Chapter 3. Finally, the results and discussions are presented in Chapter 4. Two appendices are also included in this thesis. Appendix A describes the Madison Convention of notations for polarization experiments. Appendix B gives details of the dead-time correction of the deuteron beam polarimeter.

Chapter 2

Experimental Set-up

The main objective of the present experiment was to measure the vector polarization transfer coefficient, κ_o , from the deuteron to the proton in the inclusive deuteron breakup reaction on a hydrogen target, ${}^1H(\vec{d}, \vec{p})X$, at 0° . This experiment consisted of two parts. The first part was to measure the coefficient κ_o as a function of the outgoing proton energy while the second part was to calibrate the proton polarimeter used during the experiment.

For the polarization transfer experiment, a 2.1 GeV purely vector polarized deuteron beam was directed onto a 4 cm thick liquid hydrogen target. Both the momentum and the polarization of the outgoing protons were measured. The momentum of the particle was determined by the magnetic spectrometer SPES4 and the proton polarization was measured by the focal plane polarimeter POMME. The energy of the deuteron beam was fixed throughout this part of the experiment. The magnetic field of the spectrometer was set to eight different values, thus enabling us to study the breakup reaction over a range of the outgoing proton momentum.

The calibration of POMME was done right after the completion of the polarization transfer experiment. The polarimeter had been calibrated previously for proton energies between 0.5 to 1.2 GeV. We extended this range up to 1.8 GeV. Two energies, 1.6 and 1.8 GeV, were chosen for this calibration.

In the following sections of this chapter, the hardware used in this experiment is discussed in more detail. Special attention is given to the spectrometer and the polarimeter because they were the most important pieces of apparatus for this experiment. The geometry and the experimental setup are mentioned. The electronics and the data

acquisition system are shown at the end of the chapter.

2.1 Accelerator

The experiment was done at the synchrotron Saturne II which is located at the Laboratoire National Saturne (LNS) inside the Centre d'Etudes Nucléaires de Saclay (CENS), 25 km south of Paris.

The old synchrotron Saturne I at LNS was completely rebuilt into a strong focusing machine between 1974 and 1979 and became the Saturne II. The synchrophasotron (or synchrocyclotron) at the Joint Institute for Nuclear Research (JINR) at Dubna (Russia) and Saturne II at Saclay (France) are currently the only two machines in the world that can provide high energy polarized deuteron beams. The main components of Saturne are the ion sources, injectors, and a main synchrotron. The particles from the source are transported to the injector where they are accelerated to intermediate energy before being injected into the main synchrotron. The particle beam is then extracted into the experimental areas after being brought up to the required energy. The floor plan of Saturne II is given in Figure 2-1.

2.1.1 Ion sources

Saturne II has unpolarized sources for both light and heavy ions. It also has polarized sources Hyperion for both protons and deuterons, and Amalthee for heavier ions. Hyperion [A⁺88], named after a satellite of the planet Saturn, was used for this experiment. It is an atomic beam types source. It can produce either polarized proton or deuteron ions. This source was built in 1981 and began to operate in 1982.

As shown in Figure 2-2, Hyperion is made up of a dissociator, a sextupole magnet, radio-frequency cavities and an ionizer. The principle of an atomic-beam type polarized source [Nii90, Gla70] is quite simple. The dissociator produces a neutral atomic beam from the corresponding gas. The sextupoles act as a Stern-Gerlach magnet which focus

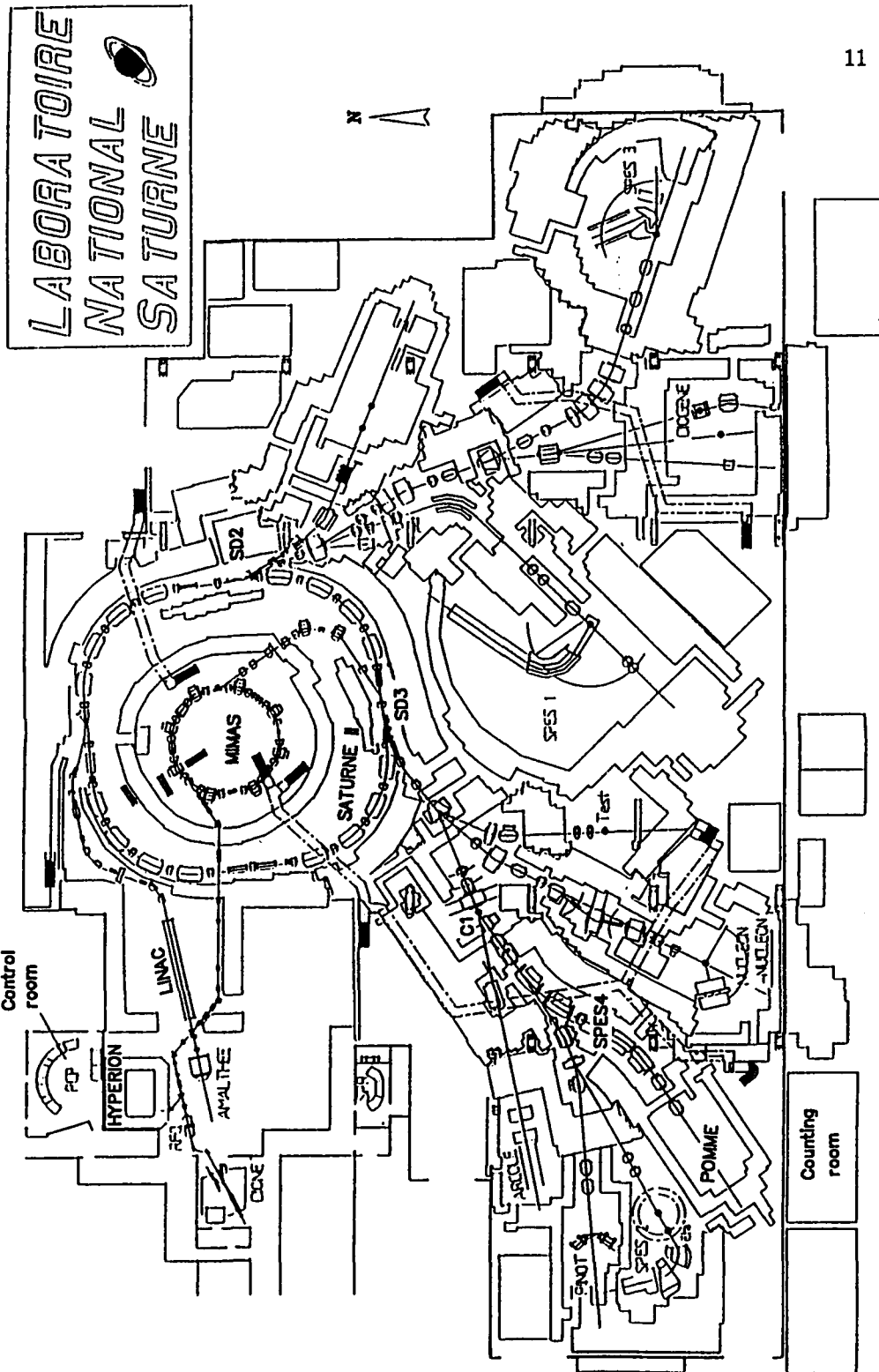


Figure 2-1: Floor plan of Saturne II.

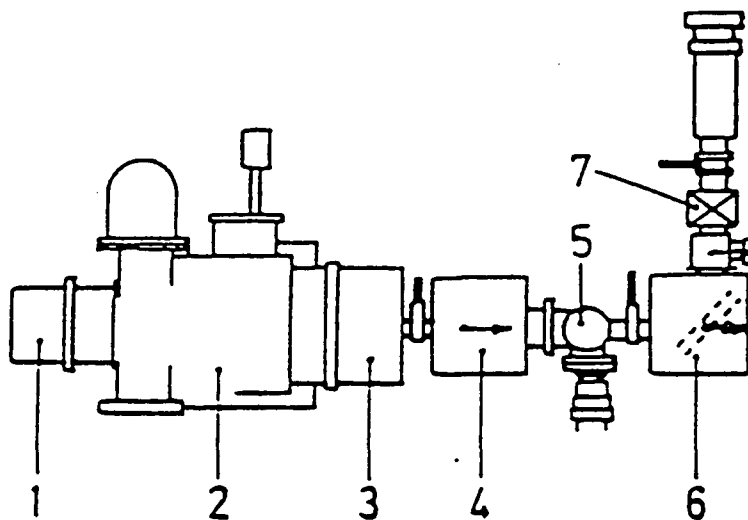


Figure 2-2: The polarized ion source Hyperion. (1) Dissociator, (2) sextupole magnet, (3) radio-frequency transitions, (4) ionizer, (5) electrostatic lenses, (6) electrostatic mirror, (7) spin rotation solenoid.

the atoms with electron spin in one direction and defocus those with electron spin in the opposite direction. The highly “electron-spin polarized” atomic beam is then transported to the RF transition cavities. The subsequent RF stimulate the hyperfine interactions [A⁺84] between different magnetic sub-states of the atom. It eventually converts the high degree of electron-spin polarization into a high degree of nuclear-spin polarization. This neutral beam is then passed through an ionizer where electrons are removed. Finally, the spin of the polarized ions is rotated to the vertical direction, by means of an electrostatic lense and a mirror followed by a solenoid, to match the magnetic field orientation inside the accelerator.

The RF dissociator of Hyperion is operated at 17 MHz [C⁺90] and the atomic jet is formed by free expansion at a gold covered copper nozzle which is cooled down to 80° K in order to achieve a high atomic beam density [Lem90]. A tapered sextupole magnet is used. Hyperion has a set of removable RF transition cavities (2 for protons and 3 for deuterons) to select the required nuclear polarization states. The whole polarized source, including the electron beam ionizer, is operated in a pulsed mode. The extracted ion beam current is of the order of a few hundred μA with a pulse length of 1.5 ms for protons and 1 ms for deuterons.

In the polarization transfer experiment, the source Hyperion was operated in a two-state mode [A⁺88] which provided a purely vector polarized deuteron beam with no tensor polarization component. Between consecutive beam spills, the spin direction of the deuterons was alternated between up and down by activating different radio-frequency cavities in the ion source. The maximum polarization of a purely vector polarized deuteron is $P_Z = \pm 2/3$. For the polarimeter calibration part of the experiment, a polarized proton beam was required. Hyperion can provide a proton beam with maximum polarization up to $P_Z = \pm 1$. The direction of the proton beam polarization was also oriented vertically and flipped up and down between beam spills. In both cases,

the efficiency of the polarized source was about 0.9. The loss of polarization is due to the presence of an unpolarized background and the inefficiency in the RF cavities.

2.1.2 Injectors

There are currently two injectors at Saturne, a linear accelerator injector Linac which had been operational since 1969, and a new mini-synchrotron injector MIMAS [C+90] which was used for this experiment.

Mimas (a satellite of Saturn and an acronym for "Machine a Intensite Maximale par Acceleration et Stockage") is an accumulator-accelerator booster that is used for the injection of both heavy ions and polarized projectiles. It has 1/3 the radius of the main synchrotron and is located at the center of the main ring. The polarized particles are captured adiabatically in Mimas and stored at 200 keV per nucleon for up to 800 μ s. The deuterons are then accelerated to 23.8 MeV and fast injected on one turn into the principal Saturne synchrotron in a single shot. Accurate matching between Hyperion and Mimas gives an 80% efficiency for capturing and accelerating of the polarized ions, while the efficiency of transferring the particles from Mimas into the synchrotron is 90%.

2.1.3 Synchrotron

A synchrotron is a ring shaped device for accelerating charged particles by the repeated passage of the particles, at essentially constant radius, through a time-varying electric field. The prefix "synchro-" refers to the synchronous nature of the acceleration process in which the beam particles are kept in phase with the oscillating accelerating voltage as they circulate in the accelerator ring. The radius of the trajectory is held constant by dipole magnets with a variable magnetic field, adjusted exactly to the increasing momentum of the beam. Quadrupole magnets, with the field increasing in the same manner, focus the particles about the central equilibrium orbit.

The main synchrotron Saturne II [Sat87] is a 100 meters circumference machine

which consists of 16 dipole bending magnets and 24 quadrupole focusing magnets. The injector Mimas transfers the particles into the nearly circular cross section vacuum chamber of the synchrotron. During each turn in the accelerator ring, particles are accelerated by two radio-frequency cavities. Position and intensity of the beam are continuously measured and adjusted during each acceleration cycle. Nearly a million turns are needed to reach the maximum energy. The beam line is always kept under a very high vacuum (5×10^{-11} HPa) to minimize the particle losses due to scattering with the gas residue.

Saturne II provides proton beams with energies between 100 MeV and 2.95 GeV, or heavy ion beams between 50 MeV and 1.15 GeV per nucleon with a precision of 10^{-3} . The stability of the energy of the extracted beams is of the order of 10^{-4} . Slow extraction systems with adjustable flux and duration are employed at the two beam extraction points of Saturne, SD2 and SD3. This extraction system has a very high efficiency and provides high intensity beams to the experimental areas.

In the polarization transfer experiment, the 2.1 GeV deuteron beam came into the experimental area every 3.95 seconds with spill duration of 500 ms. The beam intensity could be adjusted between 10^8 and 10^{11} deuterons per spill. For the second part of the experiment, the intensity of the polarized proton beam was 5×10^8 per spill in the accelerator ring before extraction. At 1.6 GeV, the beam came in every 1.7 seconds. The acceleration time increased to 2.1 seconds at 1.8 GeV. Each proton beam spill had a width of 400 ms.

2.2 Spectrometer

The magnetic spectrometer SPES4 [G^{+81} , B^{+87}] was designed to measure particles up to a rigidity p/z of 4 GeV/c, with the best possible momentum resolution of about 5×10^{-4} . Its optical design is based upon the dipole magnets of the old synchrotron yokes of Saturne I. It is a weak focusing spectrometer with four dipole bending magnets, six

quadrupole and two sextupole magnets. The total length of SPES4 is about 33 meters. Particles entering SPES4 are first bent to the left by two of the dipole magnets, and then to the right by the other two dipoles. Each dipole magnet provides a deflection of about 15° and the overall net deflection of the particles in SPES4 is zero. A detail layout of the spectrometer is shown in Figure 2-3.

The focusing of SPES4 is mostly due to the quadrupole magnets. The sextupole magnets are used to bring the normal of the final focal plane close to 0° with respect to the optical axis of SPES4. A horizontal image is formed at the intermediate focal plane (IFP) in the middle of the spectrometer. Double focusing (both vertical and horizontal) conditions are obtained at the final focal plane (FFP) at the end of SPES4. Hodoscopes I is placed at the intermediate focal plane and hodoscope F is placed 14.2 cm behind the final focal plane. The distance between I and F provides a flight path of about 16.34 meters for particle time-of-flight measurements.

The primary beam is directed from the extraction point SD3 to the target position, C1, at the front end of SPES4. A very important component of this part of the beam transport line is a moving device located upstream of the target position, which provides an adjustable incidence angle of the primary beam. With this system, the spectrometer remains in a fixed position while the scattering angle may be varied by changing the direction of the incident particles. When the target is placed at the C1 position, a dipole magnet downstream of the target is used to separate the scattered particles from the un-scattered primary beam. This makes the experiments with outgoing particles detected at 0° possible.

The 4 cm thick liquid hydrogen target, used for the polarization transfer experiment, has two thin Ti end windows. It is mounted on a ladder which could slide vertically in and out of the beam axis. This ladder is driven by a stepper motor which itself is controlled remotely by a computer in the counting room. Position C1 is located about

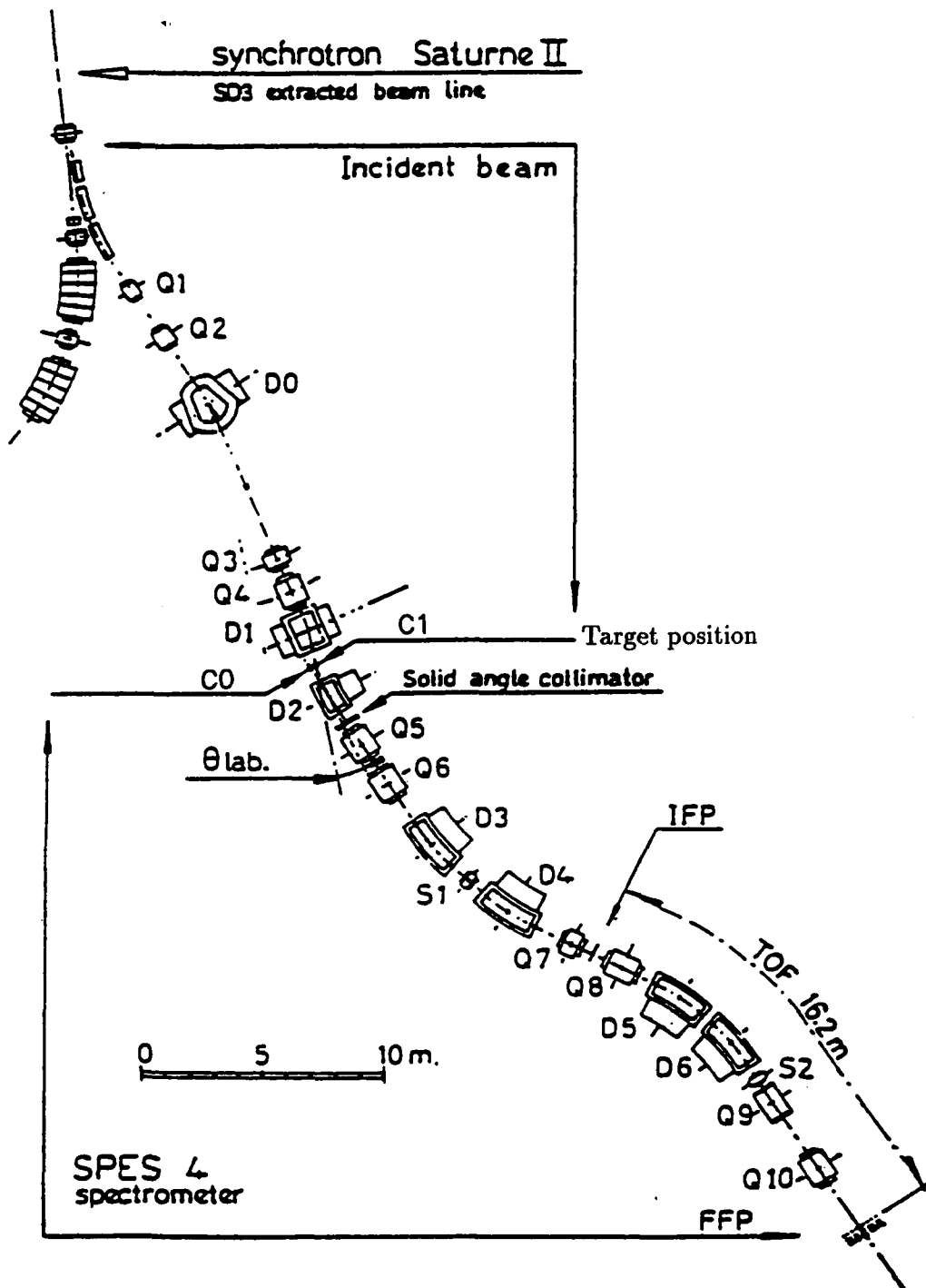


Figure 2-3: The magnetic spectrometer SPES4.

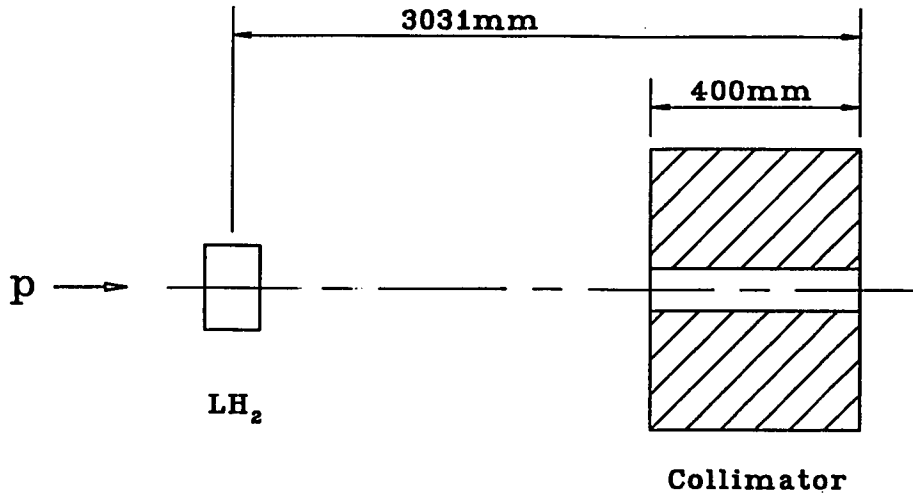


Figure 2-4: The target cell and collimator of SPES4.

3 meters upstream of the entrance of SPES4 as shown in Figure 2-4. Forty centimeter thick collimators with circular openings of variable sizes were used to define the solid angles and to control the number of particles entering SPES4.

Eight p/z settings of SPES4 were used in the first part of the experiment. They began at half the deuteron beam momentum and extended almost to the proton-deuteron backward elastic scattering peak at 2.726 GeV/c. There was a four order of magnitude difference in the cross section over the range of measurements. Therefore different combinations of beam intensity and collimator opening sizes were used to maintain a reasonable count rate. The eight p/z settings together with the corresponding collimator opening sizes are shown in Table 2-1

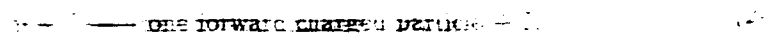
During the polarimeter calibration, the liquid hydrogen target was removed from the beam line and the polarized proton beam was sent directly into SPES4. The p/z setting of SPES4 was tuned to match the beam momentum.

p/μ (GeV/c)	beam intensity (deuterons per spill)	collimator opening diameter (mm)
1.75	$2 > 10^8$	10
1.85	$2 > 10^8$	10
1.97	$2 > 10^8$	30
2.09	$2 > 10^{10}$	10
2.21	$2 > 10^{10}$	10
2.33	$2 > 10^{10}$	30
2.46	$2 > 10^{10}$	30
2.61	$2 > 10^{10}$	30

Table 2-3: The p/μ SPES-0 settings and the experimental conditions for the eight data points.

2.3 Polarimeter

The polarization of the protons was measured at the final focal plane of SPES-0 by a large polarimeter POMME (Polarimeter Mobile à Moyenne Énergie). The operational principle of POMME (HT90, TG92) is based on the classic method of proton scattering on carbon. A 31.2 mm thick carbon block (1) which is made up of three 2.4 cm thick graphite slabs with density of 1.8 g/cm^3 , was used as the analyzer. Three small X^0 multi-wire proportional chambers (MWPC) (C1, C2, C3) with sensitive area of $48 \times 48 \text{ cm}^2$ were placed in front of the carbon block while three large X^0 MWPC (C4, C5, C6) with sensitive area of $90 \times 90 \text{ cm}^2$ were placed after it. They provided the particle tracking both in front of and after the carbon block. A $5.0 \times 7.5 \times 0.5 \text{ cm}^3$ plastic scintillator (S) was placed in front of the carbon. The geometry of the polarimeter is shown in Figure 2-4. POMME is able to measure proton polarizations in a large energy domain and of a size large enough to cover the entire focal plane of SPES-0. It uses the proton-carbon inclusive reaction:



For every event, a proton in the front chambers and a charged particle in the rear chambers was expected. Almost all these fast forward going charge particles are protons.

and the reaction is dominated by $C(p,p)X$.

All six wire chambers of POMME had two signal planes, X and Y, with wires running perpendicular to each other. The anode wires were 20μ gold-plated tungsten and the wire spacing was 2 mm for all chambers. The small chambers had a total of 241 wires per plane and the large chambers had 481 wires per plane. The combination of the "magic gas" used for the chambers was 70% of argon, 24% of isobutane, 0.4% of freon and 5.6% of methylal. The gap between the anode wires and the cathode was 4mm for the small chambers, and 6mm for the large chambers. A high voltage of 2900 V was applied to the small chambers during their normal operations, and 3850 V to the large chambers.

The wire chambers recorded the particle trajectories before and after the scattering at the carbon analyzer. From that, the polar and azimuthal scattering angles of each event could then be calculated. We chose to use the laboratory frame and the coordinate system with the z -axis along the optical axis of POMME, the y -axis pointing upward and the x -axis pointing to the left when looking downstream. The angular distribution of the scattered protons is then given by

$$n(\theta, \phi) = n_o(\theta)\{1 + A_c(\theta)[P_y \cos \phi - P_x \sin \phi]\}, \quad (2-2)$$

where $A_c(\theta)$ is the analyzing power and $n_o(\theta)$ is the distribution for unpolarized protons. P_y and P_x are the projections of the proton polarization onto the y - and x -axis, respectively. It should be pointed out that the coordinate system used in the above equation is the ordinary spherical coordinates system, instead of the one according to the Madison convention. The differences between them are discussed in Appendix A.

Both the left-right asymmetry, $P_y A_c(\theta)$, and the up-down asymmetry, $-P_x A_c(\theta)$, can be found by performing a Fourier analysis on the ϕ -distribution of the scattered protons at each angle of θ . If the analyzing power of POMME, $A_c(\theta)$, is known from the calibration, the transverse polarization of the proton can then be found.

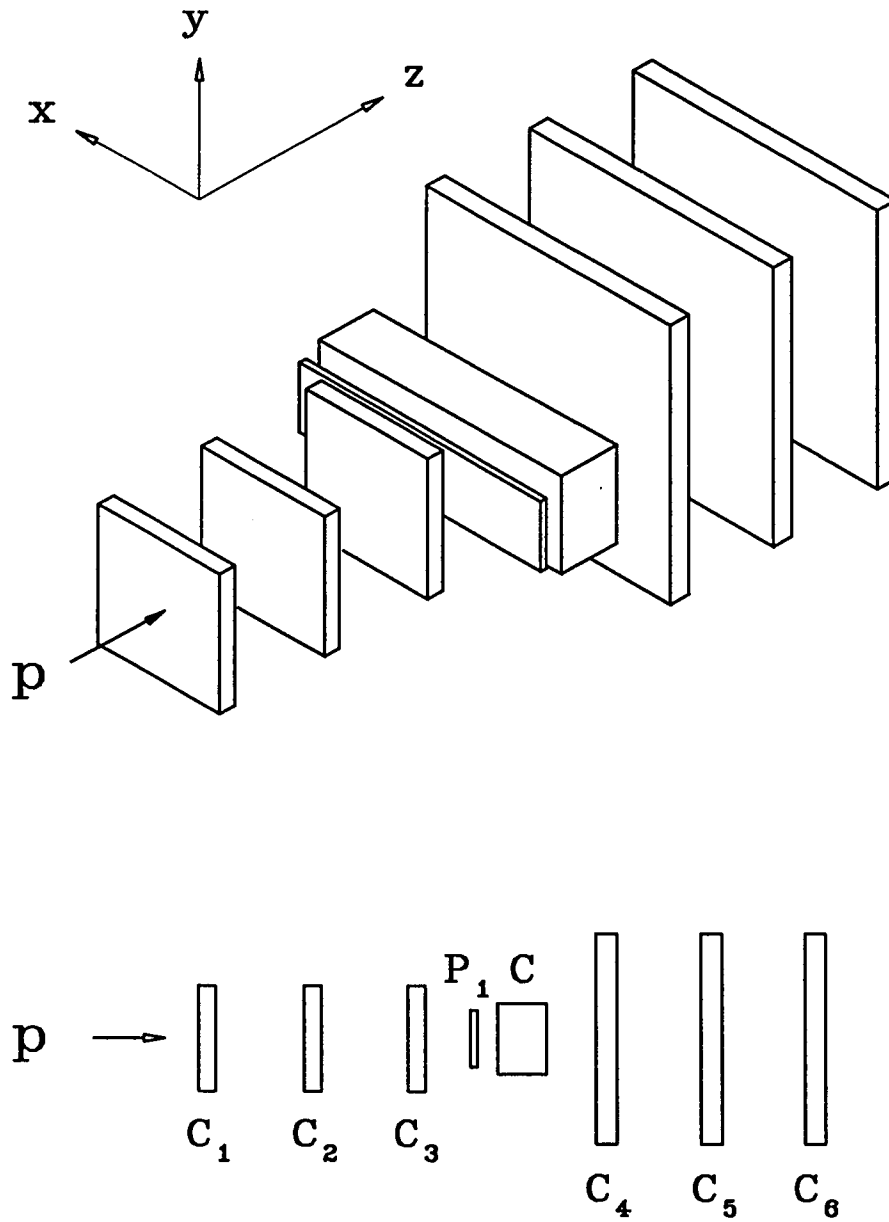


Figure 2-5: The polarimeter POMME

2.4 POMME calibration

During the polarization transfer experiment, the energies of the protons detected for different data points range from 1.0 to 1.8 GeV. The polarimeter POMME had been previously calibrated only for proton energies between 0.5 and 1.2 GeV [B⁺90]. Part of the present experiment was to extend this calibrated region of POMME up to 1.8 GeV. We had planned to do the calibration at 1.2, 1.4, 1.6 and 1.8 GeV. Unfortunately, due to time constraint, we could only finish the two higher energy points.

During the calibration of POMME, the polarized proton beam was accelerated to the desired energy and then extracted simultaneously at both extraction points of Saturne II, SD2 and SD3. About 95% of the beam was extracted at SD2 and directed onto a CH₂ target of a four-arm left-right coincidence proton beam polarimeter, where the beam polarization was measured. At the same time, the rest of the proton beam was extracted at SD3. This portion of beam was de-focused and then passed through a vertical slit before it was sent directly into the spectrometer SPES4. The width of the slit was adjusted to control the beam intensity entering SPES4 and POMME. The slow extraction system of Saturne cannot work properly if the intensity is lower than 10⁷ particles per spill. This intensity is still much too high for the MWPC used in POMME if the full beam from SD3 is sent on to the wire chambers. The charge collected on each chamber would be so high that the protective circuit would automatically shut down the chambers. The only possible way to reduce the beam intensity after extraction is by mean of de-focussing the beam and the use of a slit to select only a fraction of the particles from the enlarged beam profile.

The calibration of POMME was based on the assumption that the two proton beams extracted simultaneously at two different points had the same polarization. This assumption seems reasonable but yet needed to be verified. A verification procedure was performed at each proton energy. A 10 cm liquid hydrogen target was put in place at

T_p (GeV/c)	p/z setting (GeV/c)	
	during calibration at 0°	during verification at 10.1°
1.6	2.358	2.263
1.8	2.573	2.460

Table 2-2: The p/z SPES4 settings during the POMME calibration.

the target position C1 and the direction of the incident proton beam was moved to 10.1° to match the scattering angle of the forward arms of the proton beam polarimeter at SD2. SPES4 became a single arm proton polarimeter with a liquid hydrogen analyzer as shown in Figure 2-6.

By knowing the proton-proton analyzing power at 10.1° and assuming that the polarization of the beam spill for spin-up and spin-down states had the same magnitude but with opposite sign, we could find the average proton polarization after the extraction point SD3 by using SPES4. The value obtained was then compared with the polarization measurement from the beam polarimeter at SD2. As shown in Section 3.6, the two results were found to agree with each other to within the statistical uncertainty.

During the double extraction verification process, SPES4 was set to the momentum corresponding to the proton-proton elastic scattering at 10.1°. For the calibration, SPES4 was tuned to the beam momentum. The p/z settings of SPES4 during this part of the experiment is shown in Table 2-2.

2.5 Deuteron Beam Polarimeter

There is no high energy deuteron polarimeter at Saturne. Instead, the polarization of the deuteron beam is measured at the exit of the polarized source by a low energy deuteron beam polarimeter (DBP). It has been shown both theoretically and experimentally that the deuteron beam does not depolarize during acceleration at Saturne up to 2.3 GeV [A⁺88]. Therefore, the beam polarization at high energy after acceleration

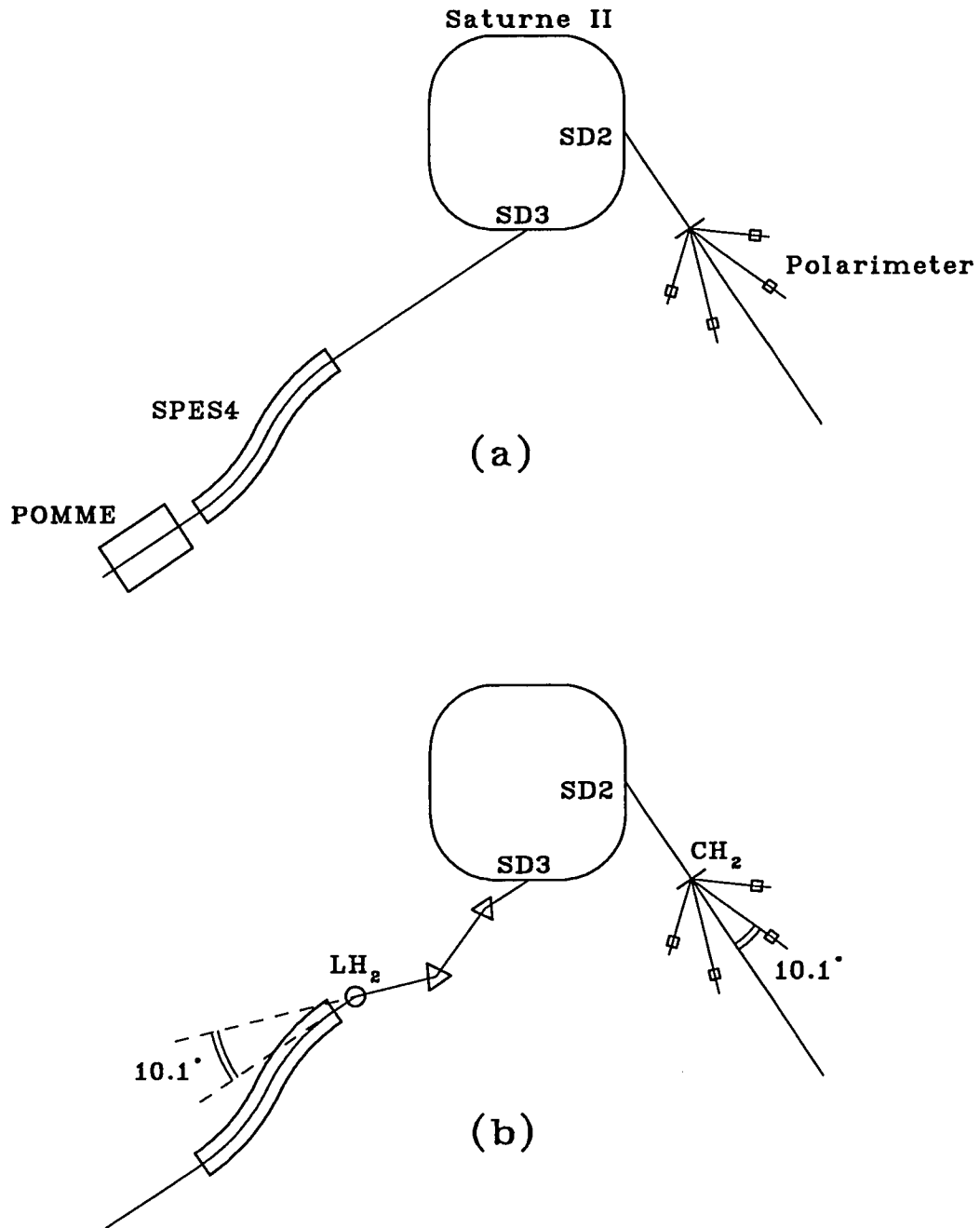


Figure 2-6: The double extraction settings during the POMME calibration (a), and during the verification (b).

should be the same as the polarization measured by the DBP at low energy.

The polarimeter DBP is installed in the beam transport line between the source and the injector. The deuteron energy at this location is 386 keV. Because of the very low deuteron energy, it is impossible to place a permanent target in the beam line. The polarimeter is placed after one of the dipole magnets of the transport line. When the current in the dipole is switched off, deuterons go straight into the polarimeter instead of bending towards the injector.

The reaction used for DBP is ${}^2H(d, p){}^3H$. This reaction was chosen because it is exothermic and it has a large vector analyzing power at 386 keV. The analyzing power of this reaction also changes slowly with respect to the incident energy [A⁺88], which allows a smooth interpolation for a thick target where energy loss of the particles is significant. The outgoing protons are detected at 0° and ±120° where their energies are 4 and 3 MeV respectively, using 150 μm surface barrier silicon detectors 24mm in diameter, as shown in Figure 2-7.

The number of particles scattered to the 120° left and right detectors in the DBP, n_L and n_R respectively, were recorded. The asymmetry, X , was calculated by

$$X = \frac{n_L - n_R}{n_L + n_R}. \quad (2-3)$$

This asymmetry is related to the deuteron polarization by

$$X = \frac{3}{2} P_Z A_{DBP} \quad (2-4)$$

where P_Z is the deuteron vector polarization and A_{DBP} is the analyzing power of the reaction. The polarization can be found if A_{DBP} is known either from a calibration or from a theoretical calculation.

The deuteron beam polarization was measured every 24 hours during the four-day polarization transfer experiment. The five polarization measurements were consistent with each other to within the statistical error and gave an average value of about 90% of

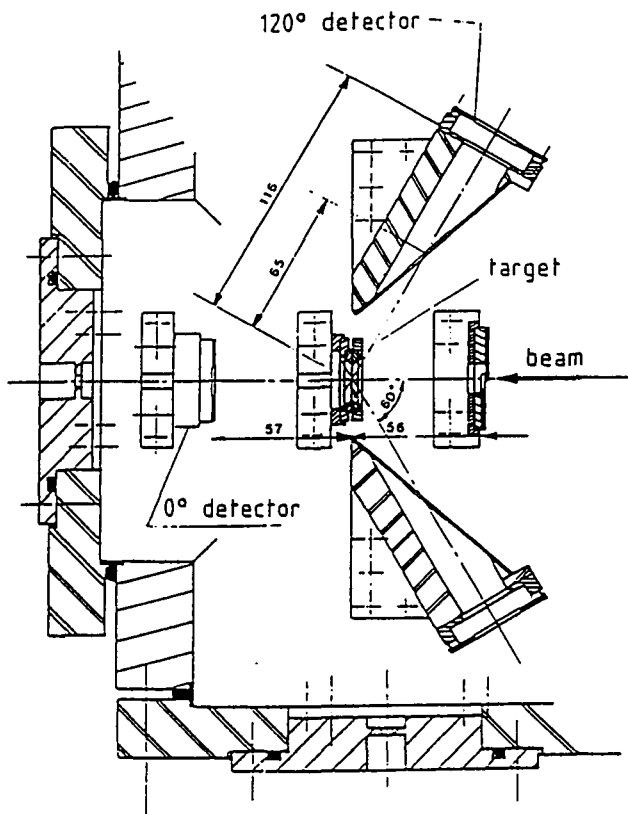


Figure 2-7: The low energy deuteron beam polarimeter.

the maximum theoretical value. The polarization of the deuteron beam was very stable throughout the experiment. The detailed analysis of the deuteron beam polarization is given in Section 3.7.2.

2.6 Electronics

2.6.1 SPES4

At the spectrometer SPES4, the intermediate focal plane is covered by a hodoscope I [B⁺87] consisting of 12 contiguous scintillator counters (I_1, I_2, \dots, I_{12}) of the size of 10 cm high, 1 mm thick and 21.6 cm wide. Each I counter is connected to two XP2020 photomultiplier tubes, one at the top and the other at the bottom. In front of each photomultiplier tube is a light-emitting diode, LED, which is connected to a pulse generator.

A horizontal image of the I counters is formed at the final focal plane. It consists of 12 contiguous geometrical zones each corresponding to one I counter. At a distance from the final focal plane, the images of the I counters are dispersed and the geometrical zones become wider and overlap with each other. A hodoscope (F_1, F_2, \dots, F_{13}) is put at a distance of 14.2 cm after the final focal plane. The dispersed zone of a I_i counter is covered with two half overlapping counters F_i and F_{i+1} . The F counters are made of plastic scintillator 14 cm high, 12 cm wide and 1 mm thick. A XP2020 photomultiplier tube and a LED are mounted on each F counter.

The electronics of SPES4 was built with NIM and CAMAC standard modules giving NIM and ECL standard signals. A SPES4 trigger signal was generated when a particle passing through the I_i counter also hit the corresponding F_i or F_{i+1} counter. The signals from the photomultiplier tubes of the I and F were fed to constant fraction discriminators. For each I count, the signals from the top and the bottom of the scintillator were sent to a mean-timer. It generated a mean time information of I_i which is independent of the particle impact coordinate. The signal from I_i was then

fed to a computer controlled delay box where it was delayed to compensate the time required for the particle to travel from I to F . Finally, all I and F signals were fed to a coincidence unit. The TDC signal of individual I and F counters were also recorded.

Two synchronized pulse generators were used to drive the LEDs in front of each I and F hodoscope counters to simulate particles flying through the spectrometer. It allowed fine time adjustment between the I and F coincidence.

2.6.2 POMME

The polarimeter POMME was equipped with a simple, low cost and compact electronic system to treat the wire chamber signal. POMME was designed to measure single track events only. An expensive one discriminator per wire readout system was not necessary. Instead, the position determination of the chamber was done by charge division on a resistor chain that connected all the anode wires [FL91] as shown in Figure 2-8. The charge collected on the hit wire flowed down along the anode wire into the resistor chain. Charge preamplifiers were spaced regularly along the line to amplify the charge. There was a preamplifier every 16 wires for the small chambers and every 32 wires for the large chambers. The signal from each preamplifier was sent to a receptor which amplified the signal further. The total gain was about 100. A fast ADC multi-channel system (LeCroy FERA) was used to encode the charge. A programmable threshold for the FERA allowed one to suppress the background. Only the FERA signals above the corresponding threshold were transmitted to the computer.

The trigger of POMME consisted of a coincidence between the plastic scintillator P_1 and the hodoscope F of SPES4. Scintillator P_1 was put 5.5 cm in front of the carbon analyzer C , and F was 22 cm upstream of P_1 . The scintillator was viewed from both ends by photomultiplier tubes XP2020. The coincidence of the POMME trigger and the SPES4 trigger is made in a specially designed coincidence module which activates the data acquisition process. The logic of this trigger module is shown in Figure 2-9.

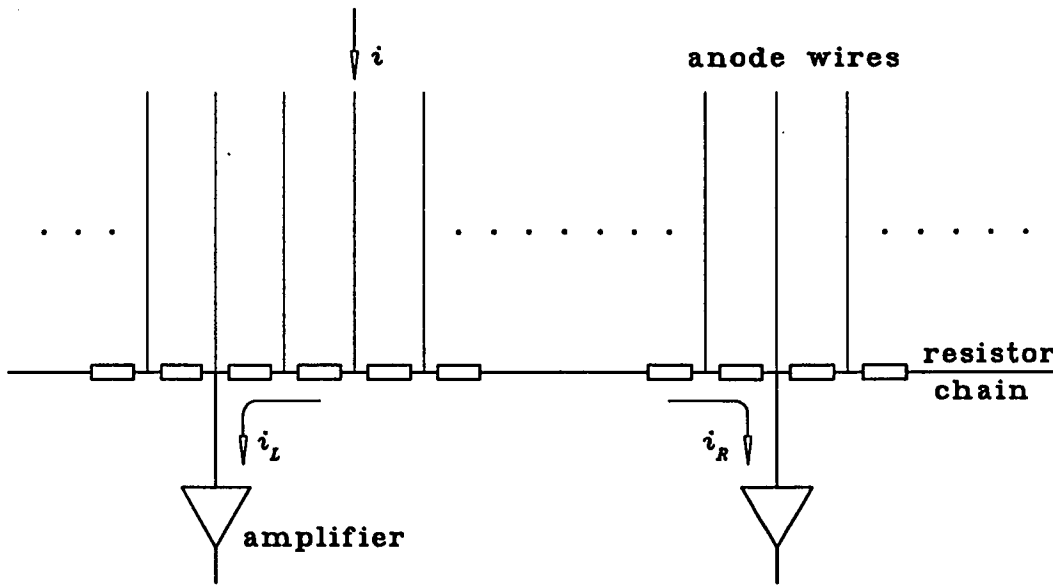


Figure 2-8: The readout system of the wire chambers.

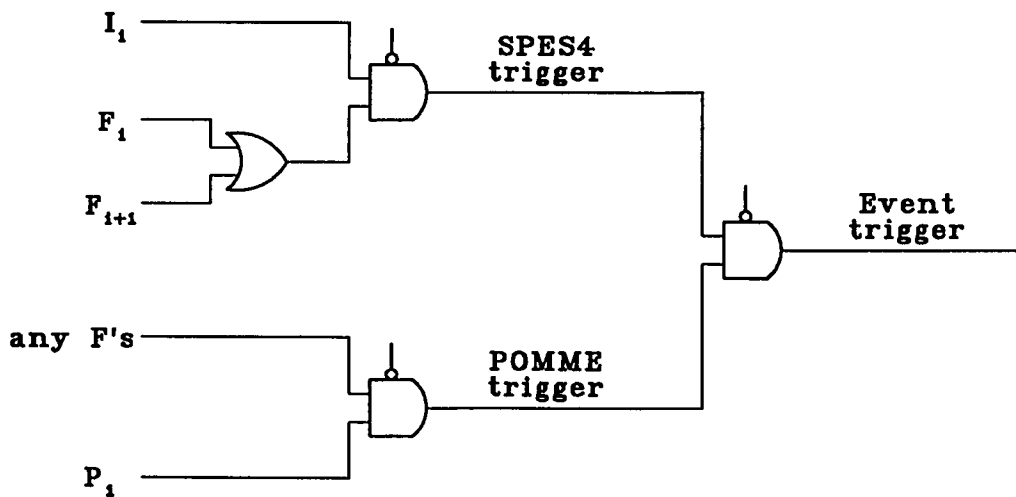


Figure 2-9: The structure of the event trigger.

2.7 Data Acquisition

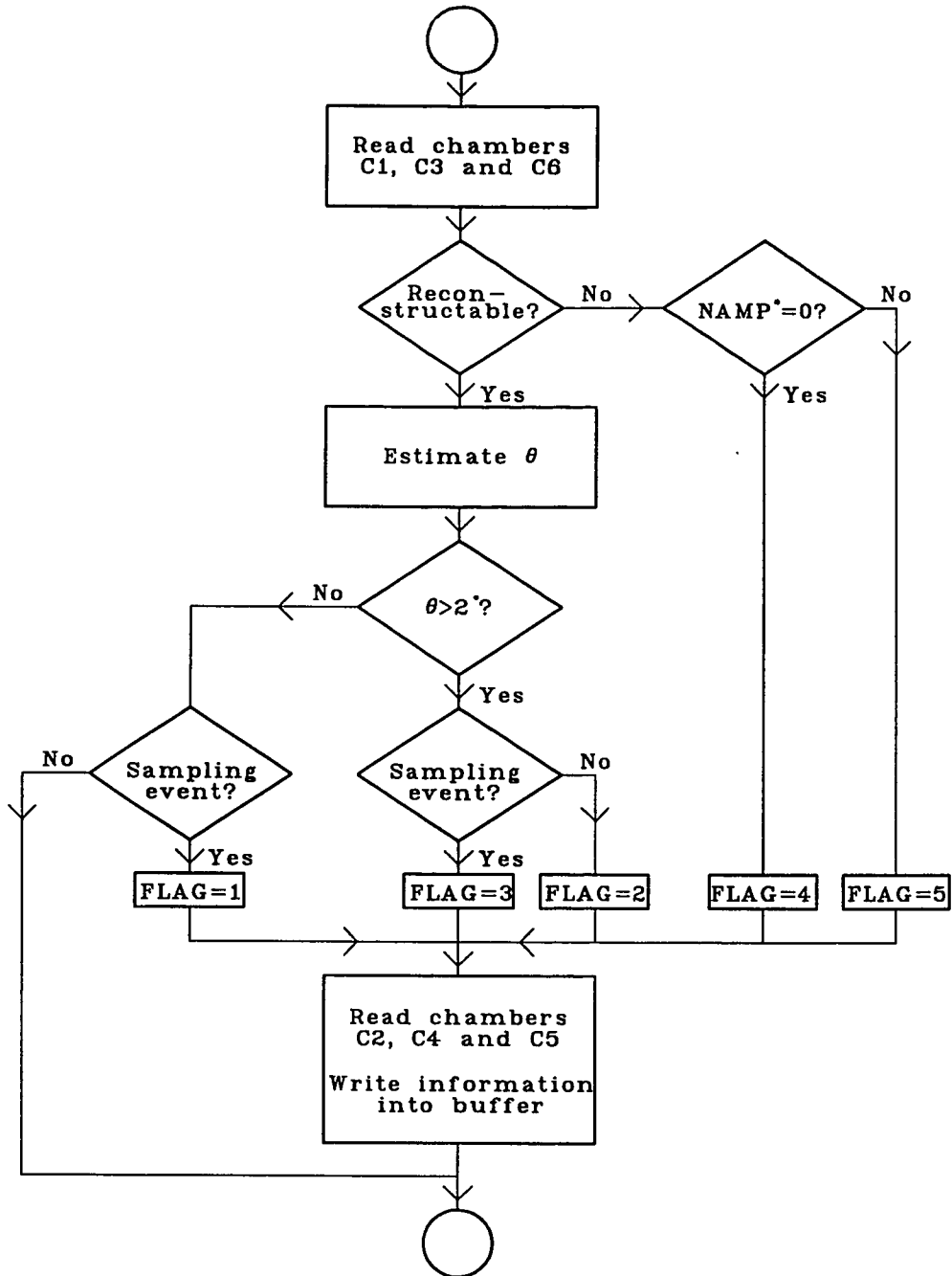
The data acquisition was accomplished with a CAMAC system and the SAR (Satellite d'Acquisition Rapide or Fast Acquisition Satellite) computer developed at the Laboratoire National Saturne in the late 1970's. As soon as an event trigger appeared, the computer was interrupted. A special treatment program was activated in the computer which performed the reading of the event parameters from the CAMAC modules. At the same time, a pulse was generated to prevent any other event trigger by vetoing the coincidence module. The system was restored and ready for new events after the computer finished the acquisition procedure.

More than half the proton-carbon reactions in POMME were multiple Coulomb scatterings with no nuclear interaction involved. Those events are of little use for the proton polarization measurements since Coulomb scattering is spin independent and has no analyzing power. Such purely Coulomb events also had typical scattering angles of 0.6° (r.m.s.) in the proton energy range of this experiment. This made them even more undesirable since the azimuthal angular resolution of POMME was poor when the polar scattering angle was small. The ϕ -distribution of the proton-carbon scattering events with θ less than 1° was unreliable. An on-line data reduction procedure, with the help of a computer program RAF [TG92b], was intended to remove these unwanted events from the acquisition.

The idea of the on-line data reduction was to have a quick way to find the polar scattering angle of the proton-carbon interaction in POMME and to reject the events if their angles were smaller than a preset value. This "fast rejection" process was fast ($\sim 105\mu\text{s}$ per event) [TG92b] and did not tie up the computer. The dead-time of the acquisition system was always kept below 25%. The flow chart of the program RAF is given in Figure 2-10. The program did a rough estimation of the scattering angle by using only the information from three of the six wire chambers. It read the FERA values

from the first and the third small chamber in front of the carbon block and the last large chamber. Both x and y coordinates of these three chambers were reconstructed and the scattering angle was calculated. In this experiment, if the angle was larger than 2° , the FERA of the remaining wire chambers and all the other experimental parameters from the CAMAC modules would be stored in the computer memory buffer. On the other hand, if the angle was found to be smaller than 2° , the event would be rejected and none of the remaining CAMAC modules would be read. The system was then reset by a "fast clear" signal and ready for the next event trigger. In some cases, the polar scattering angle could not be found on-line due to problems of the wire chambers. Those events were still kept and saved on tape for off-line analysis. Every hundredth event was stored in the buffer regardless of the result of the on-line scattering angle estimation. Those events were specially marked and served as a sample of the original population before the on-line data reduction.

Between successive beam bursts, the computer SAR transferred the data from its memory buffer onto a magnetic tape for permanent storage. After finishing the tape writing task and before the arrival of the next beam burst, the SAR did a simple on-line analysis of the events from the previous burst. The computer looked at as many events as time allowed and updated about a hundred histograms. Displaying those histograms on-line was very helpful for monitoring the experiment during its progress.



* NAMP:- number of amplifiers fired on a single wire plane

Figure 2-10: Flow chart of the on-line data reduction program.

Chapter 3

Data Analysis

During the experiment at Saclay, data acquisition and on-line analysis were handled by the computer SAR. The full off-line analysis was done at the College of William and Mary on a microVAX II computer. FORTRAN77 programs utilizing the CERN HBOOK and HPLOT packages were used to analyse the data. The histogram plotting was done with the graphic software PLOTDATA.

In this chapter, the data structure of the experiment is discussed. The details of the data analysis including the special features for POMME and SPES4 are then given. The on-line data reduction and the off-line event selection are described. Finally, the proton polarization and the deuteron beam polarization are calculated together with their corresponding statistical error analyses.

3.1 Data Structure

Data from each run were put on magnetic tape as separate file which contained a number of blocks with variable block size. There were three different kinds of blocks in each file, namely the *labeling block*, the *parameter block* and the *event block*. The labeling block indicated the beginning of a run. The second block of each file was the parameter block which stored all the parameters and constants used during the run. The rest of the file consisted of the event blocks containing the raw data. The number of blocks in each file could be different depending on the amount of data acquired [Sat90].

During each beam burst, data were collected, tested and put in the computer memory buffer for temporary storage. After the end of the beam burst and before the beginning of the following burst, those data were transferred from the buffer to magnetic tape for

permanent storage.

The data from each burst were kept in a separate record. Each record was made up of one or more event blocks depending on the number of events acquired during that beam burst. The maximum size of an event block was 65536 bytes. At the beginning of an event record were the 98 scalers which the computer SAR read from the CAMAC modules. It was followed by the data themselves, which were recorded in an event-by-event format. The data from each event consisted of the TDC and the firing pattern from the hodoscopes I and F of SPES4, together with the ADC and TDC information from the scintillator P_1 , and the FERA signals from the wire chambers of POMME. There was also a SAR clock signal for every event, which recorded the "time" when the event happened relative to a synchronized signal provided by the accelerator at the beginning of each beam burst. SAR transferred the data from its buffer on to a magnetic tape during that brief moment between beam bursts. When it used up all the 65536 bytes in the first event block, it moved on to the next block and so on until it finished copying everything from the memory buffer. All 98 scalers were reset before the beginning of the next beam burst and the record of the events from the new burst was started with a new event block.

Besides the magnetic tapes, additional backup copies of the data were put on 8mm exabyte tapes. The data file from each run was first copied onto a hard disk of the microVAX before any analysis to speed up the process by cutting down the input/output processing time. SAR and microVAX have slightly different data structure. Using microVAX to read a file written by SAR required a byte-flipping procedure for every data word. It was done by a computer program before the analysis was begun.

3.2 POMME

The function of POMME is to measure the angular distribution of the protons from the pC scattering, and from that to determine the proton polarization. The heart

and soul of this polarimeter is the six multi-wire proportional chambers. One of the main tasks of the analysis was to decode the FERA signals from the chambers and to reconstruct the particle trajectory.

As mentioned in Section 2.6.2, POMME uses a special charge division method on a resistor chain to locate which anode wire the particle hit. This resistor chain connects all the anode wires, and 16 amplifiers are placed evenly along the chain. The segment between two consecutive amplifiers is defined as a *section* and labeled by a section address, SA. There are 15 sections on each wire plane. The relative position p of the “hit” wire within a section is given by a simple empirical formula

$$p = at + bt^3 + 0.5 \quad \text{with} \quad t = \frac{1 [rR - L]}{2 [rR - L]} \quad (3-1)$$

where $R(L)$ is the FERA from the right(left) amplifier of the section, r is the relative gain between the two amplifiers, a and b are parameters (one set for the small chambers and another set for the large chambers) which take into account the portion of sensitive area within a section and the non-linearity defaults along the resistor chain, respectively. The best values of a and b for the small chambers are found to be 0.91 and 0.00, respectively. For the large chambers, the values are 0.81 and 0.2657.

This formula works under the assumption that only two consecutive amplifiers fired. The definition of an amplifier fired was that its FERA ADC signal was above the preset threshold, the signal was then transmitted to the SAR and eventually ended up on tape. Those thresholds were calibrated before the experiment by reading the FERA from the chambers when there was no particle hitting them. This corresponds to the “dark current” measurements of individual chambers.

In reality, any number between 0 and 16 amplifiers could fire on one plane. The analysis criterion was to select those events with one to four consecutive amplifiers fired. If only one amplifier fired, the location of that amplifier was used as the position of the hit anode wire. When three consecutive amplifiers fired, the middle one and the

one on the side with the larger signal were chosen. When four consecutive amplifiers fired, the middle two were used. No event with more than four amplifiers fired was analyzed.

For the central part of the front chamber where most of the incoming particles hit, a better formula was used to replace the one described above. It introduces a FERA offset parameter for each amplifier and keeps only the linear term in t' ,

$$p = at' + 0.5 \quad \text{with} \quad t' = \frac{1[r'(R + \delta_R) - (L + \delta_L)]}{2[r'(R + \delta_R) + (L + \delta_L)]}, \quad (3-2)$$

where $\delta_R(\delta_L)$ is the offset parameter for the right(left) amplifier and r' is the new relative gain. This formula works better than the Equation 3-1 simply because it has more parameters. The new parameters for every section are obtained by adjusting their values until the distribution of p resembles the known anode wire spacing.

The results of the position spectrum of a single section, in both the small and the large chambers, are given in Figure 3-1. It clearly shows that the small chambers have better spatial resolution. For the large chambers, one anode wires at each edge of a section is "missing". This happens because of the huge difference in resistance on the resistor chain on both sides of that anode wire. The charge division mechanism puts most of the current to the nearer amplifier, while the amplifier on the far side of the section gets almost no current. Since every amplifier has a preset threshold value to eliminate the background noise, any signal below that threshold will be discarded. The event becomes a "single amplifier fired" event. The position of the particle in this section will then be assumed to be the location of the fired amplifier.

A Cartesian coordinate system, as shown in figure 2-5, was used when reconstructing the particle trajectories. The z-coordinate of every chamber with respect to a fixed reference point was measured very carefully at the beginning of the experiment. Their value are shown in table 3-1. They were stored in the parameter block and put on tape every time when a new run was started.

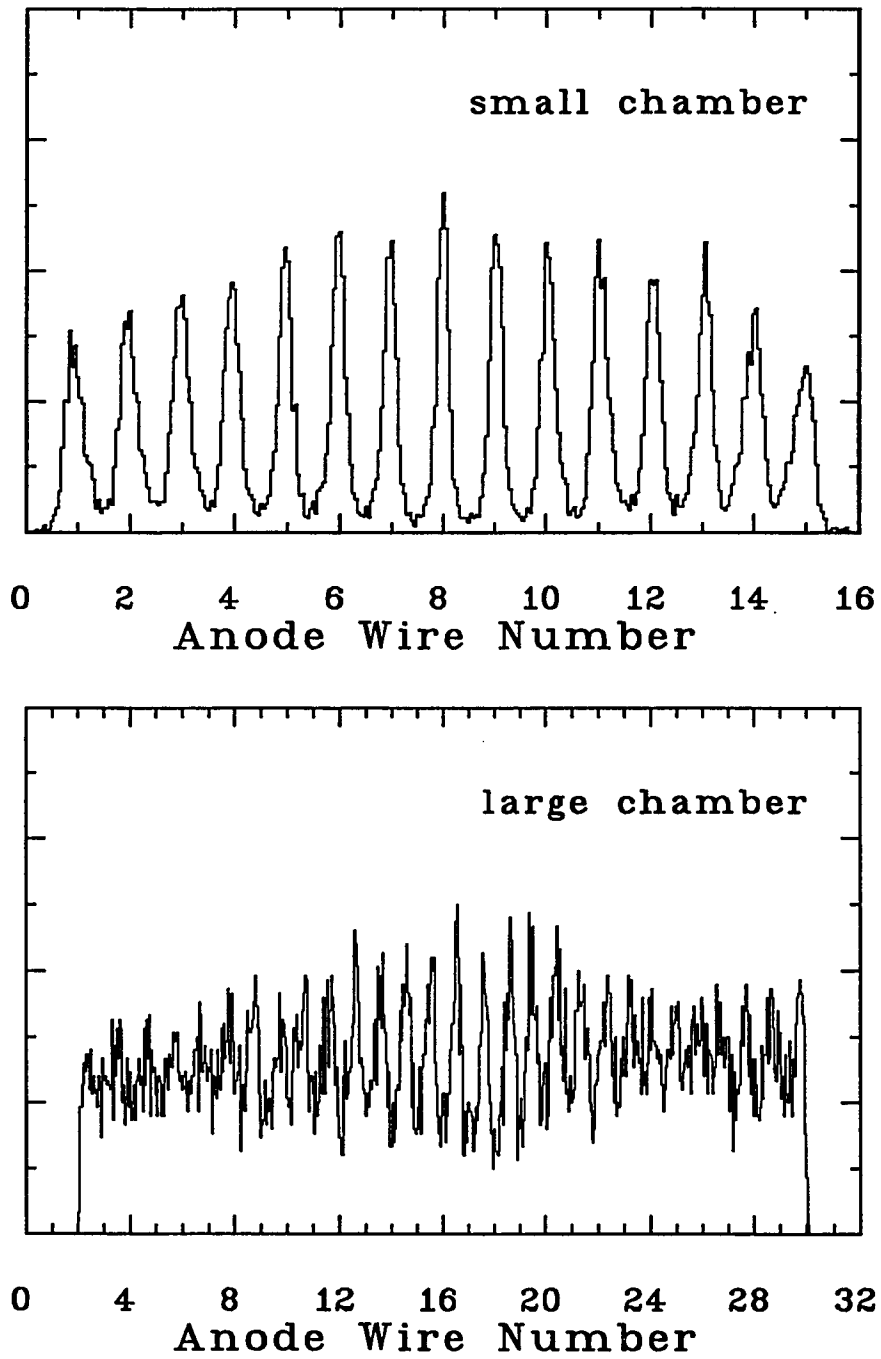


Figure 3-1: The position spectrum of a small chamber (a), a large chamber (b).

Chamber	z-coordinate (mm)	
	X plane	Y plane
C_1	-1196	-1204
C_2	-696	-704
C_3	-196	-204
C_4	739	715
C_5	1182	1158
C_6	1625	1601

Table 3-1: The z -coordinates of the chambers from a fixed reference point.

The x and y coordinates of the particle at each chamber is given by

$$x = (p + SA - 8.5)\ell_{sec} + X_o \quad (3-3)$$

$$y = (p + SA - 8.5)\ell_{sec} + Y_o \quad (3-4)$$

with $\ell_{sec} = 32\text{mm}(64\text{mm})$ for the small(large) chambers being the width of a section, and SA the address of the section where the “hit” anode wire was located. X_o and Y_o are the geometrical offset parameters (one for each plane) which take into account an eventual misalignment of the chambers. The three large chambers were misaligned on purpose by one third of a section width ($\sim 21\text{mm}$) to reduce the possible systematic error in the scattering angles determination due to the missing wire problem at the edges of each section lining up.

As shown in Equation 3-3 and 3-4, the alignment of the chambers is very crucial in calculating the particle trajectory and the geometrical offset parameters must be very finely adjusted. During the experiment, one run was dedicated to determine those parameters. In this run, the carbon block was removed from POMME and the particles were sent directly onto the wire chambers. The particles travelled along a straight path through all six chambers. Their coordinates at each chamber were found following the same procedure mentioned above except for the geometrical offset parameters, X_o and Y_o , in Equation 3-3 and 3-4 were set to zero. An equation of a straight line was then calculated using the particle coordinates at the first and the last chambers. For the

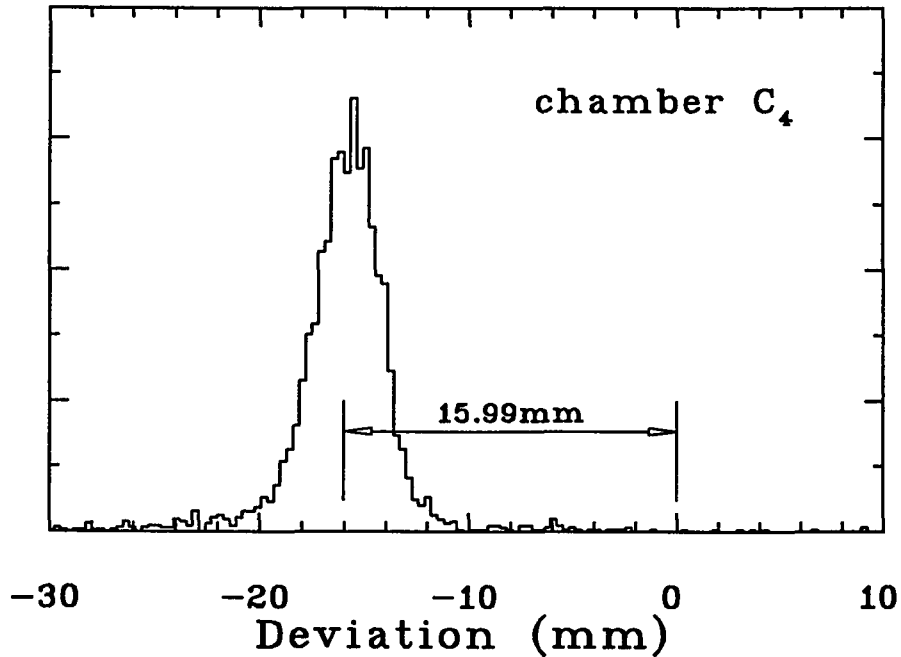


Figure 3-2: The deviation between the straight line and the position readout from the y -coordinate of chamber C_4 .

four remaining chambers, the difference between the particle coordinate at each plane and the corresponding value calculated by the straight line equation was plotted in a histogram. The distance of the centroid from the origin gave the geometrical offset parameter of that chamber. The result of Y_0 for chamber C_4 is shown in Figure 3-2 as an example. The offset parameters for all six chambers are given in Table 3-2.

After including the newly found geometrical offset in the calculation, the particle coordinates from all six chambers were used to determine a best straight line for the particle trajectory by least square fit. The difference between this straight line and the particle coordinates at individual chambers was plotted again. This time, the centroid of the distribution should be centered at zero and the width would indicate the spatial resolution of the chamber. The average resolution of all six planes in the front chambers was found to be 1.6mm (FWHM). The average resolution of the rear chambers was

Chamber	offset parameter (mm)	
	X_o	Y_o
C_1	0.00	0.00
C_2	- 1.55	-1.55
C_3	1.30	-2.39
C_4	-20.62	18.37
C_5	19.33	-15.99
C_6	0.00	0.00

Table 3-2: The geometrical offset parameters for the chambers.

3.2mm (FWHM), compared with the 2mm anode wires spacing. The spatial resolution of the small and the large chambers are shown in Figure 3-3.

This same run was also used to estimate the efficiency of the wire chambers with the special readout system. The average efficiency of an individual wire plane is about 98.5% for the small chambers, and is about 83.5% for the large chambers.

The three front chambers are used to track the particle before the proton-carbon scattering while the three rear chambers reconstruct the trajectory after the scattering. Since each chamber consists of both x and y plane, there are three x planes and three y planes for every trajectory. It is an over-determined system. The overall efficiency of the three front chambers as a group to reconstruct the particle track is estimated to be about 99.8%. The similar overall efficiency for the three rear chambers as a group is about 84.4%.

The thickness of the carbon block in POMME was 53.0 g cm^{-2} (31.2cm thick with density of 1.7 g cm^{-3}), to be compared with the carbon nuclear collision length of 60.2 g cm^{-2} . The probability of having any nuclear collision between the proton and carbon is then given by $[1 - \exp(-53.0/60.2)] = 0.59$. The chances for a single, double, triple scattering are 37%, 16% and 5%, respectively. The proton trajectories before and after the pC scattering should intercept with each other within the thickness of the carbon block if there was no multiple scattering. It is not true in reality, even for

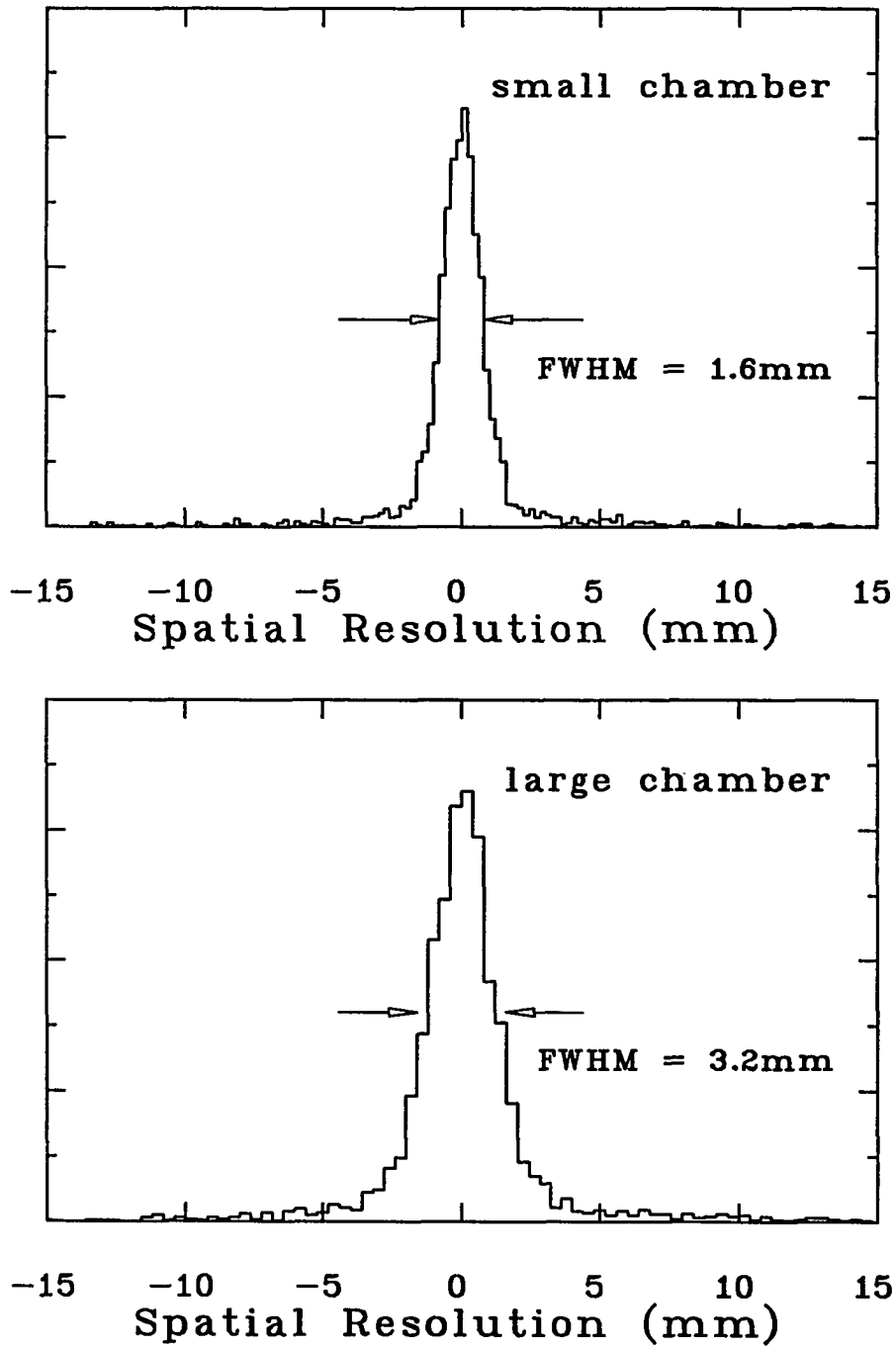


Figure 3-3: The spatial resolution of the small and the large chambers.

the single scattering cases, because of the uncertainty in track reconstruction due to the finite spatial resolution of the wire chambers. Instead, the distance of the closest approach between the two trajectories was calculated. The coordinates at the middle point of this distance was taken to be the interaction vertex.

After the particle trajectories were reconstructed, the polar and azimuthal scattering angles of the pC interaction were calculated using the following equations

$$\cos \theta = \frac{m_{xr}m_{xf} + m_{yr}m_{yf} + 1}{\sqrt{(m_{xr}^2 + m_{yr}^2 + 1)(m_{xf}^2 + m_{yf}^2 + 1)}} \quad (3-5)$$

$$\tan \phi = \frac{m_{yr}(m_{xf}^2 + 1) - m_{yf}(m_{xr}m_{xf} + 1)}{(m_{xr} - m_{xf})\sqrt{m_{xf}^2 + m_{yf}^2 + 1}}. \quad (3-6)$$

m_{xf} and m_{yf} are the slopes of the reconstructed particle trajectories in the front chambers projected on to the x - z and y - z plane, respectively, while m_{xr} and m_{yr} are the same quantities for the rear chambers. The convention was chosen in such a way that ϕ is 0° in the positive x -axis direction (downstream on the left) and is 90° in the positive y -axis direction (upwards). When the incoming particle trajectory is almost parallel to the optical axis such that m_{xf} and m_{yf} are much smaller than 1, the equations become

$$\cos \theta \simeq \frac{1}{\sqrt{m_{xr}^2 + m_{yr}^2 + 1}} \quad (3-7)$$

$$\tan \phi \simeq \frac{m_{yr} - m_{yf}}{m_{xr} - m_{xf}}. \quad (3-8)$$

3.3 SPES4

The main purposes of the magnetic spectrometer SPES4 is to select the protons with the desired momentum, and to transport those protons to the polarimeter POMME. The particle identification in SPES4 is accomplished by combining magnetic rigidity of the particle and its time of flight between the two hodoscopes, I and F . The time of detection in individual I and F scintillator counters was digitized in TDCs and the difference between them defines the time of flight (TOF) of the particle. The TOF

spectra of both combinations of $I_k \cdot F_k$ and $I_k \cdot F_{k+1}$ were calculated for all k from 1 to 12. All the spectra showed a peak corresponding to the protons. At the data points with higher proton momentum, the dipole magnet after the liquid hydrogen target cell together with the collimator of SPES4 were no longer capable of completely separating the protons from the beam particles entering the spectrometer and scattering on various pieces of hardware so as to reach the focal plane. A second peak corresponding to the deuterons began to appear in the TOF spectra. Both peaks have a width of about 30 TDC channels (FWHM) and the separation between them is 180 TDC channels. Accidental coincidence events only appeared at the data points with the highest proton momentum. They showed up as a flat platform under the proton peak as shown in figure 3-4.

The proton peaks in all individual TOF spectra with different I and F counter combinations were shifted to TDC channel 0 before they were added together to form a single I - F TOF spectrum. A window of 100 channel wide (between channel -60 and 40) was used to select protons from this spectrum. For the data point in which accidental coincidences occurred, two additional TOF windows were used to sample the accidental events. Those events were used for the background subtraction. The two windows, one on the left and the other on the right of the proton peak, were from channel -100 to -60, and from channel 40 to 100.

The final focal plane of SPES4 is located between the second and the third front chambers of POMME. The normal of the focal plane makes an angle of 1° with the optical axis. Its location relative to a fixed reference point were recorded in the parameter block and put on tape at the beginning of every run. The direction and the momentum of the particle at the liquid hydrogen target are related to its trajectory at the focal plane by a set of transport coefficients. By knowing the particle information at the focal plane, its momentum and scattering angles at the hydrogen target can be

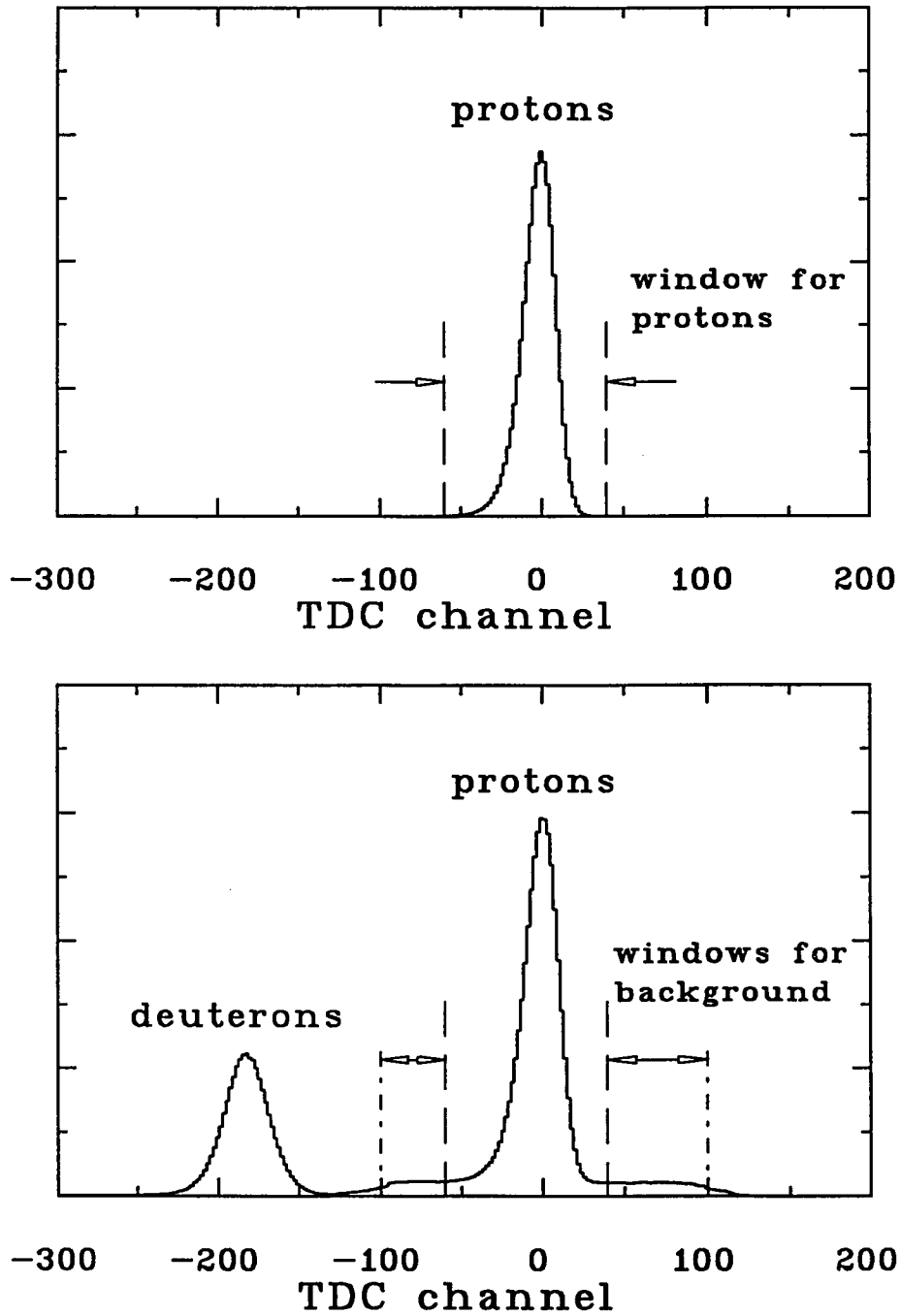


Figure 3-4: The TOF spectrum for the data point with $p/z = 1.75$ GeV/c (a), and the data point with $p/z = 2.61$ GeV/c. The dashed lines are the window for protons and the dash-dotted lines are for the background.

	0	1	2	3	4	5
a	0.5496	1.563×10^{-2}	-6.193×10^{-3}	-1.979×10^{-4}	-2.428×10^{-3}	1.391×10^{-3}
b	0.3031	-0.2829	0.9882	2.337×10^{-4}	4.832×10^{-3}	-2.206×10^{-3}
c		-6.540	3.659	-0.1076	-0.2004	
d		0.1310	-2.678×10^{-2}	-0.2034	0.1994	

Table 3-3: The transport coefficients of SPES4.

calculated from the following equations:

$$\delta = a_o + a_1 X_F + a_2 \Theta_F + a_3 X_F^2 + a_4 \Theta_F^2 + a_5 X_F \Theta_F \quad (3-9)$$

$$\Theta_T = b_o + b_1 X_F + b_2 \Theta_F + b_3 X_F^2 + b_4 \Theta_F^2 + b_5 X_F \Theta_F \quad (3-10)$$

$$\Phi_T = c_1 Y_F + c_2 \Phi_F + c_3 Y_F \delta + c_4 \Phi_F \delta \quad (3-11)$$

$$Y_T = d_1 Y_F + d_2 \Phi_F + d_3 Y_F \delta + d_4 \Phi_F \delta \quad (3-12)$$

where a_i , b_i , c_i and d_i are the transport coefficients given in Table 3-3, $\delta = \Delta p/p$ is the percentage of the particle momentum deviation from the SPES4 p/z setting, Θ is the horizontal angle of the particle trajectory with respect to the optical axis, Φ is the similar vertical angle, and $X(Y)$ is the $x(y)$ -coordinate of the particle. The subscript F indicates the variables are measured at the final focal plane, while the subscript T means the values are calculated at the hydrogen target. In the above equations, δ is in %, X and Y are in mm, Θ and Φ are in mrad.

A single run was done using the deuteron-proton backward elastic scattering reaction, $^1\text{H}(d,p)d$, to verify the values of the transport coefficients. With a 2.1 GeV deuteron beam and the 4cm liquid hydrogen in place, the rigidity of the spectrometer at 0° was set to 2.70 GeV/c with momentum acceptance of about $\pm 3\%$. The protons emerged from this elastic reaction would have a momentum of 2.725 GeV/c. It was found that the original value for one of the transport coefficients, a_o , had to be increased from 0.0496 to 0.5496 for this experiment. The momentum spectrum of this backward elastic scattering is given in Figure 3-5.

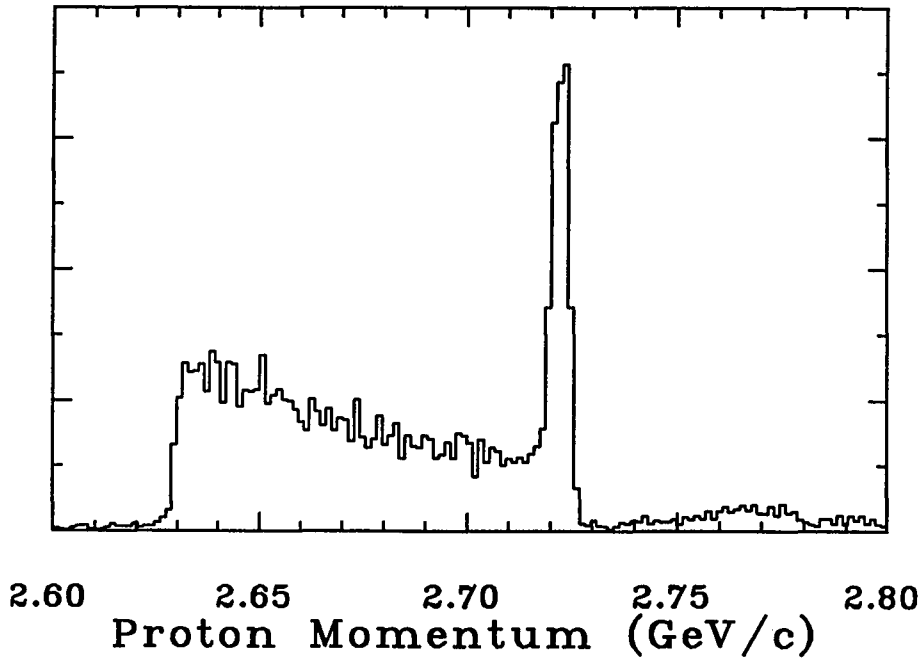


Figure 3-5: The proton momentum spectrum of dp backward elastic scattering.

3.4 Event Selection

3.4.1 On-line

The on-line data reduction program RAF, discussed in section 2.7, was used during the data acquisition to remove events with proton-carbon scattering angles less than 2° . Due to the time constraint during the data collection, a simplified method was employed by RAF to calculate the polar scattering angle. It read the information from the first and the third front chambers as well as the last rear chamber of POMME. The particle coordinates on each chamber were calculated in the same way as described in section 3.2, except with the relative gain r set to 1, and the non-linearity parameters $a=1$ and $b=0$. The polar scattering angle θ was then approximated by

$$\tan^2 \theta = \frac{f^2 + g^2}{z^2} \quad (3-13)$$

where

$$f = \left[\frac{z_6 - z_3}{z_3 - z_1} (x_3 - x_1) + x_3 \right] - x_6 \quad (3-14)$$

$$g = \left[\frac{z_6 - z_3}{z_3 - z_1} (y_3 - y_1) + y_3 \right] - y_6 \quad (3-15)$$

$$z = z_6 - z_{carbon} \quad (3-16)$$

$x_i(y_i)$ are the particle coordinates at the i^{th} chamber, z_i is the position of the corresponding wire chamber given in Table 3-1 and z_{carbon} is where the center of the carbon block was located along the z -axis. An event was rejected if the scattering angle found on-line was less than 2° . Every hundredth event was collected regardless of the result of the on-line θ calculation. From analyzing this 1% "uncensored" events, it was found that 95% of the events rejected by RAF on-line indeed had θ less than 2° as shown in Figure 3-6.

3.4.2 Off-line

For the off-line analysis, events from a whole beam burst were read by a FORTRAN program and the data was analyzed event-by-event. After treating all events from the burst, the program moved on to the next burst and repeated the same task over until it reached the end of the data file. The TOF between the I and the F hodoscope of SPES4 was first calculated and a 100 TDC channel software window was used to select the protons as mentioned in section 3.3. After this, the particle trajectories in both the front and the rear chambers were reconstructed. The proton-carbon scattering angles could then be found as described in section 3.2.

Up to this point, not every event reconstructed was useful. For instant, some of the protons may have come from the wall of the 40cm thick collimator in front of SPES4 instead of the liquid hydrogen target. Those events should be excluded from the final analysis. A number of variables were calculated for every event and a set of software windows (or cuts) were applied on those variables to remove the unwanted events. The

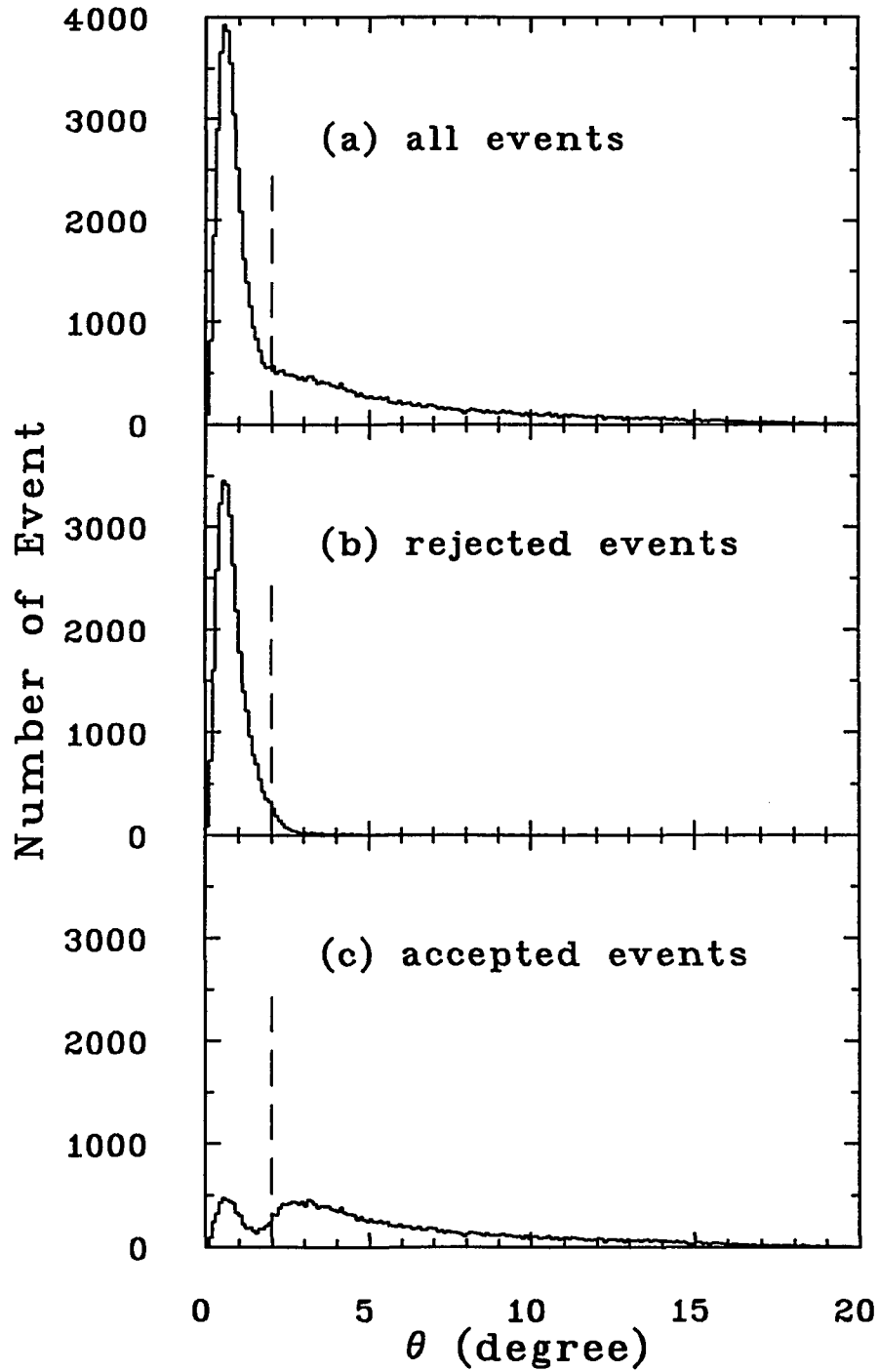


Figure 3-6: The θ -distribution of the 1% sampling events (a). In (b) are events rejected by the on-line data reduction program and the events being kept are show in (c).

main philosophy was to use a number of “loose” cuts rather than a few “tight” cuts. By doing so, the exact widths and locations of the windows were not critical.

The finite resolution of the wire chambers gave some uncertainties in the particle track reconstruction. Those uncertainties propagate to the proton-carbon scattering angle calculation and they directly affected the proton polarization measured in the experiment. Some steps were taken to minimize the amount of those uncertainties in the analysis.

The three front chambers functioned as a group to reconstruct the particle track before the carbon. The rear chambers worked in a similar way. A least square fit procedure was used to find the best straight line to represent the particle trajectory in each group of chambers. When all three wire planes in a group fired, the difference between the particle coordinate and the best straight line was calculated for each chambers. The square of these differences were summed together for the x -front chambers, the y -front chambers, the x -rear chambers and the y -rear chambers. These four variables were used to measure how well the straight line agreed with the readout from the chambers. Cuts were applied to these sums to remove events that were badly reconstructed. Obviously, the same summation would be 0 if only two out of three wire planes fired. Any cut on this variable would favor the “two-plane fired” events. That was the reason why the windows on this variable were very wide. The spatial resolution is 1.6mm (FWHM) for the front chambers and 3.2mm (FWHM) for the rear chambers. The windows chosen for these variables had a width of 768mm^2 ($=3 \times [10 \times 1.6\text{mm}]^2$) for the front chambers, and of 3072mm^2 ($=3 \times [10 \times 3.2\text{mm}]^2$) for the rear chambers.

The coordinates of the proton-carbon interaction vertex were reconstructed for every event as described in section 3.2. Cuts were put onto these coordinates to reject events with the calculated pC vertex far away from the carbon analyzer. The physical size of the carbon block in the x , y and z direction were $\pm 27.4\text{cm}$, $\pm 13\text{cm}$ and $\pm 16.25\text{cm}$,

respectively. The corresponding cuts were $\pm 40\text{cm}$ on the x -coordinate, $\pm 20\text{cm}$ on the y -coordinate and $\pm 50\text{cm}$ on the z -coordinate. The distance of the closest approach, d_{clos} , between the particle tracks in the front and the rear chambers was also calculated. Events with this distance larger than 2cm were considered to be bad events and rejected. The histograms of each coordinate and its corresponding window are shown in Figure 3-7 and 3-8.

With the transport coefficients of SPES4 discussed in Section 3.3, we can calculate the momentum spread of the protons, δ , together with the horizontal and vertical scattering angles at the liquid hydrogen target, Θ_T and Φ_T , respectively. Two 2-dimensional histograms, (Θ_T vs δ) and (Φ_T vs δ), were created. As shown in Figure 3-9, the contour of the SPES4 collimator could be seen clearly in these two histograms. A set of 2-dimension cuts were applied to remove the protons that were obviously not coming from the opening of the collimator.

After all the software cuts mentioned above, the events that survived were considered “good” events. They were protons emerging from the liquid hydrogen target, passing through the opening of the collimator with momentum within the acceptance of SPES4, and then scattered by the carbon analyzer of POMME.

The proton polarization is determined by measuring the ϕ -asymmetry of the proton scattering at the polarimeter. POMME is a specially designed device which can measure the full 2π range of ϕ and for θ up to about 30° . Fourier analysis is used to determine the asymmetry from the angular distribution of the scattered events. But before applying the Fourier analysis, the instrumental asymmetry that originated from the geometrical shape of the wire chambers has to be removed. A test was used to check for every event with polar scattering angle θ , whether the whole 2π range of azimuthal angle ϕ was contained within the geometrical acceptance of the chambers. This cone test removed any event that did not have the whole 2π circle of ϕ within the chamber. The test tends

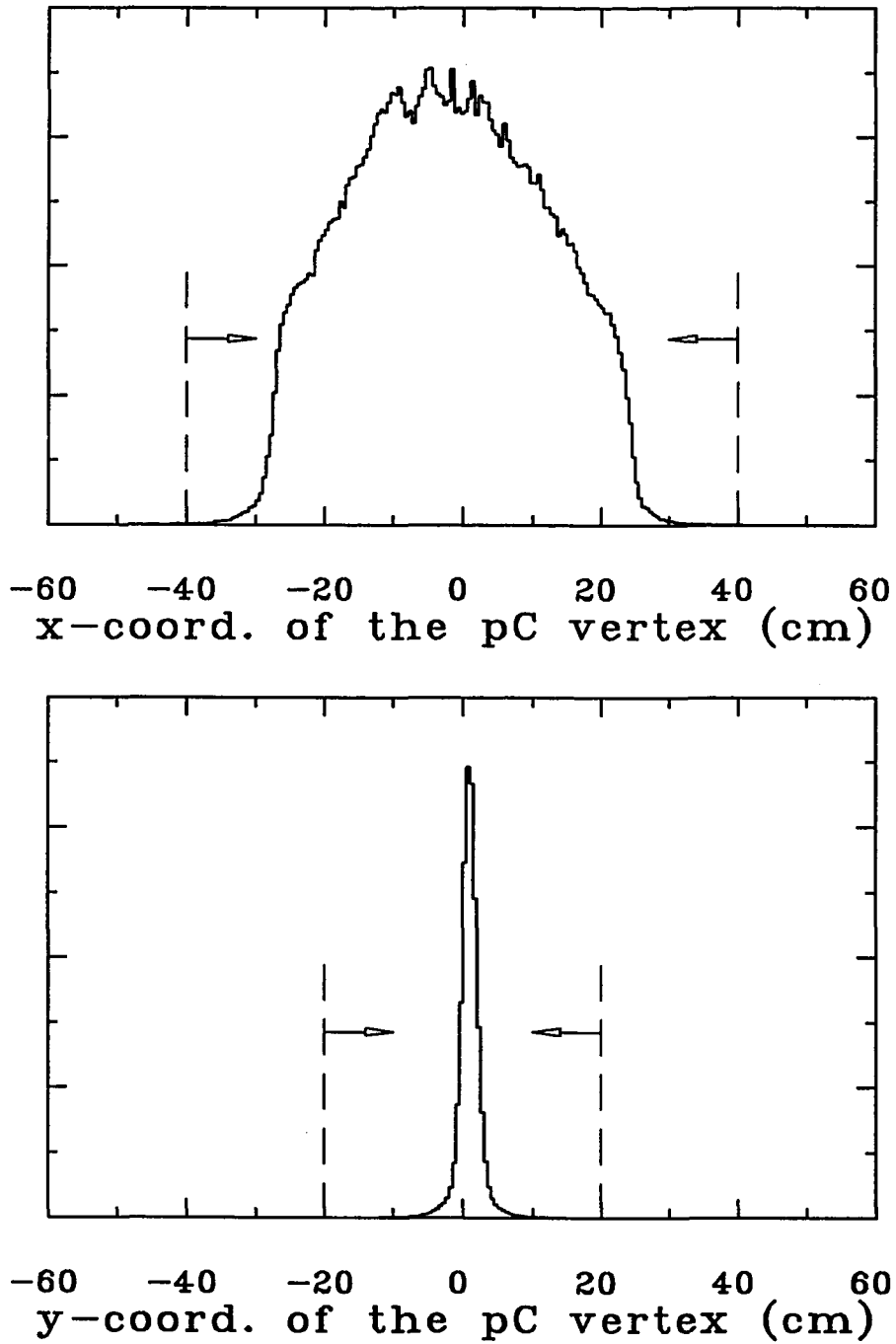


Figure 3-7: The x - and y -coordinates of the proton-carbon scattering vertex. The dashed lines are the locations of the cuts.

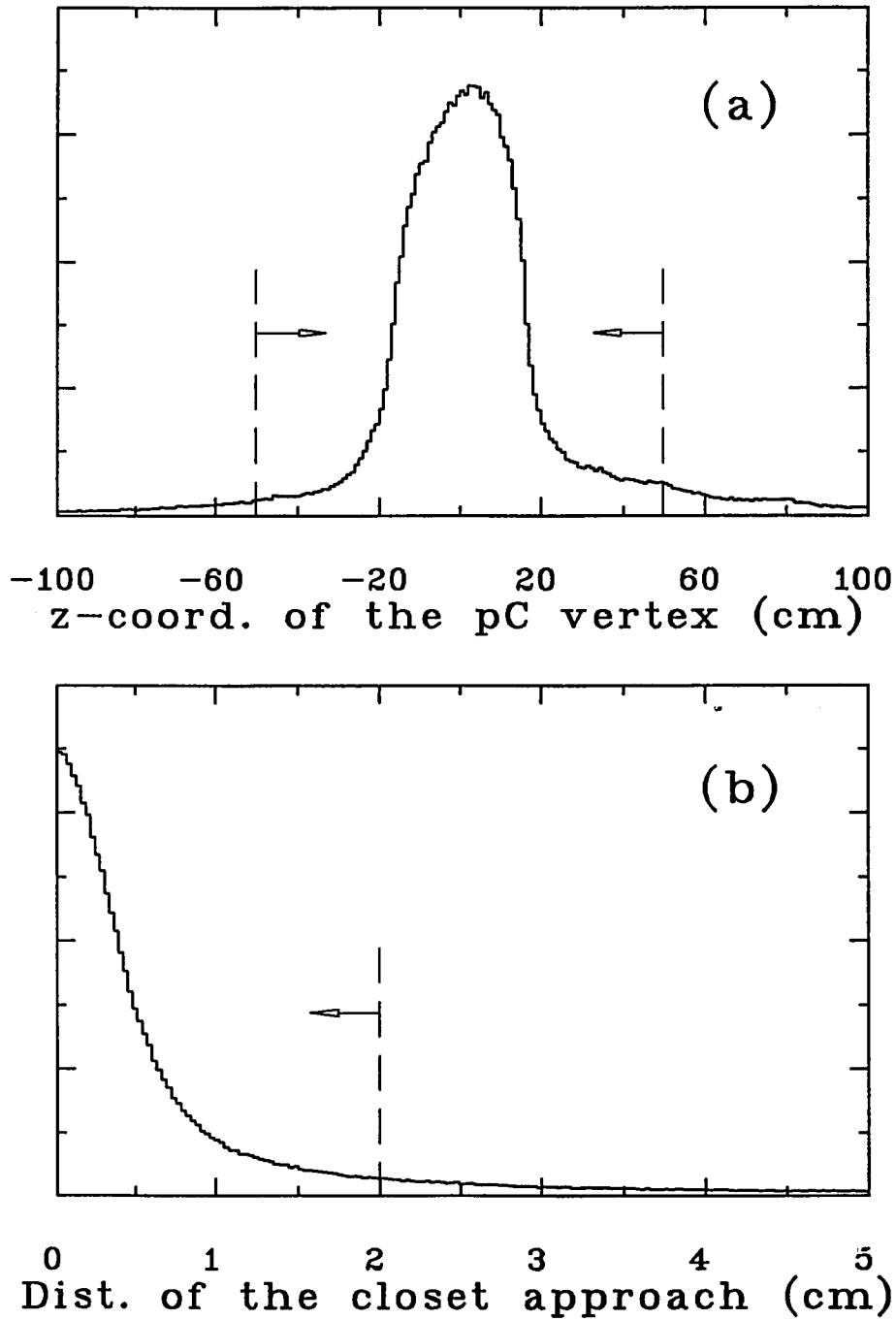


Figure 3-8: The z -coordinates of the proton-carbon scattering vertex (a) and the distance of the closest approach between the trajectories in the front and the rear chambers (b). The dashed lines are the locations of the cuts.

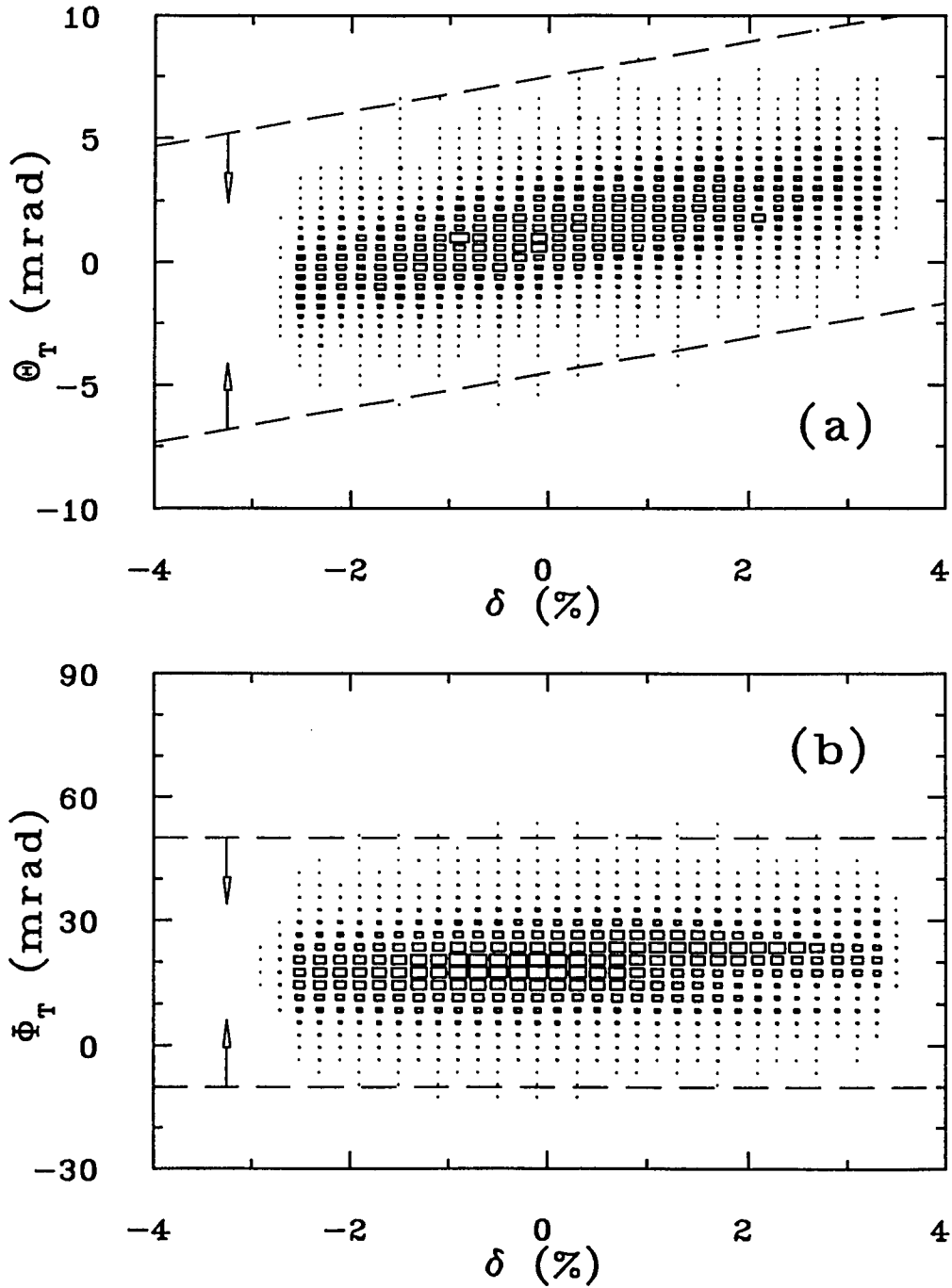


Figure 3-9: The 2-dimensional histogram of Θ_T vs δ (a), and Φ_T vs δ (b). The dashed line are the cuts applied for event selection.

Total number of events		100
On-line data reduction	30	
Number of events on tape		70
Event losses during off-line analysis		
- track reconstruction	30	
- software windows/cuts	12	
- cone test	10	
	52	
Number of surviving events		18
Events with $\theta < 2.5^\circ$	5	
Number of useful events		13

Table 3-4: The number of rejections by individual tests and cuts for every hundred proton-events.

to have a greater effect on events with large θ . The x - and y -coordinates of the particle trajectories at the last chamber C_6 , both before and after the cone test, are shown in Figure 3-10. It clearly shows that most of the events being removed by the cone test come from the edges of the chamber. In Figure 3-11 are the same histograms, but with all the incoming particle trajectories overlapping each other. It shows a circular feature for the events that passed the cone test.

For every 100 protons scattered at the carbon block during the experiment, the tracks of about 70 of them could be reconstructed on-line by the simplified method used by RAF. Out of these 70 events, 30 were rejected by the on-line data reduction program because of their small scattering angles at the carbon block. The remaining 40 events, together with the 30 events that could not be reconstructed on-line, were put on tape.

All events on tape were subjected to off-line analysis. Eighteen out of every 70 events on tape survived all the tests and cuts imposed on them by the analysis program. Thirteen out of the 18 surviving events had scattering angle, θ , between 2.5° and 20.5° . Only those events were used to find the polarization of the proton. The estimated number of events being rejected due to different tests and cuts for every 100 incoming protons are given in Table 3-4.

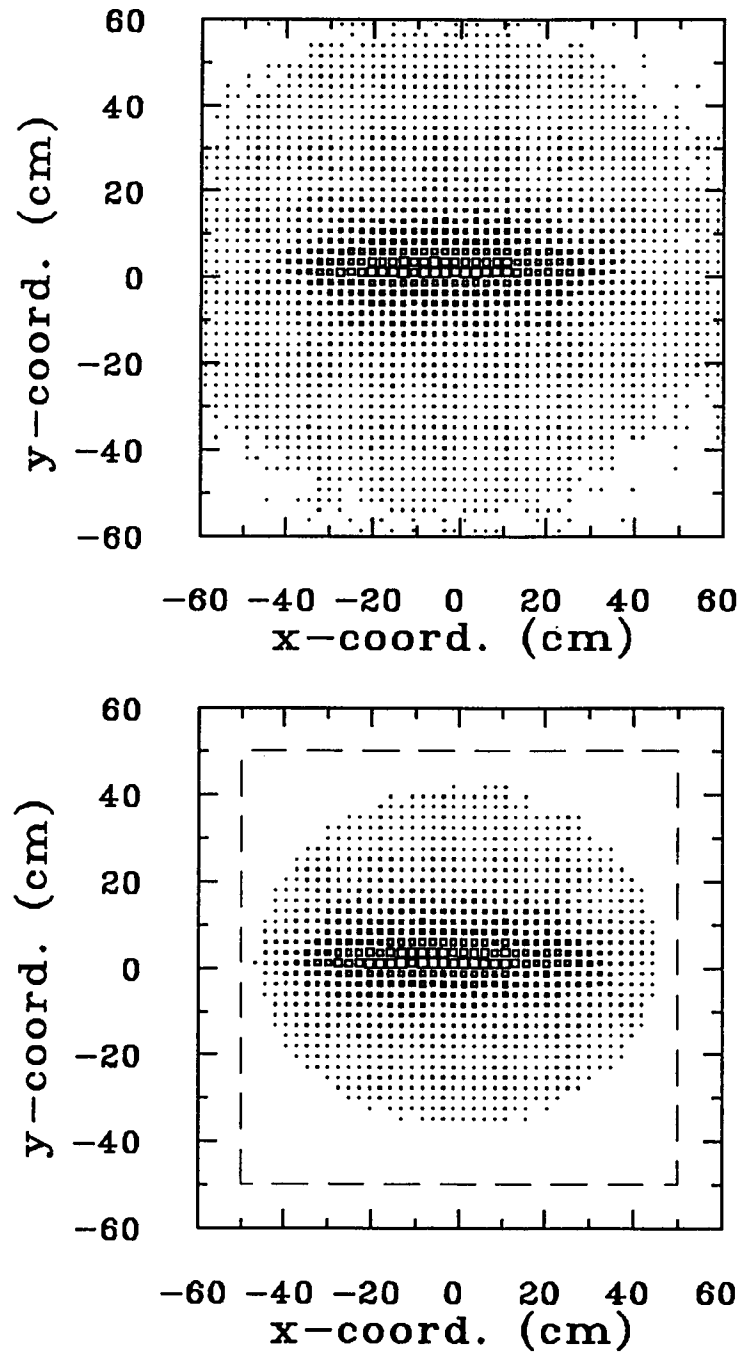


Figure 3-10: The x - and y -coordinates where the particle intercepted the plane of the last wire chamber before (a), and after (b) the cone test. The dashed line indicates the physical boundaries of the chamber.

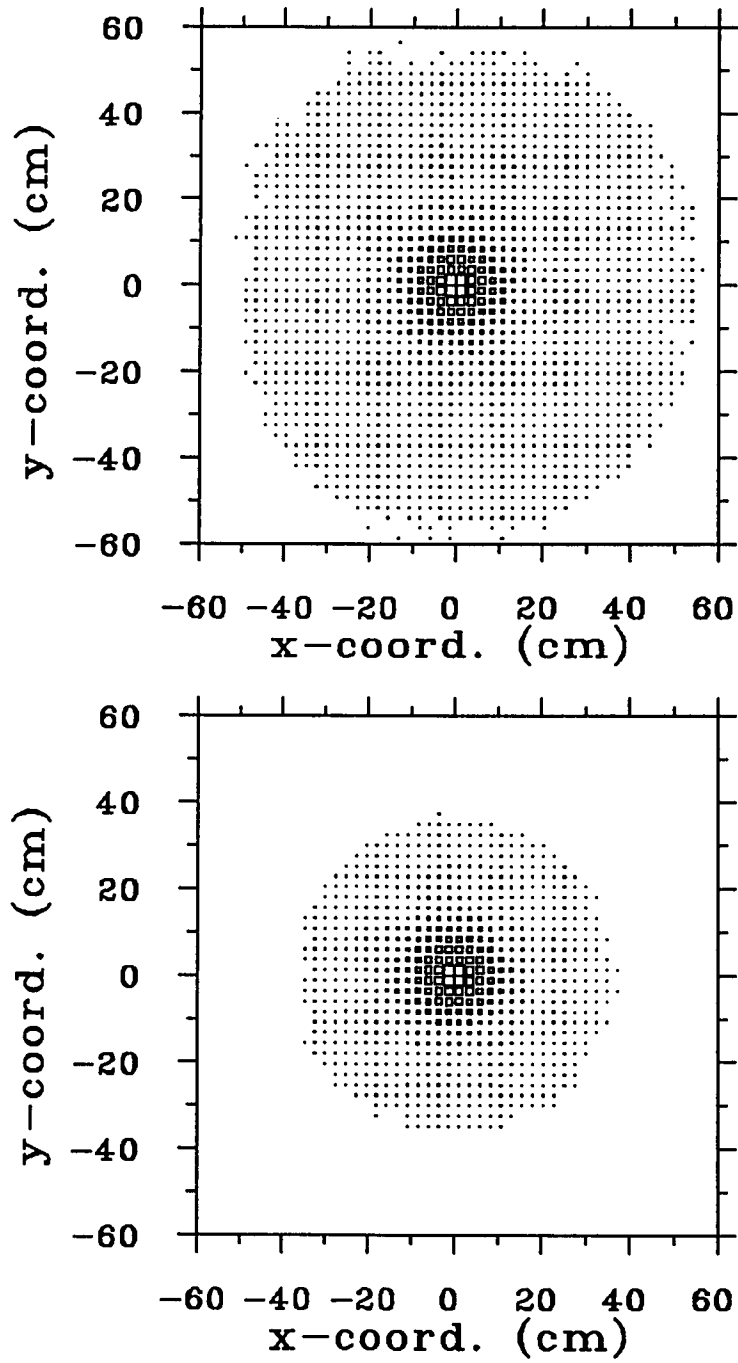


Figure 3-11: Same histograms as figure 3-10, but with the incoming particle trajectories overlapping each other.

After passing all the cuts and the cone test, the angular distribution of the proton-carbon scattering events were subjected to a Fourier analysis to determine the scattering asymmetry.

3.5 Fourier Analysis

For polarized protons, the angular distribution, $n(\theta, \phi)$, from the pC scattering is given by Equation 2-2. The measured distribution $m(\theta, \phi)$ is given by

$$m(\theta, \phi) = D(\theta, \phi)n(\theta, \phi) \quad (3-17)$$

where $D(\theta, \phi)$ is the detection efficiency of POMME in the direction (θ, ϕ) . In general, this detection efficiency depends on the locations where the particle hits each chambers. It is a function of the slopes of the particle trajectories both in the front and the rear chambers, as well as the coordinates of the pC interaction vertex.

$$D = D(m_{xf}, m_{yf}, m_{xr}, m_{yr}, x_o, y_o, z_o) \quad (3-18)$$

To make matters simpler, we assumed that D is independent of the vertex coordinates. Since the incoming particle trajectories were almost parallel to each other, D can be further simplified to

$$D = D(\theta, \phi)$$

as it appears in Equation 3-17.

During the experiment, the direction of the deuteron beam polarization was flipped between every burst and the emerging protons were measured at 0° . According to this geometrical symmetry, the polarization direction of the detected protons should also alternate in a similar fashion. We labeled the state with deuteron beam polarized in the upward direction as “state 2”, and the state with beam polarization pointing downward as “state 3”. Following this notation, we have

$$\begin{aligned} m_2(\theta, \phi) &= D(\theta, \phi)n_2(\theta, \phi) \\ &= D(\theta, \phi)n_{o,2}(\theta)[1 + P_{y,2}A_c(\theta) \cos \phi - P_{x,2}A_c(\theta) \sin \phi], \end{aligned} \quad (3-19)$$

and

$$m_3(\theta, \phi) = D(\theta, \phi)n_{o,3}(\theta)[1 + P_{y,3}A_c(\theta) \cos \phi - P_{x,3}A_c(\theta) \sin \phi]. \quad (3-20)$$

The beam intensities of the two states were very close to each other. As the result, $n_{o,2}$ and $n_{o,3}$ agreed with each other to within a few percents. The ratio η between them was calculated as

$$\eta(\theta) = \frac{n_{o,2}(\theta)}{n_{o,3}(\theta)}, \quad (3-21)$$

which was close to 1. For a given θ , if the detection efficiency, $D(\theta, \phi)$, was largely independent of ϕ , such that

$$\begin{aligned} \int_0^{2\pi} D(\theta, \phi) \cos \phi d\phi &\simeq 0 \\ \int_0^{2\pi} D(\theta, \phi) \sin \phi d\phi &\simeq 0, \end{aligned} \quad (3-22)$$

we had

$$\eta(\theta) \simeq \frac{\int_0^{2\pi} m_2(\theta, \phi) d\phi}{\int_0^{2\pi} m_3(\theta, \phi) d\phi}. \quad (3-23)$$

$\eta(\theta)$ was then used to re-normalize the distribution measured in state 3. The normalized distributions from the two states became

$$m_2(\theta, \phi) = D(\theta, \phi)n_{o,2}(\theta)[1 + P_{y,2}A_c(\theta) \cos \phi - P_{x,2}A_c(\theta) \sin \phi] \quad (3-24)$$

$$m_3'(\theta, \phi) = \eta(\theta)m_3(\theta, \phi) \quad (3-25)$$

$$= D(\theta, \phi)n_{o,2}(\theta)[1 + P_{y,3}A_c(\theta) \cos \phi - P_{x,3}A_c(\theta) \sin \phi].$$

Notice that the factors outside the square bracket are the same for both states.

Finally, we calculated the ratio

$$\begin{aligned} R(\theta, \phi) &= \frac{m_2(\theta, \phi) - \eta(\theta)m_3(\theta, \phi)}{m_2(\theta, \phi) + \eta(\theta)m_3(\theta, \phi)} \\ &= \frac{\frac{1}{2}(P_{y,2} - P_{y,3})A_c(\theta) \cos \phi - \frac{1}{2}(P_{x,2} - P_{x,3})A_c(\theta) \sin \phi}{1 + \frac{1}{2}(P_{y,2} + P_{y,3})A_c(\theta) \cos \phi - \frac{1}{2}(P_{x,2} + P_{x,3})A_c(\theta) \sin \phi}. \end{aligned} \quad (3-26)$$

The proton polarizations of the two states were pointing into the opposite direction. This gave $P_{y,2}$ and $P_{y,3}$ an opposite sign. The same thing was true for $P_{x,2}$ and $P_{x,3}$. If the magnitude of the polarization in the two states were similar, we had

$$(P_{y,2} + P_{y,3}) \ll 1 \quad (3-27)$$

$$(P_{x,2} + P_{x,3}) \ll 1 \quad (3-28)$$

With the value of $A_c(\theta)$ always less than 0.25 for this experiment, the expression became

$$\begin{aligned} R(\theta, \phi) &\simeq \left[\frac{1}{2}(P_{y,2} - P_{y,3})A_c(\theta) \cos \phi - \frac{1}{2}(P_{x,2} - P_{x,3})A_c(\theta) \sin \phi \right] \\ &\quad \times \left[1 - \frac{1}{2}(P_{y,2} + P_{y,3})A_c(\theta) \cos \phi + \frac{1}{2}(P_{x,2} + P_{x,3})A_c(\theta) \sin \phi \right] \\ &= -\frac{1}{8}[(P_{y,2} - P_{y,3})(P_{y,2} + P_{y,3}) + (P_{x,2} - P_{x,3})(P_{x,2} + P_{x,3})]A_c^2(\theta) \\ &\quad + \frac{1}{2}(P_{y,2} - P_{y,3})A_c(\theta) \cos \phi \\ &\quad - \frac{1}{2}(P_{x,2} - P_{x,3})A_c(\theta) \sin \phi \\ &\quad - \frac{1}{8}[(P_{y,2} - P_{y,3})(P_{y,2} + P_{y,3}) - (P_{x,2} - P_{x,3})(P_{x,2} + P_{x,3})]A_c^2(\theta) \cos 2\phi \\ &\quad + \frac{1}{8}[(P_{y,2} - P_{y,3})(P_{x,2} + P_{x,3}) + (P_{x,2} - P_{x,3})(P_{y,2} + P_{y,3})]A_c^2(\theta) \sin 2\phi. \end{aligned} \quad (3-29)$$

If Fourier analysis is performed on R , it will give

$$R(\theta, \phi) = a_0(\theta) + a_1(\theta) \cos \phi + b_1(\theta) \sin \phi + \dots \quad (3-30)$$

By comparing the Equation 3-29 and 3-30, we have

$$\begin{aligned} a_1(\theta) &= \frac{1}{2}(P_{y,2} - P_{y,3})A_c(\theta) \\ &= \bar{P}_y A_c(\theta), \end{aligned} \quad (3-31)$$

$$\begin{aligned} b_1(\theta) &= -\frac{1}{2}(P_{x,2} - P_{x,3})A_c(\theta) \\ &= -\bar{P}_x A_c(\theta). \end{aligned} \quad (3-32)$$

The coefficient a_1 is the left-right asymmetry and b_1 is the up-down asymmetry of the pC scattering. \bar{P}_y (\bar{P}_x) is the magnitude of the average proton polarization projected onto the vertical (horizontal) direction.

The main reason we calculated the variable $R(\theta, \phi)$ instead of applying the Fourier analysis directly to the measured distributions $m_2(\theta, \phi)$ and $m_3(\theta, \phi)$ is to minimize the effect of the detection efficiency of POMME. This whole procedure works only if the conditions at Equation 3-22 are satisfied. If this is not the case, an unpolarized beam can be used to measure $D(\theta, \phi)$ experimentally. Unfortunately, we did not have time to do this measurement.

During the off-line analysis, the measured angular distribution of the proton-carbon scattering were divided into 60 bins over the whole 2π range of ϕ for every one-degree of θ from 1° to 25° . The number of counts in each bin was labeled as $M_{ij}(\theta_i, \phi_j)$ with θ_i and ϕ_j being the angles in that bin. The ratio $R(\theta, \phi)$ in Equation 3-27 became

$$R_{ij}(\theta_i, \phi_j) = \frac{M_{2,ij}(\theta_i, \phi_j) - \eta_i(\theta_i)M_{3,ij}(\theta_i, \phi_j)}{M_{2,ij}(\theta_i, \phi_j) + \eta_i(\theta_i)M_{3,ij}(\theta_i, \phi_j)} \quad (3-33)$$

with

$$\eta_i(\theta_i) = \frac{\sum_{j=1}^N M_{2,ij}(\theta_i, \phi_j)}{\sum_{j=1}^N M_{3,ij}(\theta_i, \phi_j)} \quad (3-34)$$

Fourier analysis was then applied to R_{ij} by calculating

$$a_0(\theta_i) = \frac{1}{N} \sum_{j=1}^N R_{ij}(\theta_i, \phi_j) \quad (3-35)$$

$$a_1(\theta_i) = \frac{2}{N} \sum_{j=1}^N R_{ij}(\theta_i, \phi_j) \cos \phi_j \quad (3-36)$$

$$b_1(\theta_i) = \frac{2}{N} \sum_{j=1}^N R_{ij}(\theta_i, \phi_j) \sin \phi_j \quad (3-37)$$

where N is the number of bins in ϕ . The statistical uncertainties are given by

$$\delta a_0(\theta_i) = \frac{1}{N} \left[\sum_{j=1}^N (\delta R_{ij})^2 \right]^{\frac{1}{2}} \quad (3-38)$$

$$\delta a_1(\theta_i) = \frac{2}{N} \left[\sum_{j=1}^N (\delta R_{ij})^2 \cos^2 \phi_j \right]^{\frac{1}{2}} \quad (3-39)$$

$$\delta b_1(\theta_i) = \frac{2}{N} \left[\sum_{j=1}^N (\delta R_{ij})^2 \sin^2 \phi_j \right]^{\frac{1}{2}} \quad (3-40)$$

proton beam energy (GeV)	proton polarization	
	SD2	SD3
1.6	0.828 ± 0.015	0.868 ± 0.015
1.8	-0.859 ± 0.021	-0.854 ± 0.013

Table 3-5: The proton polarization measured at the two extraction ports, SD2 and SD3, during the double extraction verification procedure.

proton beam energy (GeV)	proton polarization	pp analyzing power
1.6	0.834 ± 0.010	0.330
1.8	-0.893 ± 0.013	0.300

Table 3-6: The measured proton beam polarization during the POMME calibration.

where

$$(\delta R_{ij})^2 = \frac{4\eta_i^2}{(M_{2,ij} + \eta_i M_{3,ij})^4} (M_{2,ij}^2 M_{3,ij} + M_{3,ij}^2 M_{2,ij}) \quad (3-41)$$

3.6 Polarimeter Calibration

POMME was calibrated at both proton energies 1.6 and 1.8 GeV as part of the present experiment. The verification procedure described in Section 2.4 was performed at both energies. The results are given in Table 3-5. The values from the two extraction points were not inconsistent with each other.

After the verification procedure, SPES4 was moved back to 0° and the hydrogen target was removed. The system was then ready for the calibration of POMME. Under the double extraction procedure, 95% of the proton beam was extracted at SD2 and then transported onto a two-arm proton polarimeter where the beam polarization was measured. The results together with the pp analyzing power used are shown in Table 3-6. The remaining 5% of the proton beam was extracted at SD3 and sent directly through SPES4 onto POMME where the pC scattering asymmetry was measured. Fourier analysis was carried out to the angular distribution of the proton-carbon scattering at POMME as discussed in section 3.5. Since the polarization of the proton beam

energy (GeV)	carbon analyzer thickness (cm)	number of data points
0.8	21.6	22
0.8	31.2	22
1.2	21.6	22
1.2	30.0	22
1.6	31.2	18
1.8	31.2	18

Table 3-7: The 124 point data base used for the proton-carbon analyzing power parameterization.

was lined up with the vertical magnetic field of the synchrotron Saturne II, the up-down asymmetry term, b_1 , in equation 3-32 was expected to be zero. The proton-carbon analyzing power at POMME was then given by

$$A_c(\theta_i) = \frac{a_1(\theta_i)}{P_{SD2}} \quad (3-42)$$

where P_{SD2} was the proton polarization measured at SD2.

POMME had been calibrated previously for proton energies between 0.5 and 1.2 GeV [B⁺90]. The new results at 1.6 and 1.8 GeV extended the calibrated range. A sixteen parameter least square fit was used to represent the proton-carbon analyzing power of POMME between 0.8 and 1.8 GeV. The data set included in this fit are given in Table 3-7. It consists of four energies, six sets of data, a total of 124 data points. This fit took an analytical form of

$$A(\theta, p) = \frac{ar}{1 + br^2 + cr^4} + dp \sin(5\theta) \quad (3-43)$$

with

$$r = p \sin \theta \quad (3-44)$$

where p , in GeV/c, is the proton momentum at the middle of the carbon analyzer. The quantities a , b , c and d are parameterized functions of the following forms:

	0	1	2	3
a	1.248 ± 0.148	-0.694 ± 0.339	1.931 ± 0.620	-3.39 ± 1.10
b	17.11 ± 3.39	-10.83 ± 8.67	20.3 ± 19.8	-13.6 ± 28.6
c	21.0 ± 30.4	30.2 ± 53.2	-89.8 ± 66.4	17.3 ± 210
d	0.0414 ± 0.0110	-0.0537 ± 0.0254	-0.1061 ± 0.0457	0.2246 ± 0.0792

Table 3-8: The parameters for the analytical fit of the pC analyzing power.

$$\begin{aligned}
 a &= a_0 + a_1 p' + a_2 p'^2 + a_3 p'^3 \\
 b &= b_0 + b_1 p' + b_2 p'^2 + b_3 p'^3 \\
 c &= c_0 + c_1 p' + c_2 p'^2 + c_3 p'^3 \\
 d &= d_0 + d_1 p' + d_2 p'^2 + d_3 p'^3
 \end{aligned}
 \tag{3-45}$$

with

$$p' = p - 1.9 . \tag{3-46}$$

The coefficients a_i , b_i , c_i and d_i with $i = 0, 3$ are the sixteen parameters to be determined from the calibration data. The shifted momentum, p' , was used as the variable in the above equations because it centered at the middle of the valid momentum range of the fit and made the calculation of the 16 parameters converge faster. The best value we found for the parameters are shown in Table 3-8. These parameters gave the POMME analyzing fit a total Chi-square of 161.84, or a reduced Chi-square of 1.50 per degree of freedom [TG92a]. The fit together with the calibration data are shown in Figure 3-12. The fit describes the data very well. The pC analyzing power for proton energies between 1.0 and 1.8 GeV were calculated based on this fit and the results are shown in Figure 3-13. The analyzing power is around 0.21 at 1.0 GeV. It decreases smoothly as the energy increases, and becomes about 0.11 at 1.8 GeV.

Besides the analyzing power, the figure of merit is also a very important quantity of

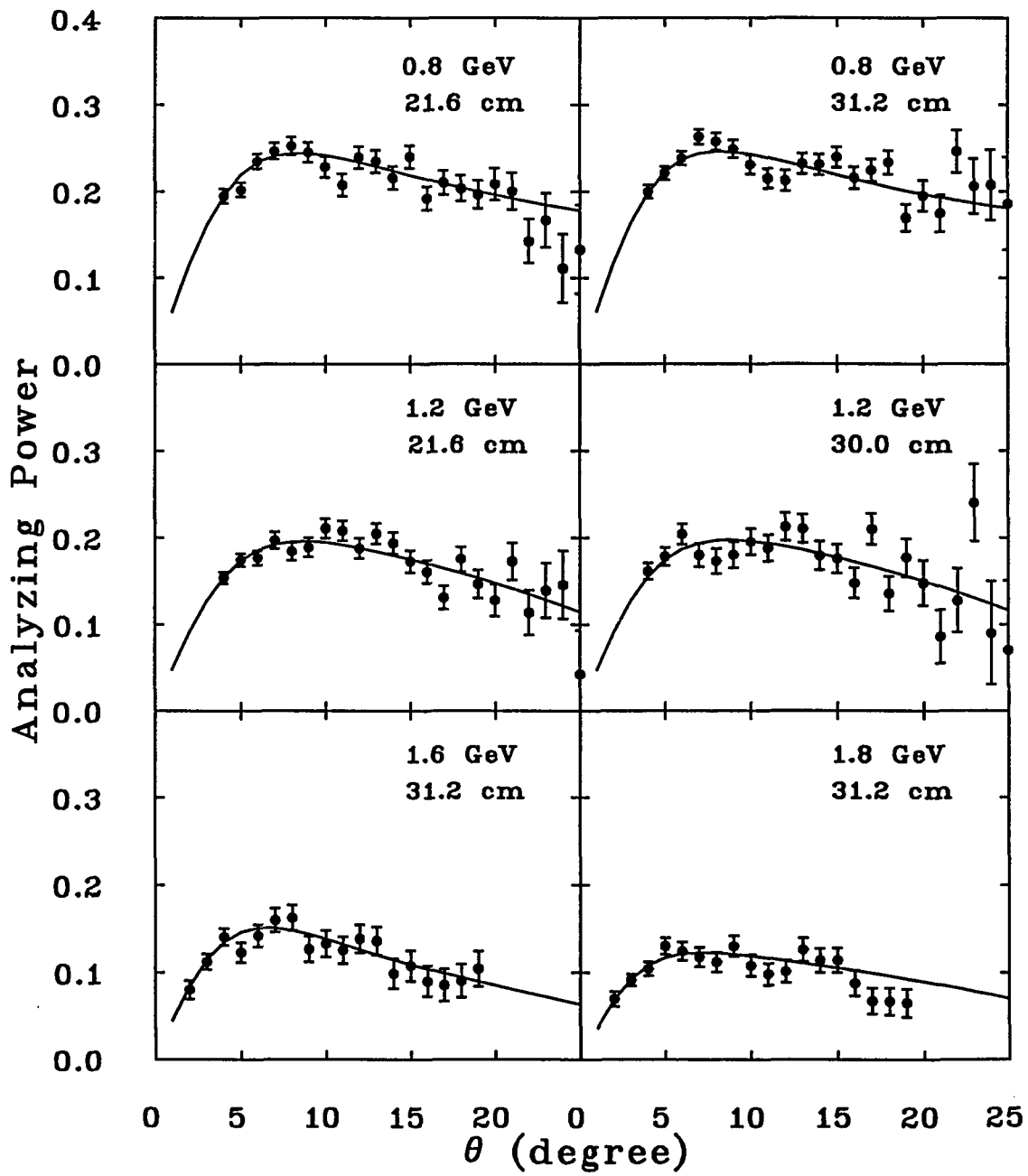


Figure 3-12: The overall fit of the data base for the pC analyzing power.

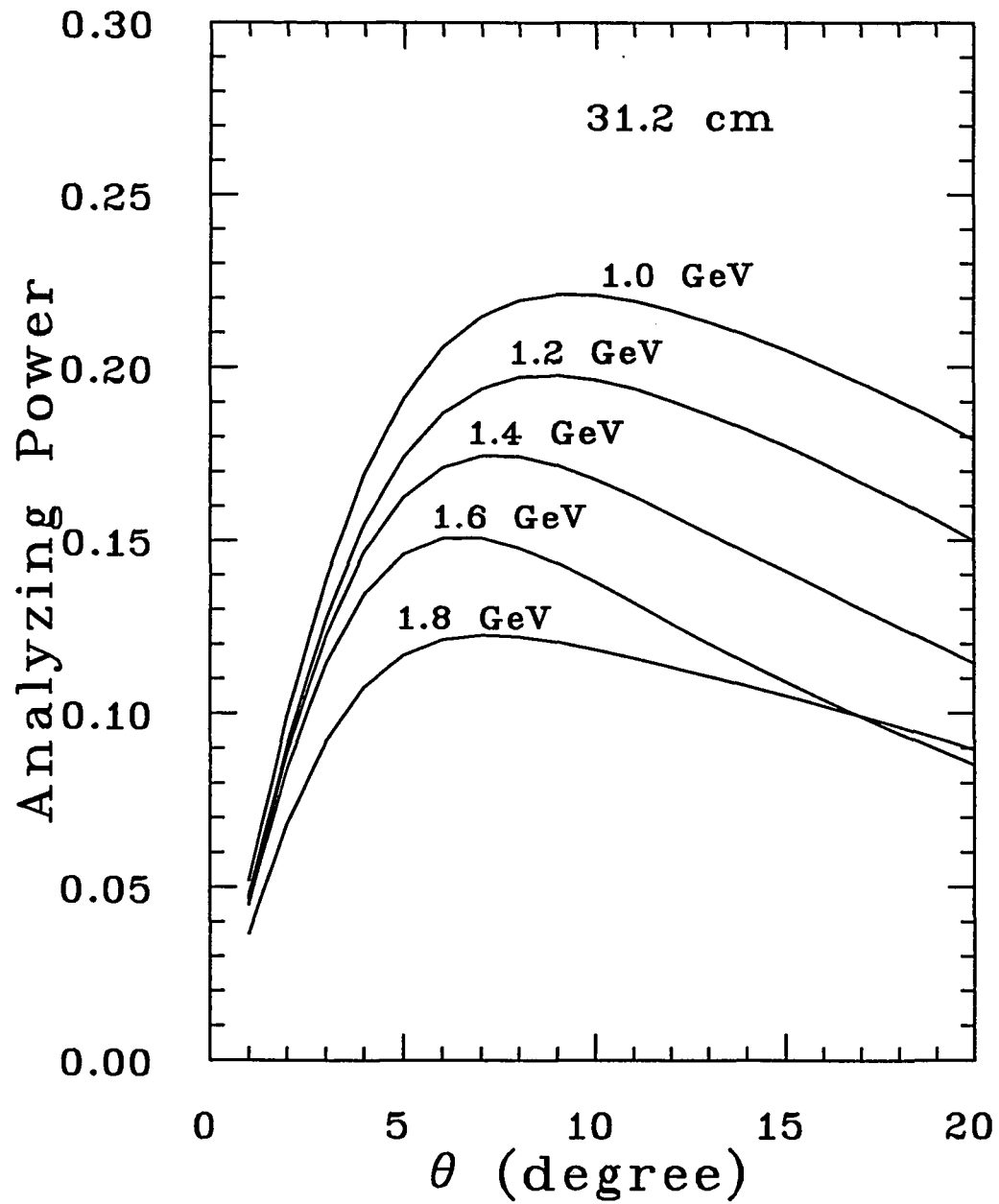


Figure 3-13: The pC analyzing power fit between $T_p=1.0$ and 1.8 GeV.

a polarimeter. It is given by

$$F = \iint \varepsilon(\theta, \phi) A^2(\theta) \cos^2 \phi \, d\theta \, d\phi, \quad (3-47)$$

which is integrated over the solid angle sustained by the device. $A(\theta)$ is the analyzing power and $\varepsilon(\theta, \phi)$ is the polarimeter efficiency defined by

$$\varepsilon(\theta, \phi) = \frac{m(\theta, \phi)}{N_{inc}}, \quad (3-48)$$

where $m(\theta, \phi)$ is given in Equation 3-17 and N_{inc} is the number of incoming protons in POMME. Assuming the detection efficiency D is independent of ϕ , one has

$$\varepsilon(\theta, \phi) = \varepsilon_o(\theta) [1 + P_y A_c(\theta) \cos \phi]. \quad (3-49)$$

The figure of merit becomes

$$F = \int \varepsilon_o(\theta) A^2(\theta) \, d\theta \int [1 + P_y A_c(\theta) \cos \phi] \cos^2 \phi \, d\phi. \quad (3-50)$$

For a simple two-arm, left-right polarimeter, one has

$$\begin{aligned} F &= 2\Delta\phi \int \varepsilon_o(\theta) A^2(\theta) \, d\theta \\ &= \int \varepsilon_{LR}(\theta) A^2(\theta) \, d\theta \end{aligned} \quad (3-51)$$

with

$$\varepsilon_{LR}(\theta) = 2\Delta\phi \varepsilon_o(\theta), \quad (3-52)$$

where $\Delta\phi$ is the angular width of the detectors.

For a 2π polarimeter like POMME, the figure of merit is given by

$$\begin{aligned} F &= \int \varepsilon_o(\theta) A^2(\theta) \, d\theta \int_0^{2\pi} [1 + P_y A_c(\theta) \cos \phi] \cos^2 \phi \, d\phi \\ &= \pi \int \varepsilon_o(\theta) A^2(\theta) \, d\theta \\ &= \frac{1}{2} \int \varepsilon_{2\pi}(\theta) A^2(\theta) \, d\theta \end{aligned} \quad (3-53)$$

with

$$\varepsilon_{2\pi}(\theta) = 2\pi \varepsilon_o(\theta). \quad (3-54)$$

T_p (GeV)	N_{inc} $\times 10^6$	Figure of merit $\times 10^{-4}$	Absolute polarization uncertainty
1.05	1.77	25.0	0.015
1.14	1.83	19.5	0.017
1.24	2.28	12.2	0.019
1.35	1.81	14.2	0.020
1.47	2.19	13.0	0.019
1.59	2.95	11.1	0.017
1.72	4.22	8.0	0.017
1.84	2.92	5.1	0.026

Table 3-9: The figure of merit of POMME and the estimated statistical uncertainty of the measured proton polarization.

The absolute statistical uncertainty on the polarization measured by a polarimeter is simply given by

$$\Delta P \simeq \frac{1}{\sqrt{F N_{inc}}}. \quad (3-55)$$

So, the figure of merit is a very important quantity to determine the number of events one has to acquire during the experiment so as to achieve a particular absolute uncertainty for the polarization. The values of F at different data points together with the corresponding absolute polarization uncertainties calculated by the Equation 3-55 are given in Table 3-9. These estimated statistical errors agree very well with the results obtained from the complete error analysis which are shown in Table 3-10.

A very important aspect of F is that its value depends not only on the hardware of the polarimeter, but also on the way the “useful” events were selected. Those events are used to determine the efficiency ϵ .

3.7 Polarization Transfer

3.7.1 Proton Polarization

During the polarization transfer experiment, a 2.1 GeV vector polarized deuteron beam was directed onto a 4cm thick hydrogen target. The deuterons broke up at

the hydrogen target and the emerging protons were detected at 0° . The momentum and polarization of the protons were measured. Eight data points were obtained with detected proton momenta between 1.75 and 2.61 GeV/c. The detailed discussion of the experimental set-up can be found in Chapter 2.

The polarization axis of the deuteron beam was in the vertical direction. The emerging protons measured at 0° were expected to also have their polarization in the vertical direction. For each data point, the angular distribution of the protons were Fourier analyzed as described in section 3.5. For the present experiment, the coefficient of the sine term, $b_1(\theta_i)$, from the analysis should be very small when compared with the coefficient of the cosine term, $a_1(\theta_i)$.

The proton polarization is given by

$$a_1(\theta_i) = \bar{P}_y A_c(\theta_i) \quad (3-56)$$

$$b_1(\theta_i) = -\bar{P}_x A_c(\theta_i) \quad (3-57)$$

where \bar{P}_y and \bar{P}_x are the projections of the measured proton polarization on the vertical and horizontal axis, respectively. Beside the asymmetries, a_1 and b_1 , we need to know the analyzing power, A_c , in order to find the polarization.

For every data point, the momentum distribution of the protons was calculated with the help of the transport coefficients of SPES4 as described in Section 3.3. The normalized momentum distribution, $f(p)$, of the proton momentum was used to calculate the effective analyzing power as

$$A_c(\theta_i) = \int \int_{\theta_i - \frac{\Delta\theta}{2}}^{\theta_i + \frac{\Delta\theta}{2}} f(p) A(\theta, p) d\theta dp \quad (3-58)$$

with

$$\int f(p) dp = 1. \quad (3-59)$$

p is the proton momentum at the middle of the carbon block. $\Delta\theta$ is the bin width of θ , which was chosen to be 1° . $A(\theta, p)$ is the analytical fit of the analyzing power discussed

in section 3.6.

For every degree of θ , the proton polarization was calculated as

$$(P_y)_i = \frac{a_1(\theta_i)}{A_c(\theta_i)} \quad (3-60)$$

$$(P_x)_i = \frac{b_1(\theta_i)}{A_c(\theta_i)} \quad (3-61)$$

with the error bars

$$\delta(P_y)_i = \frac{\delta a_1(\theta_i)}{A_c(\theta_i)} \quad (3-62)$$

$$\delta(P_x)_i = \frac{\delta b_1(\theta_i)}{A_c(\theta_i)}, \quad (3-63)$$

where δa_1 and δb_1 are given by Equation 3-39 and 3-40, respectively. The results from one of the data points are shown in Figure 3-14.

Finally, the weighted averages were calculated for θ between 3° and 20° as

$$\bar{P}_y = \frac{\sum_{i=3}^{20} \frac{(P_y)_i}{[\delta(P_y)_i]^2}}{\sum_{i=3}^{20} \frac{1}{[\delta(P_y)_i]^2}} \quad (3-64)$$

$$\bar{P}_x = \frac{\sum_{i=3}^{20} \frac{(P_x)_i}{[\delta(P_x)_i]^2}}{\sum_{i=3}^{20} \frac{1}{[\delta(P_x)_i]^2}} \quad (3-65)$$

with the corresponding error bars

$$\delta \bar{P}_y = \sqrt{\frac{1}{\sum_{i=3}^{20} \frac{1}{[\delta(P_y)_i]^2}}} \quad (3-66)$$

$$\delta \bar{P}_x = \sqrt{\frac{1}{\sum_{i=3}^{20} \frac{1}{[\delta(P_x)_i]^2}}} \quad (3-67)$$

The results are summarized in the table 3-10. As the results indicate, \bar{P}_x is indeed compatible with zero to within the error bars. The magnitude of the average proton polarization is given by

$$\begin{aligned} P_p &= \sqrt{\bar{P}_y^2 + \bar{P}_x^2} \quad (3-68) \\ &\simeq \bar{P}_y \end{aligned}$$

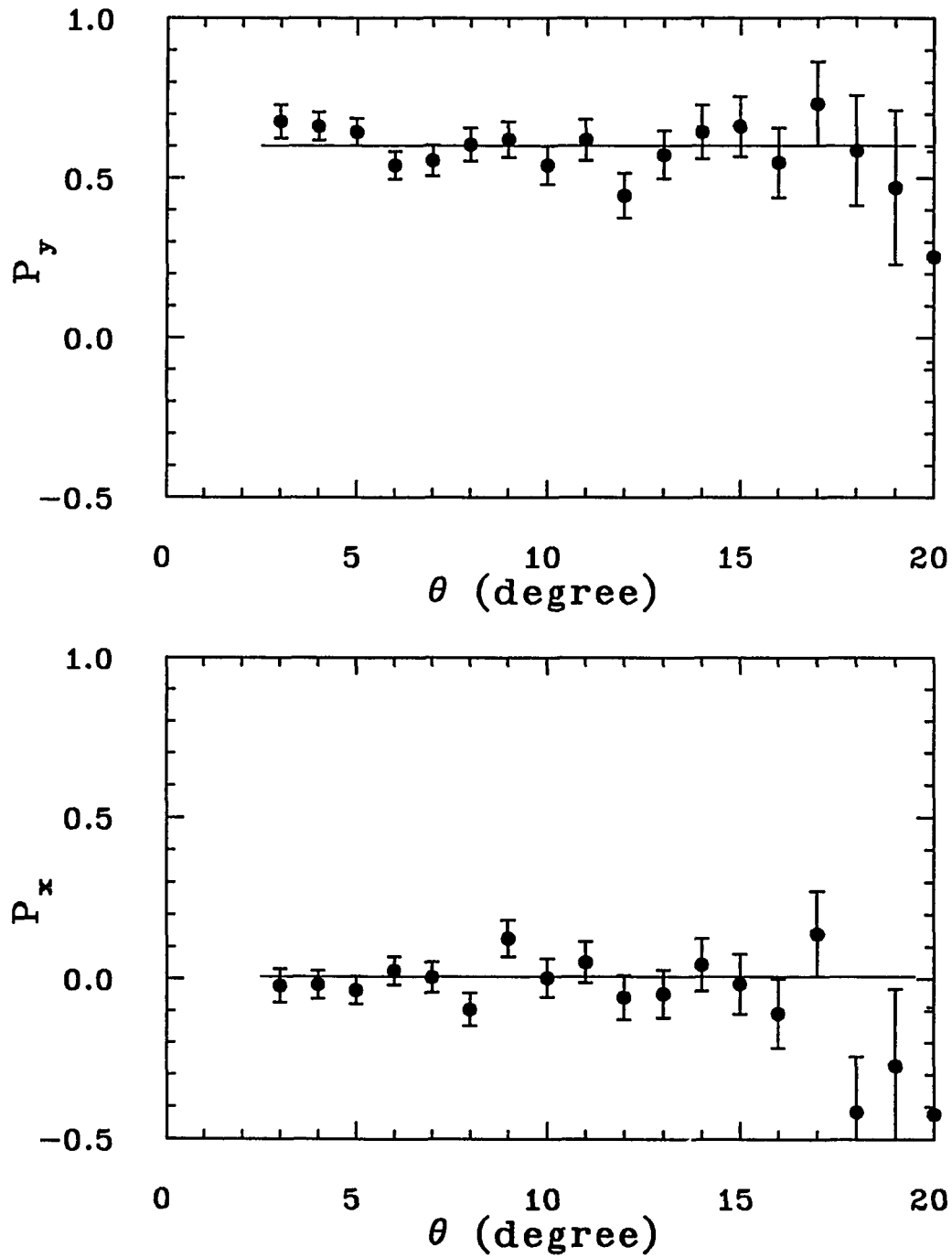


Figure 3-14: P_y and P_x of the data point with SPES4 setting of 1.75 GeV/c. The solid lines are the weighted average.

p/z setting (GeV/c)	$P_{p,lab}$ (GeV/c)	\bar{P}_y	\bar{P}_x
1.75	1.756	0.601 ± 0.015	0.009 ± 0.015
1.85	1.840	0.599 ± 0.017	0.010 ± 0.017
1.97	1.962	0.608 ± 0.019	-0.015 ± 0.019
2.09	2.084	0.535 ± 0.020	0.019 ± 0.020
2.22	2.220	0.330 ± 0.019	-0.000 ± 0.019
2.35	2.355	0.122 ± 0.018	0.013 ± 0.018
2.49	2.496	-0.116 ± 0.017	0.017 ± 0.017
2.61	2.602	-0.193 ± 0.026	-0.023 ± 0.026

Table 3-10: The measured proton polarization for each data point.

3.7.2 Polarization Transfer Coefficient

The polarization of a particle beam from an ion source always has an axial symmetry because of the magnetic field present in the polarized source. Four quantities are needed to describe such a deuteron beam: two angles to determine the direction of the quantization axis in space, as well as the vector polarization P_Z and the tensor polarization P_{ZZ} of the beam. For the experiment discussed here, the polarization axis is in the vertical direction. The two polarizations, in terms of Cartesian tensors, are given by:

$$P_Z \equiv \frac{n^+ - n^-}{n^+ + n^- + n^0}, \quad (3-69)$$

$$P_{ZZ} \equiv \frac{n^+ - n^- - 2n^0}{n^+ + n^- + n^0}, \quad (3-70)$$

where n^+, n^-, n^0 are the number of deuterons in the magnetic sub-state with $m_z = 1, -1, 0$. The deuteron beam in this experiment was purely vector polarized with no tensor component in it. Under this condition, the maximum possible magnitude of the vector polarization is $2/3$. It is accomplished by having either ($n^+ = 2/3, n^- = 0, n^0 = 1/3$), or ($n^+ = 0, n^- = 2/3, n^0 = 1/3$).

The polarization transfer coefficient, κ , is defined by

$$\kappa \equiv \frac{P_p}{P_Z}, \quad (3-71)$$

measurement	asymmetry, \bar{X}
1	0.2135 ± 0.0150
2	0.2143 ± 0.0054
3	0.2216 ± 0.0058
4	0.2180 ± 0.0068
5	0.2191 ± 0.0064

Table 3-11: Asymmetry measurements from the Deuteron Beam Polarimeter.

where P_p is the proton polarization measured with POMME. In the special case of this experiment where $P_{ZZ} = 0$, we then define

$$\kappa_o \equiv \frac{P_p}{P_Z} \Big|_{P_{ZZ}=0}. \quad (3-72)$$

As demonstrated in Appendix A, the relationship between κ and κ_o is given by

$$\kappa = \frac{\kappa_o}{1 - \frac{1}{2}T_{20}\rho_{20}}, \quad (3-73)$$

where ρ_{20} and T_{20} are the tensor polarization and analyzing power in spherical tensors representation, respectively. As also pointed out in Appendix A, κ_o and the coefficient $\mathcal{K}_y^{y'}$ defined in the review by Ohlsen [Ohl72] are related by

$$\kappa_o = \frac{3}{2}\mathcal{K}_y^{y'}. \quad (3-74)$$

The deuteron beam polarization was measured five times through out the experiment as described in Section 2.5. The intensity of the beam reaching the deuteron polarimeter DBP was adjusted by means of a filter. The typical averaged count rate on both the left and the right silicon detectors of the polarimeter was about 15 counts per beam burst, with the beam burst duration of about 1ms. The results of the five measurements are given in the Table 3-11. Those results have been corrected for the dead-time of the system as described in Appendix B. The weighted average of the five left-right asymmetry measurements, \bar{X} , was found to be

$$\bar{X} = 0.2179 \pm 0.0029 \quad (3-75)$$

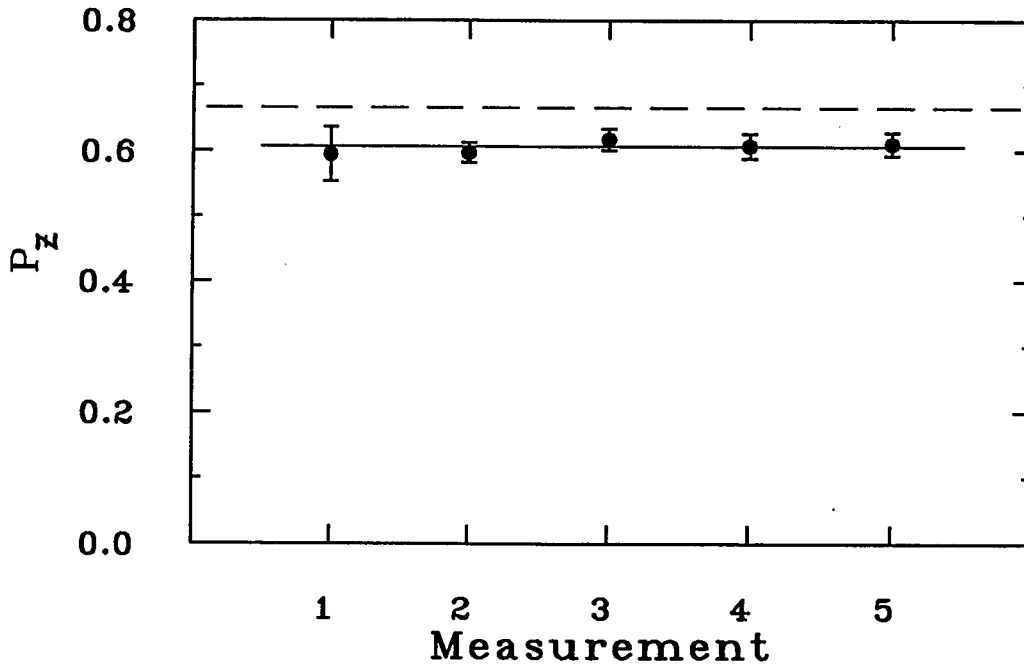


Figure 3-15: Measured beam vector polarization. The solid line is the weighted average. The dashed line is the theoretical maximum polarization ($2/3$) from the ion source, Hyperon.

The deuteron polarization is given by

$$P_Z = \frac{2}{3} \frac{\bar{X}}{A_{DBP}}. \quad (3-76)$$

The value of A_{DBP} used in this analysis was 0.2393 ± 0.0049 which was slightly higher than the 0.2234 ± 0.0046 published value by J. Arvieux, et al. [A⁺88]. The 7% increase in value was due to the dead-time correction and is explained in Appendix B. As shown in Figure 3-15, the deuteron beam polarization was very stable through out the experiment. The average deuteron beam polarization was found to be

$$P_Z = 0.607 \pm 0.015 \quad (3-77)$$

With the beam polarization and the result of the proton polarization measurements given in Table 3-10, the polarization transfer coefficient, κ_o , was calculated and the

p_{mean} (GeV/c)	κ_o	$\delta\kappa_o$
1.756	0.995	0.025
1.840	0.992	0.028
1.962	1.007	0.031
2.084	0.885	0.033
2.220	0.547	0.031
2.355	0.202	0.029
2.496	-0.191	0.029
2.602	-0.320	0.044

Table 3-12: Polarization transfer coefficient, κ_o .

results are shown both in Table 3-12 and Figure 3-16

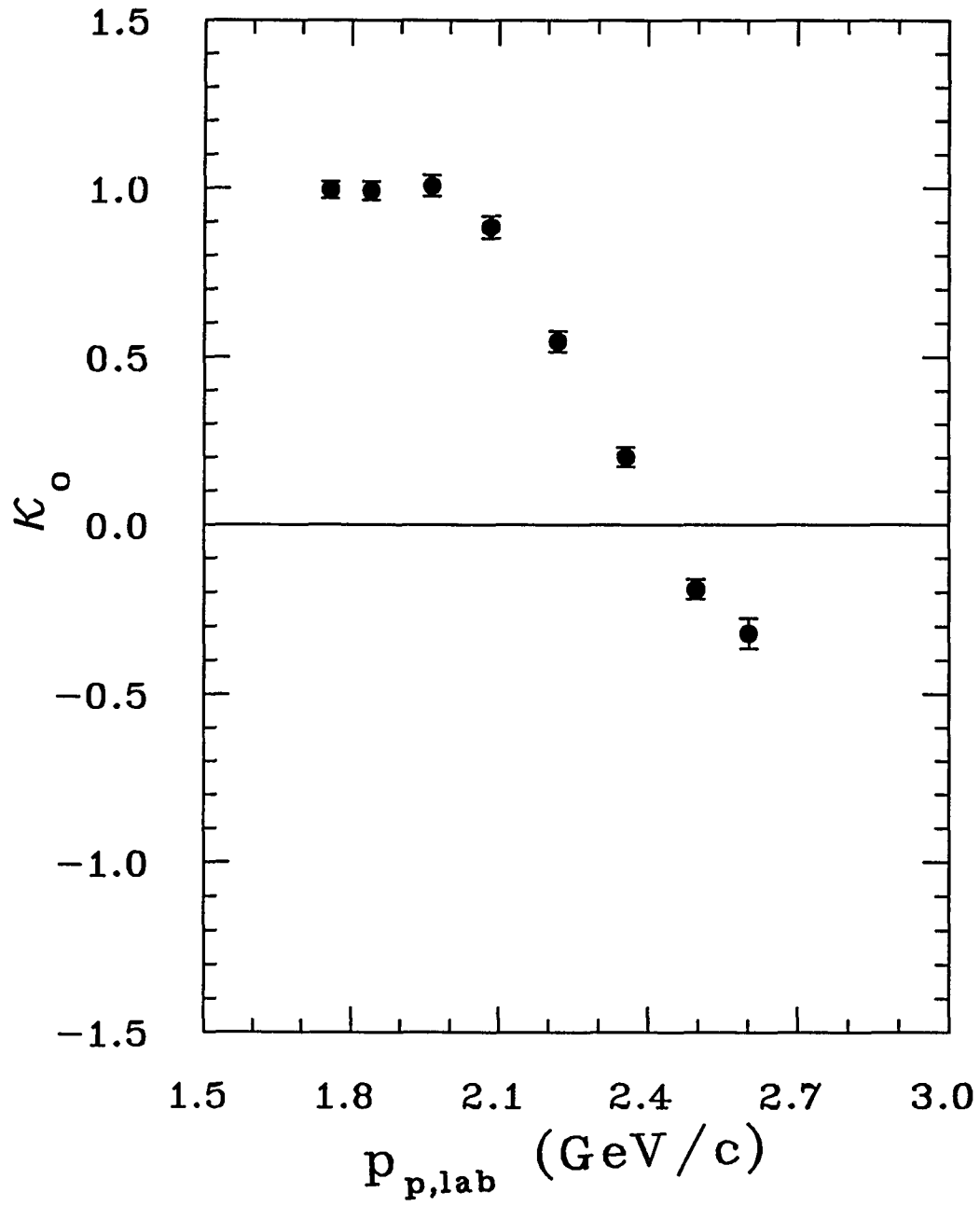


Figure 3-16: Polarization transfer coefficient, κ_0 .

Chapter 4

Results and Discussion

In this chapter, the non-relativistic two-nucleon deuteron wave function will be introduced. Then, the simple relationship between the polarization transfer coefficient, κ_o , and the deuteron wave function will be derived based on the impulse approximation and the proton spectator assumption. The deviation between the experimental result and the impulse approximation prediction will be discussed and possible interpretations of the discrepancy will be given. Finally, the relativistic effects, affecting both the deuteron wave function and the interaction process, will be mentioned briefly.

4.1 Non-relativistic Deuteron Wave Function

In a non-relativistic model, the deuteron is made up of a proton and a neutron except for small NN^* and $\Delta\Delta$ contributions. As mentioned in Chapter 1, the deuteron is a spin-1 particle in a two-nucleon isospin-singlet state. In general, its wave function can be written as:

$$\Psi_d(\vec{r}) = c_+ \Psi_+(\vec{r}) + c_o \Psi_o(\vec{r}) + c_- \Psi_-(\vec{r}), \quad (4-1)$$

where

$$\begin{aligned} c_+ &= \langle \Psi_+ | \Psi_d \rangle \\ c_o &= \langle \Psi_o | \Psi_d \rangle \\ c_- &= \langle \Psi_- | \Psi_d \rangle \end{aligned} \quad (4-2)$$

and

$$c_+^2 + c_o^2 + c_-^2 = 1 \quad (4-3)$$

Ψ_+ , Ψ_0 and Ψ_- are the deuteron wave functions with spin projection onto the quantization axis equals to +1, 0 and -1, respectively.

The wave function of the deuteron is the product of a radial part, an angular orbital part and a spin part. The dominant part of the orbital deuteron wave function is the S -state with $L = 0$. There is also about 6% of D -state ($L = 2$) present in the deuteron. The configuration space wave function of a deuteron with spin in $+z$ direction (the "spin up" state) is then given as

$$\Psi_+(\vec{r}) = \frac{U(r)}{r} Y_0^0 \xi_1^1 + \frac{W(r)}{r} \left(\sqrt{\frac{1}{10}} Y_2^0 \xi_1^1 - \sqrt{\frac{3}{10}} Y_2^1 \xi_1^0 + \sqrt{\frac{6}{10}} Y_2^2 \xi_1^{-1} \right) \quad (4-4)$$

The numerical factors above are the Clebsch-Gordan coefficients and $Y_l^m(\Theta, \Phi)$ are spherical harmonics functions. $U(r)/r$ and $W(r)/r$ are the radial wave functions of the deuteron for the S and D states, respectively. The spin wave functions, $\xi_s^{m_s}$, of a spin triplet proton-neutron system are given by

$$\begin{aligned} \xi_1^1 &= \alpha_p \alpha_n \\ \xi_1^0 &= \frac{1}{\sqrt{2}} (\alpha_p \beta_n + \beta_p \alpha_n) \\ \xi_1^{-1} &= \beta_p \beta_n, \end{aligned} \quad (4-5)$$

where $\alpha_p(\alpha_n)$ are the spinors for proton(neutron) spin-up state. Similarly, β is the spinor for the spin-down state.

The wave function in Equation 4-4 is written in configuration space (r, Θ, Φ) . The same function can also be expressed in momentum space (k, Θ, Φ) , where k is the momentum of the nucleon with respect to the c.m. of the nucleus. The orbital and spin dependence of the wave function are the same in both spaces. The position- and momentum-space wave functions are related by the Fourier transforms:

$$\begin{aligned} u(k) &= \sqrt{\frac{2}{\pi}} \int \frac{U(r)}{r} j_0(kr) r^2 dr & \frac{U(r)}{r} &= \sqrt{\frac{2}{\pi}} \int u(k) j_0(kr) k^2 dk \\ w(k) &= \sqrt{\frac{2}{\pi}} \int \frac{W(r)}{r} j_2(kr) r^2 dr & \frac{W(r)}{r} &= \sqrt{\frac{2}{\pi}} \int w(k) j_2(kr) k^2 dk \end{aligned} \quad (4-6)$$

The $j_0(kr)$ and $j_2(kr)$ are spherical Bessel functions given as:

$$\begin{aligned} j_0(x) &= \frac{\sin x}{x} \\ j_1(x) &= \frac{\sin x}{x^2} - \frac{\cos x}{x} \\ j_2(x) &= \left(\frac{3}{x^3} - \frac{1}{x}\right) \sin x - \frac{3}{x^2} \cos x \end{aligned} \quad (4-7)$$

The “spin up” wave function in the momentum space then becomes

$$\Psi_+(\vec{k}) = u(k)Y_0^0\xi_1^1 + w(k)\left(\sqrt{\frac{1}{10}}Y_2^0\xi_1^1 - \sqrt{\frac{3}{10}}Y_2^1\xi_1^0 + \sqrt{\frac{6}{10}}Y_2^2\xi_1^{-1}\right) \quad (4-8)$$

Similarly, one has

$$\Psi_o(\vec{k}) = u(k)Y_0^0\xi_1^0 + w(k)\left(\sqrt{\frac{3}{10}}Y_2^{-1}\xi_1^1 - \sqrt{\frac{4}{10}}Y_2^0\xi_1^0 + \sqrt{\frac{3}{10}}Y_2^1\xi_1^{-1}\right) \quad (4-9)$$

$$\Psi_-(\vec{k}) = u(k)Y_0^0\xi_1^{-1} + w(k)\left(\sqrt{\frac{6}{10}}Y_2^{-2}\xi_1^1 - \sqrt{\frac{3}{10}}Y_2^{-1}\xi_1^0 + \sqrt{\frac{1}{10}}Y_2^0\xi_1^{-1}\right) \quad (4-10)$$

Substituting Equation 4-8, 4-9 and 4-10 into Equation 4-1, Ψ_d becomes

A polarized deuteron beam can then be described as an ensemble of deuterons in the “spin up”, “spin 0” and “spin down” states with the corresponding fractional population of η_+^2 , η_o^2 and η_-^2 , respectively, with

$$\eta_+^2 + \eta_o^2 + \eta_-^2 = 1. \quad (4-11)$$

As discussed in Appendix A, the vector and tensor polarization of the deuteron beam are given by

$$P_Z = \eta_+^2 - \eta_-^2, \quad (4-12)$$

$$P_{ZZ} = \eta_+^2 + \eta_-^2 - 2\eta_o^2, \quad (4-13)$$

respectively.

4.2 Proton Spectator Approximation

For the deuteron breakup reaction ${}^1H(\vec{d}, p)X$ with the outgoing protons detected at 0° , the cross section of having the scattered proton with momentum k is given by

Equation A-12 in Appendix A as

$$\sigma(k) = \sigma_o(k) \left[1 - \frac{1}{4} P_{ZZ} A_{zz}(k) \right]. \quad (4-14)$$

The simplest mechanism for this reaction is the impulse approximation (IA) in which the hydrogen target interacts with the neutron inside the deuteron nucleus, through both elastic or inelastic scattering. When enough energy is being transferred to the neutron, the deuteron is broken up. Meanwhile the proton remains as a spectator of the breakup process and does not get involved in any interaction. Since the deuteron has a small nuclear binding energy of 2.2 MeV, the bound proton is close to its mass shell before the deuteron breakup. Based on the impulse approximation and the assumption of proton spectator, one expects that the characteristic of the protons, such as polarization and momentum distribution measured in this experiment, to be about the same as they were inside the deuteron nucleus prior to the reaction. The IA and the proton spectator mechanism enable us to directly relate the measured proton characteristics to the deuteron wave function.

In the experiment, the incident deuteron beam had its polarization in the vertical direction, which is perpendicular to the direction where the protons were detected. This results in restricting $\Theta = \pi/2$ for the spherical harmonic $Y_l^m(\Theta, \Phi)$ in the deuteron wave function in the IA calculation. Notice that Θ and Φ are coordinates in the beam polarization frame which are different from the coordinates in the lab frame, (θ, ϕ) . The relationship between the two frames is given in Appendix A.

Under the IA, the invariant cross section for a deuteron breakup in its rest frame with a proton having momentum k and emerging at $\theta = 0^\circ$ can be written as

$$\begin{aligned} \frac{E_k d\sigma}{k^2 dk} = & [\sigma]_{np}^{total} E_k \int \{ \eta_+^2 \Psi_+^2 + \eta_o^2 \Psi_o^2 + \eta_-^2 \Psi_-^2 \} \delta(\Theta - \pi/2) \\ & [\delta(\Phi - \Phi_o) + \delta(\Phi - (\pi + \Phi_o))] d\Omega \end{aligned} \quad (4-15)$$

where E_k is the energy of the proton with momentum k ,

$$E_k = \sqrt{k^2 + m_p^2}. \quad (4-16)$$

The value of Φ_o is arbitrary, and $[\sigma]_{np}^{total}$ is the total cross section for the np scattering.

Substituting the deuteron wave functions from Equation 4-8, 4-9 and 4-10 with $\Theta = \pi/2$ into Equation 4-15, one obtains

$$\begin{aligned} \frac{E_k d\sigma}{k^2 dk} &= [\sigma]_{np}^{total} \frac{E_k}{4\pi} \left\{ [u^2 \eta_+^2 + w^2 (\frac{1}{8} \eta_+^2 + \frac{9}{8} \eta_-^2) - \frac{uw}{\sqrt{2}} \eta_+^2] \xi_1^1 \xi_1^{1*} \right. \\ &\quad + [u^2 \eta_o^2 + w^2 (\frac{1}{2} \eta_o^2) + \sqrt{2} uw \eta_o^2] \xi_1^0 \xi_1^{0*} \\ &\quad \left. + [u^2 \eta_-^2 + w^2 (\frac{9}{8} \eta_+^2 + \frac{1}{8} \eta_-^2) - \frac{uw}{\sqrt{2}} \eta_-^2] \xi_1^{-1} \xi_1^{-1*} \right\} \\ &= [\sigma]_{np}^{total} \frac{E_k}{4\pi} (u^2 + w^2) \left[1 - \frac{1}{4} \left(\frac{2\sqrt{2}uw - w^2}{u^2 + w^2} \right) (\eta_+^2 + \eta_-^2 - 2\eta_o^2) \right]. \end{aligned} \quad (4-17)$$

For a unpolarized beam with $\eta_+^2 = \eta_-^2 = \eta_o^2 = 1/3$, the invariant cross section is given by

$$\left[\frac{E_k d\sigma}{k^2 dk} \right]_{unpol} = [\sigma]_{np}^{total} \frac{E_k}{4\pi} (u^2 + w^2). \quad (4-18)$$

Equation 4-17 can then be rewritten as:

$$\frac{d\sigma}{dk} = \left[\frac{d\sigma}{dk} \right]_{unpol} \left[1 - \frac{1}{4} \left(\frac{2\sqrt{2}uw - w^2}{u^2 + w^2} \right) P_{ZZ} \right]. \quad (4-19)$$

Comparing Equation 4-19 with Equation 4-14, one has

$$A_{zz} = \frac{2\sqrt{2}uw - w^2}{u^2 + w^2}, \quad (4-20)$$

or in spherical tensor representation

$$T_{20} = \frac{1}{\sqrt{2}} \frac{2\sqrt{2}uw - w^2}{u^2 + w^2}. \quad (4-21)$$

Similarly, the cross section for having a spin-up proton being measured in the final state at 0° is given by

$$\begin{aligned} \frac{E_k d\sigma_{\uparrow}}{k^2 dk} &= [\sigma]_{np}^{total} \frac{E_k}{4\pi} \left\{ [u^2 \eta_+^2 + w^2 (\frac{1}{8} \eta_+^2 + \frac{9}{8} \eta_-^2) - \frac{uw}{\sqrt{2}} \eta_+^2] \right. \\ &\quad \left. + \frac{1}{2} [u^2 \eta_o^2 + w^2 (\frac{1}{2} \eta_o^2) + \sqrt{2} uw \eta_o^2] \right\}. \end{aligned} \quad (4-22)$$

The corresponding cross section for having a spin-down proton is

$$\begin{aligned} \frac{E_k d\sigma_{\downarrow}}{k^2 dk} &= [\sigma]_{np}^{total} \frac{E_k}{4\pi} \left\{ [u^2 \eta_-^2 + w^2 (\frac{9}{8} \eta_+^2 + \frac{1}{8} \eta_-^2) - \frac{uw}{\sqrt{2}} \eta_-^2] \right. \\ &\quad \left. + \frac{1}{2} [u^2 \eta_o^2 + w^2 (\frac{1}{2} \eta_o^2) + \sqrt{2} uw \eta_o^2] \right\}. \end{aligned} \quad (4-23)$$

The proton polarization measured in this experiment is then given as:

$$\begin{aligned} P_p(k) &= \frac{d\sigma_{\uparrow}/dk - d\sigma_{\downarrow}/dk}{d\sigma/dk} \\ &= \frac{(u^2 - w^2 - uw/\sqrt{2})(\eta_+^2 - \eta_-^2)}{(u^2 + w^2)(1 - \frac{1}{4} P_{ZZ} A_{zz})} \end{aligned} \quad (4-24)$$

We define the ratio between P_p and P_Z to be the polarization transfer coefficient κ , such that

$$\begin{aligned} \kappa(k) &= \frac{P_p(k)}{P_Z} \\ &= \frac{u^2(k) - w^2(k) - u(k)w(k)/\sqrt{2}}{(u^2(k) + w^2(k))(1 - \frac{1}{4} P_{ZZ} A_{zz}(k))}. \end{aligned} \quad (4-25)$$

For the present experiment, the deuteron beam was purely vector polarized with $P_{ZZ} = 0$. So we have

$$\begin{aligned} \kappa_o(k) &= \kappa(k)|_{P_{ZZ}=0} \\ &= \frac{u^2(k) - w^2(k) - u(k)w(k)/\sqrt{2}}{u^2(k) + w^2(k)}. \end{aligned} \quad (4-26)$$

As demonstrated in Equation 4-26, if the deuteron wave functions, $u(k)$ and $w(k)$, are given, the polarization transfer coefficient $\kappa_o(k)$ can be calculated in the impulse approximation.

There are many non-relativistic deuteron wave function such as Reid [Rei68], Paris [L+80], Moscow [K+85], Amsterdam [DB89] and Bonn [Mac89]. Those wave functions are very similar to each other in the region where k is less than 300 MeV/c. The Paris wave function was chosen as the basis to calculate κ_o in this thesis. Predictions based on other wave functions can be found in E. Cheung et al. [C+92].

In the Paris NN potential, the long and medium range nucleon-nucleon force is derived from πN and $\pi\pi$ interactions, which include the one-pion-exchange (π), correlated and uncorrelated two-pion-exchange (2π), and ω -exchange (ω) contributions. This long and intermediate range potential is cut off rather sharply at an inter-nucleon distance of ~ 0.8 fm and the short range interaction is described simply by a constant soft core determined phenomenologically by fitting all the known phase shifts ($J \leq 6$) up to 300 MeV and the deuteron parameters. The deuteron wave function of the Paris potential reproduces the low energy properties and the electromagnetic form factor $A(q^2)$ of the deuteron. The predicted value of the asymptotic D- to S-wave ratio, η , is 0.0268, in excellent agreement with the high precision measurements of Reference [L⁺80], 0.0259 ± 0.0007 , and Reference [G⁺80], 0.02649 ± 0.00043 . The numerical solutions for both the u and w wave functions are given in the reference by M. Lacombe et al. [L⁺81].

Before any comparison between the experimental results and the prediction can be made, there is one obstacle which has to be overcome. It is the question of how to relate the measured proton momentum, p_p , to the internal momentum, k , of a nucleon inside the deuteron nucleus. Taking the point of view of the impulse approximation and proton spectator breakup process, the momentum p_p can be Lorentz transformed to the deuteron rest frame by

$$\begin{aligned} q &= \gamma(p_p - \beta E_p) \\ E_p &= \sqrt{p_p^2 + m_p^2}, \end{aligned} \quad (4-27)$$

where m_p is the rest mass of the proton. The momentum q is the proton momentum in the deuteron c.m. frame. With the incident deuteron beam kinetic energy of 2.1 GeV, the values of γ and β are given by

$$\gamma = \frac{E_d}{m_d} = 2.1197$$

p_p (GeV/c)	q (GeV/c)	κ_o
1.756	0.001	0.995 ± 0.025
1.840	0.040	0.992 ± 0.028
1.962	0.094	1.007 ± 0.031
2.084	0.146	0.885 ± 0.033
2.220	0.201	0.547 ± 0.031
2.355	0.254	0.202 ± 0.029
2.496	0.307	-0.191 ± 0.029
2.602	0.346	-0.320 ± 0.044

Table 4-1: Polarization transfer coefficient for different values of q .

$$\beta = \frac{p_d}{E_d} = 0.8817 \quad (4-28)$$

where m_d , E_d and p_d are the rest mass, lab. energy and momentum of the incident deuteron, respectively. If we further assume that the proton is on its mass-shell both before and after the breakup, the momentum q is in fact the internal momentum k and we have

$$q = k . \quad (4-29)$$

This assumption seem to be reasonable for small value of k since the deuteron has a very small nuclear binding energy.

4.3 Interpretations

4.3.1 Non-relativistic view

The results of the measurements of κ_o at different values of q are given in Table 4-1. The data are compared with the IA prediction based on the expression of Equation 4-26 in Figure 4-1. The Paris wave function was used in the calculation. The IA calculation, shown as a solid line, describes the general trend of the data. It predicts the data very well for q less than 100 MeV/c. This result confirms that $q = k$ is indeed valid when k is small. For q greater than 100 MeV/c, the magnitude of κ_o is smaller than the prediction. It is interesting to note that the impulse approximation does predict quite

well that κ_0 becomes 0 at q around 300 MeV/c.

The discrepancy between the data and the IA calculation can be due to a number of sources. Some of the most obvious ones are:

- i the wave function used for the calculation is not “accurate” enough,
- ii contributions from processes other than impulse approximation such as multiple scattering, final states interaction and pion production are not negligible, or
- iii the assumption that $q = k$ is invalid for k larger than 100 MeV/c and a different procedure to determine the internal momentum k is needed in this region.

These possibilities will be examined briefly in the following paragraphs.

The long and medium range parts of the Paris potential are in good agreement with the experiment down to 0.8 fm [L+80]. This indicates that the wave function itself should be accurate up to at least $k = 250$ MeV/c. Another concern is the off mass-shell effect of the bound nucleons. In the deuteron rest frame, the nucleons have an average energy of half the deuteron mass, m_d . At a momentum of 250 MeV/c, the invariant mass, m_x , of the bound nucleon is given by

$$\begin{aligned} m_x &= \sqrt{\left(\frac{m_d}{2}\right)^2 - \left(\frac{250}{c}\right)^2} \\ &= 904 \text{ MeV}/c^2 \end{aligned} \quad (4-30)$$

This gives an off-shellness of 34 MeV/c² or 3.6% of the proton rest mass.

In figure 4-2, the result of the T_{20} measurement at Saclay [PP90, P+89] in the reaction $^1\text{H}(\vec{d}, p)\text{X}$ at 0° shows that the proton spectator approximation describes the data really well when q is below 200 MeV/c. Furthermore, for the inclusive deuteron breakup reaction $^1\text{H}(d, p)\text{X}$, the measurement of the invariant cross section, as shown

in Figure 4-3, agrees also very well with the IA, indicating that the proton spectator process is the dominating mechanism.

Based on the expressions given by Equation 4-21 and 4-26, the relationship between κ_o and T_{20} is governed by an equation of a circle [KPS93],

$$(\kappa_o)^2 + \left(T_{20} + \frac{\sqrt{2}}{4}\right)^2 = \left(\frac{3\sqrt{2}}{4}\right)^2. \quad (4-31)$$

This equation does not depend on the deuteron wave function. It is a direct consequence of the impulse approximation. As shown in figure 4-4, the data are close to the circle when q is less than 100 MeV/c. The data with larger q values tend to spiral inwards away from the circle. All three observables, κ_o , T_{20} and the cross section, indicate that the IA works very well at small q .

On the other hand, it is known that there are also contributions from processes other than IA. For instance, the measured proton can originate from the unpolarized hydrogen target instead of being stripped from the deuteron beam particle. This would certainly reduce the magnitude of the measured proton polarization, and κ_o as well. Many sophisticated and systematic studies of the breakup reaction mechanism other than impulse approximation have been done by a number of authors. They included the effect of the target [Mul91], the role of particle production processes [Mul90], the final state interactions and the re-scattering of the proton [PP90, DL90].

In the study by Perdrisat and Punjabi [PP90], all one- and two-step nucleon-nucleon interactions were taken into consideration. In the frame work of the Feynman diagram approach, there are two diagrams for the one-step process and four for the two-step process. Inelastic processes leading to meson production were excluded from the calculation. The six Feynman diagrams are shown in Figure 4-5. Non-relativistic deuteron wave functions were used. The only relativistic effect taken into account was the Lorentz transformation between different frames.

The result of this multiple scattering calculation for κ_o is shown in Figure 4-6 as the

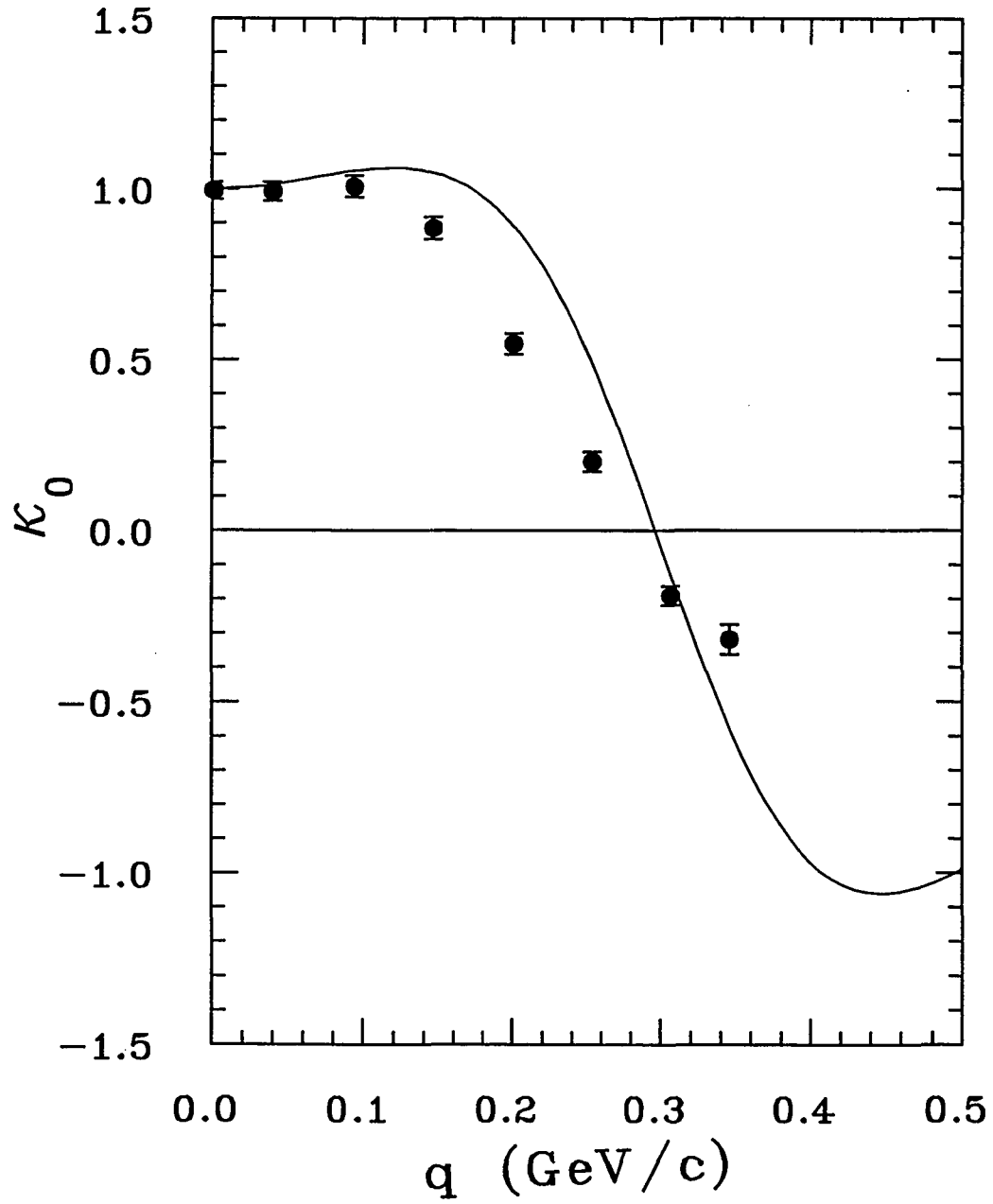


Figure 4-1: Impulse approximation calculation for κ_0 using the Paris wave function.

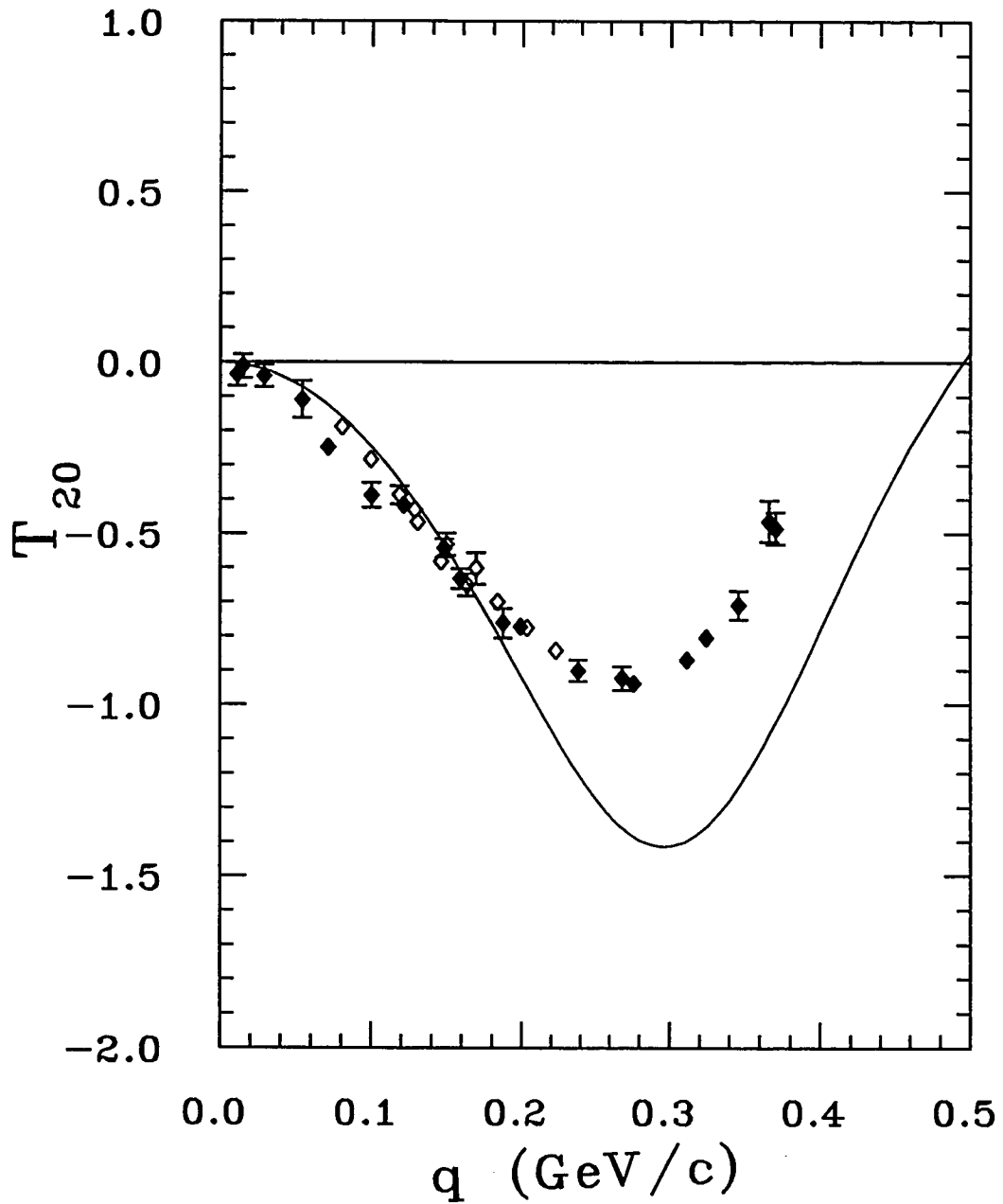


Figure 4-2: Impulse approximation calculation for T_{20} using the Paris wave function. The data are from Reference [PP90] and [P⁺89].

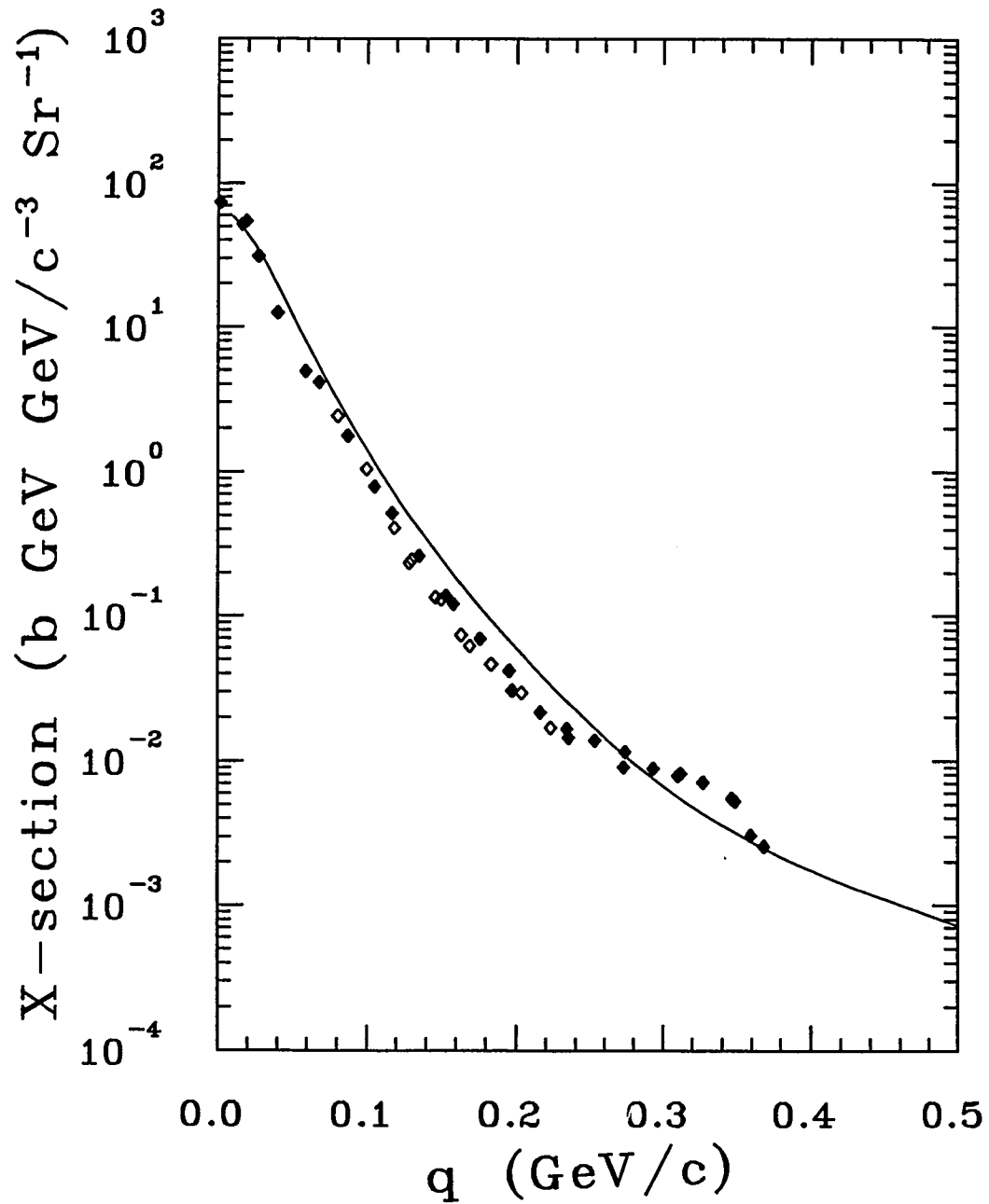


Figure 4-3: Impulse approximation calculation for the invariant cross section using the Paris wave function. The data are from Reference [PP90] and [P+89].

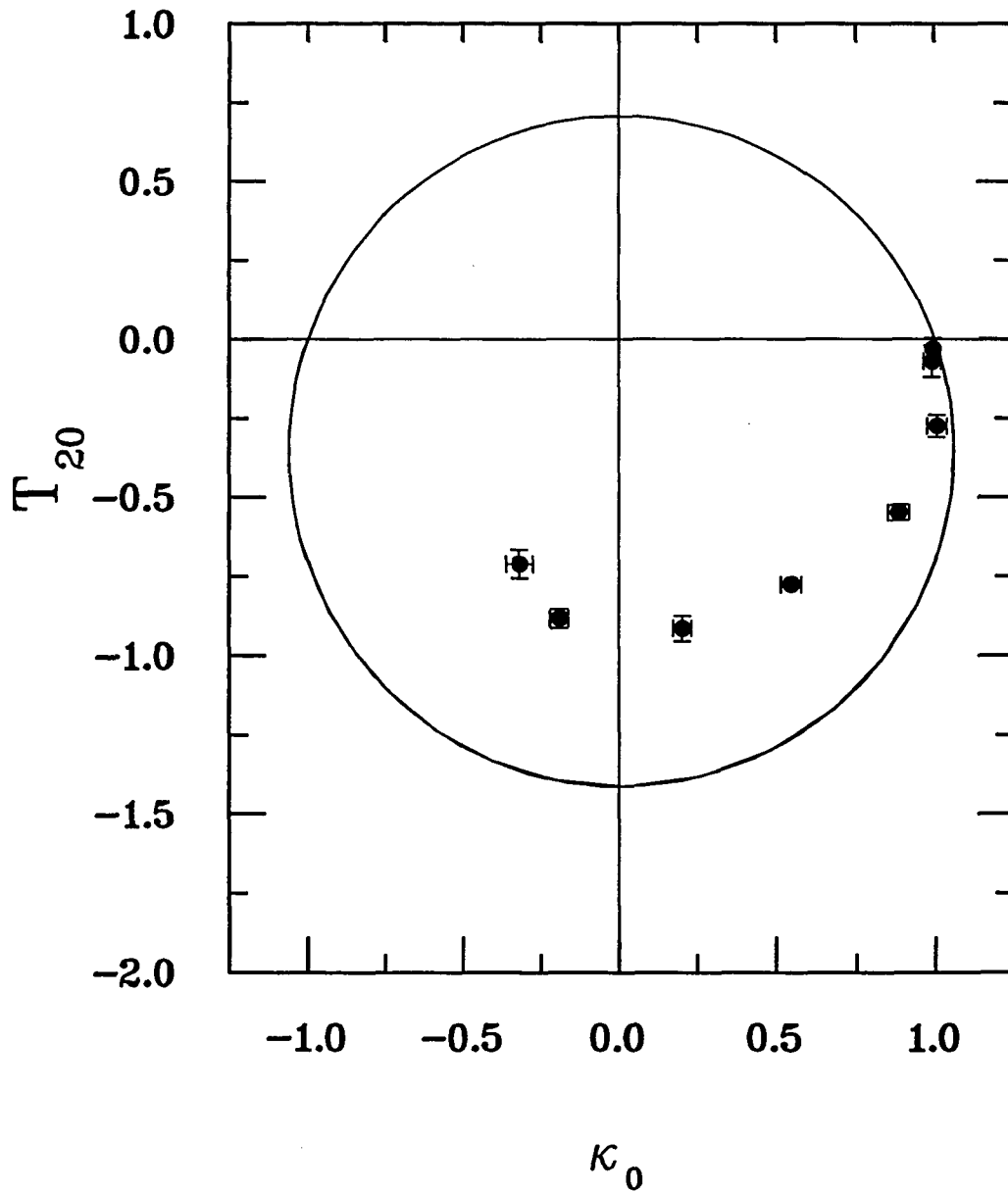


Figure 4-4: Impulse approximation predictions for κ_0 and T_{20} . The solid curve is the IA relationship between κ_0 and T_{20} . For the data points, the values of κ_0 are from the present experiment and the values of T_{20} are extrapolated from Reference [PP90].

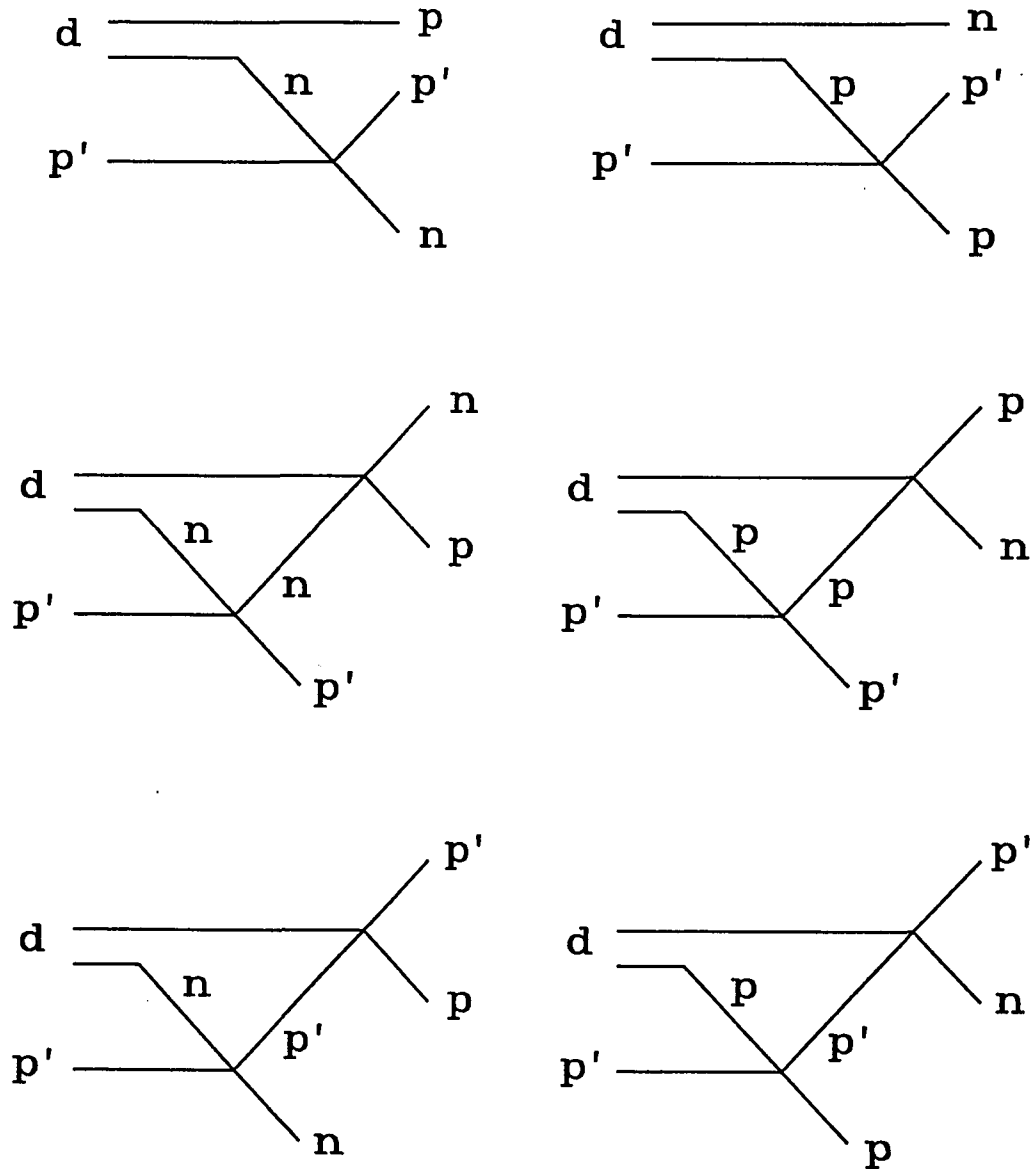


Figure 4-5: The six Feynman diagrams for the non-relativistic multiple scattering calculation. p' is the proton from the target.

dashed line. The IA calculation (solid line) using the Paris wave function is also shown for comparison. The agreement between data and prediction improved for q between 0 and 200 MeV/c with the new calculation. Unfortunately, the disagreement grows when q is larger than 200 MeV/c. The results of the T_{20} measurements of the breakup reaction from References [PP90] and [P+89] are given in Figure 4-7. The same calculation for T_{20} , shown as the dashed line, gives similar results. The agreement improves for small values of q , but gets worse when q becomes large.

The discrepancy is not a surprise since there is no particular reason that this non-relativistic calculation should work in the higher momentum region. In evaluating the double-scattering Feynman diagrams, an integration over the internal loop is performed. This integral involves high momentum components of the deuteron wave function as well as some high energy np and pp interaction vertices. Those high momentum wave functions correspond to the short-range interaction potential. They are determined only phenomenologically in the Paris wave function and have some uncertainty in themselves. Furthermore, as quoted from one of Richard Arndt's articles [Arn88] "studies indicate that throughout the 550 to 800 MeV domain the np interaction remains essentially undefined [by the data]". This certainly limits the accuracy of this non-relativistic Feynman diagram approach calculation. Nevertheless the prediction does give a satisfactory overall description of the data.

Finally, the question of how to define the internal momentum should be studied more closely. The $q = k$ relationship in Equation 4-29 rests on the assumption that the proton is on the mass-shell all the time even when it is bound inside the deuteron nucleus. It is a good approximation when k is less than 100 MeV/c.

In the deuteron rest frame, the two nucleons have equal but opposite momenta. The conservation of energy requires that the sum of their energies be equal to the deuteron

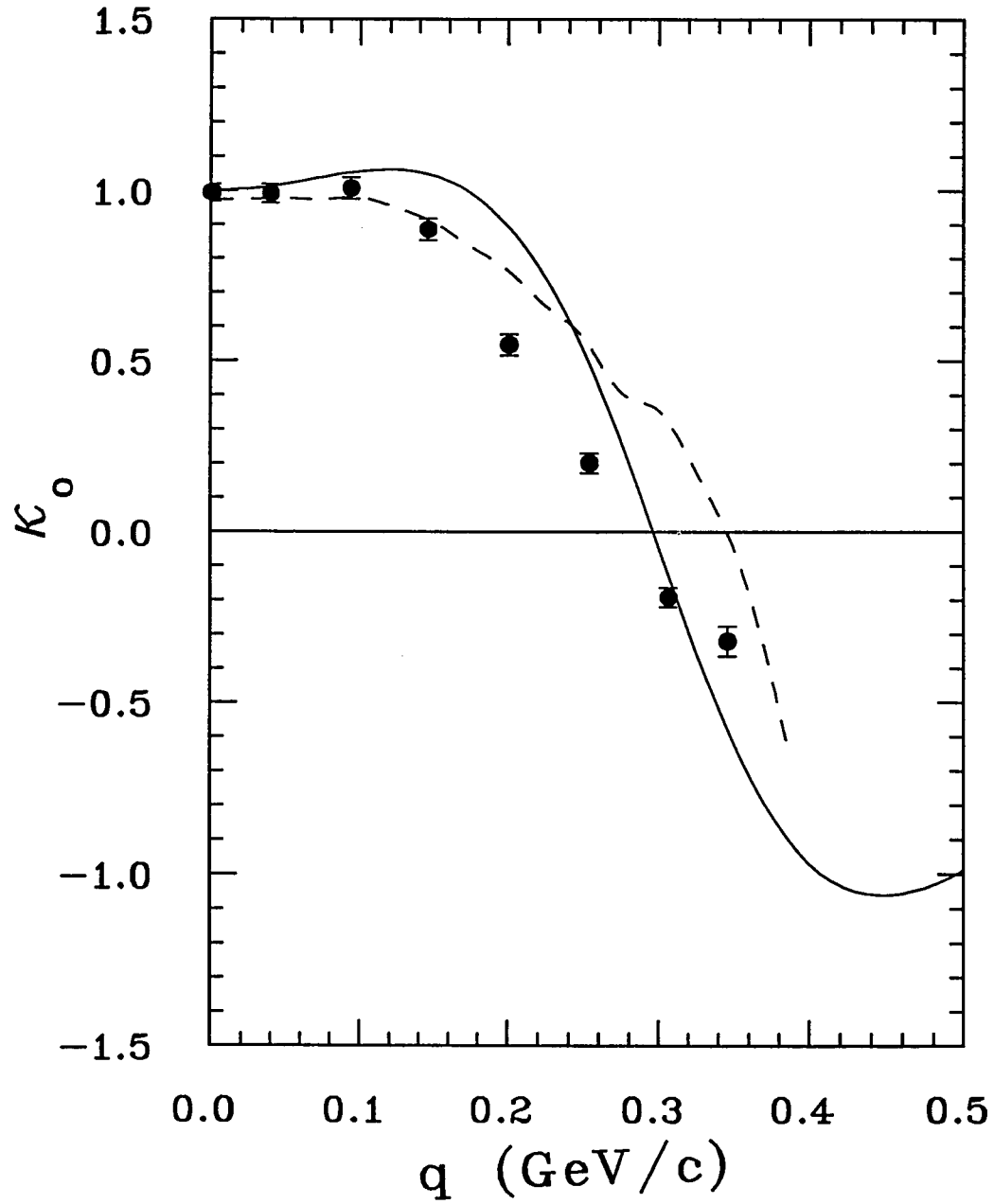


Figure 4-6: Non-relativistic multiple scattering calculation for κ_0 using the Paris wave function (dashed line). The solid line is the IA prediction.

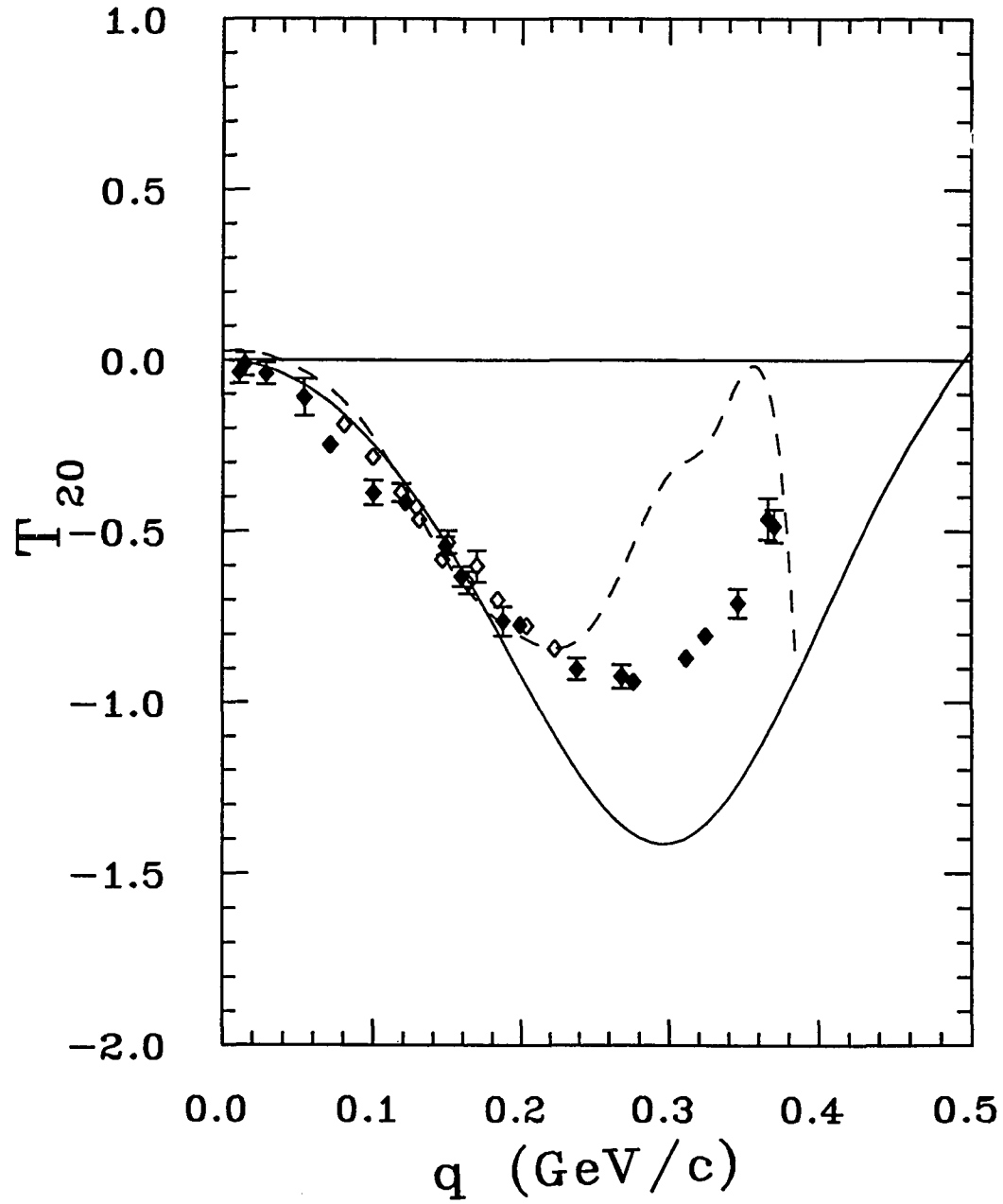


Figure 4-7: Non-relativistic multiple scattering calculation for T_{20} using the Paris wave function (dashed line). The solid line is the IA prediction.

rest mass, m_d . Together with the “proton always on-shell” condition, one has

$$E_p = \sqrt{m_p^2 + k^2} \quad (4-32)$$

$$\begin{aligned} E_n &= m_d - E_p \\ &= \sqrt{m_n^{*2} + k^2}, \end{aligned} \quad (4-33)$$

where m_n^* is the off-shell neutron mass. It is interesting to note that under this assumption, only the neutron is off-shell. It also always has less energy than its partner, the proton. As the value of k becomes larger, the uneven share of energy gets worse. Since the two nucleons are the same particle, only in difference isospin states, there is no particular reason to favour one over the other. It is unlikely that this energy imbalance situation is real. Of course one can always argue that the deuteron breakup only happens when the proton spectator is on-shell. So, the deuteron nucleus does not have an intrinsic energy imbalance between the two nucleons. Only the breakup reaction itself extracts that special portion of the wave function with the proton on-shell. This argument sounds possible but highly unlikely. For instance, if enough energy is transferred from the target to the neutron, there is no reason that the deuteron should not break up only because the proton is off-shell. It is safe to conclude that the “proton always on-shell” model has to be replaced by some more realistic models when k is large.

One possible solution to this energy imbalance problem is to put both the proton and the neutron off-shell and to treat them on an equal footing. By doing so, some kind of interactions have to be introduced to bring the proton from off-shell to on-shell before it can be measured in the lab. This means the proton spectator condition no longer holds and the simple relationship between κ_o and the deuteron wave function given in Equation 4-26 is lost. One way to preserve the proton spectator condition is to put both nucleons on-shell. But it will violate the energy conservation since $E_n + E_p > m_d$ in this case. It looks like there is no simple solution to this problem.

4.3.2 Relativistic Effect

So far in this discussion, the only deuteron wave function employed is non-relativistic. It seems logical to take relativistic effects into account to have a more complete picture of the breakup reaction. The relativistic aspects of the wave function are of principal importance when the high momentum region of the constituents is analyzed in the deuteron rest frame, or when the reaction is described in a frame of reference where the deuteron is travelling at a speed close to the speed of light. Unfortunately the problem of the relativistic description of the deuteron is not uniquely solved. Different procedures of relativisation result in different predictions.

There are two main different approaches to deal with the relativistic theory of a composite system. The first one is based on the summation of a class of perturbation theory diagrams. This approach is based on the field theory which is assumed to describe the physics. The other method is to find a way to boost amplitudes calculated in one special frame to an arbitrary frame. It is a phenomenological approach which is not guided by the fundamental quantum field theory or standard model. Any ambiguities arising from this approach can only be resolved through comparison of model calculations with the data. The advantage of this approaches is that the issue of Lorentz covariance is separated from the dynamics, so that any phenomenological, non-relativistic, or semi-relativistic calculation can be used.

In the field theory approach, one usually solves a Bethe-Salpeter type equation. It involves finding the appropriate propagator, G , describing the propagation of two nucleons, and the potential, V , which includes the Feynman diagrams that describe the interaction. A good example of this approach is given by Gross et. al. in References [BG79] and [GOH92]. They used a propagator which restricts one nucleon to its mass shell. One-boson-exchange (OBE) was used to describe the interactions. The resulting relativistic deuteron wave function (Gross wave function) has four components;

in addition to the familiar S and D states, there are two small P state components, v_t and v_s (for spin-triplet and -singlet), which play a role similar to the small negative-energy components of the Dirac wave function of the hydrogen atom. It should be pointed out that in Gross's approach, the wave function is defined in such a way that the radial wave function of the S and D states in the momentum space have a relative sign that is opposite to the same relative sign in the Paris wave function. We chose to adopt the sign convention of the Paris wave function in this dissertation to keep the discussion more consistent.

The relativistic deuteron wave function can be written in general as

$$\begin{aligned}\Psi_{d,rel} &= \{^3S_1\}part + \{^3D_1\}part + \{^3P_1\}part + \{^1P_1\}part \\ &= u(q)\chi_{^3S_1} + w(q)\chi_{^3D_1} + v_t(q)\chi_{^3P_1} + v_s(q)\chi_{^1P_1}\end{aligned}\quad (4-34)$$

where χ contains the spin and angular wave functions. The wave function is normalized according to

$$\int_0^\infty k^2 dk [u^2(k) + w^2(k) + v_t^2(k) + v_s^2(k)] = 1. \quad (4-35)$$

Using the proton spectator approximation and the impulse approximation, described in Section 4.2, together with this relativistic wave function, one can find the new relationships between the wave functions and the polarization observables, κ_o and T_{20} .

$$\kappa_o = \frac{u^2 - w^2 - \frac{1}{\sqrt{2}}uw + \frac{3}{\sqrt{2}}v_tv_s}{u^2 + w^2 + v_t^2 + v_s^2} \quad (4-36)$$

$$T_{20} = \frac{1}{\sqrt{2}} \frac{2\sqrt{2}uw - w^2 + v_t^2 - 2v_s^2}{u^2 + w^2 + v_t^2 + v_s^2} \quad (4-37)$$

The new relativistic IA predictions for κ_o , T_{20} and the invariant cross section are compared with the data from this experiment and Reference [PP90] in Figure 4-8, 4-9 and 4-10, respectively. The dashed lines are the predictions based on the relativistic wave function from Reference [BG79] (with $\lambda = 0.2$). The IA prediction from the Paris wave function are also shown as the solid lines for comparison. Since the S and the D

states of the Gross wave function are very similar to the non-relativistic Paris wave function and the two P states are relatively small, the new IA results show relatively little difference from the calculations based on the non-relativistic wave function. This demonstrates that the relativisation of the deuteron wave functions in the c.m. frame alone does not account for all the discrepancies between the IA predictions and the data.

The second popular method to handle the relativistic effect of the few-body system is by using the time-ordered perturbation theory in the infinite momentum frame (IMF). In this approach, the amplitudes of the time-ordered diagrams of the reaction are calculated in a special frame travelling at the speed of light in a direction opposite to the observed constituent. In this frame, the momenta of the particles are infinite, thus providing the name, *infinite momentum frame*, for this approach.

For each Feynman diagram of order n (with n vertices), there exist a corresponding $n!$ time-ordered diagrams. In Figure 4-11, a Feynman graph of 3 vertices and its 6 corresponding time-ordered graphs are shown. The direction of time flows from left to right for the time-ordered graphs. In the IMF, only those time-ordered graphs with at least one particle line from the past and at least one line towards the future at each vertex can have a non-zero amplitude. All the other graphs are suppressed in this frame. It is one of the advantages of using the IMF over the field theory Feynman diagram approach since only a fraction of all the time-ordered graphs need to be calculated. In the example given in Figure 4-11, the three time-ordered graphs, (d), (e) and (f), are suppressed in the IMF. Only three graphs out of all six have contributions to the reaction.

There is one problem which needs to be solved before applying the IMF approach to the deuteron breakup reaction. It is the question of how to write down the deuteron wave function, Ψ_{IMF} , in the infinite momentum frame. Unfortunately, up to now there is still no unique way to do it. In general, the Ψ_{IMF} is being expressed in a form that is

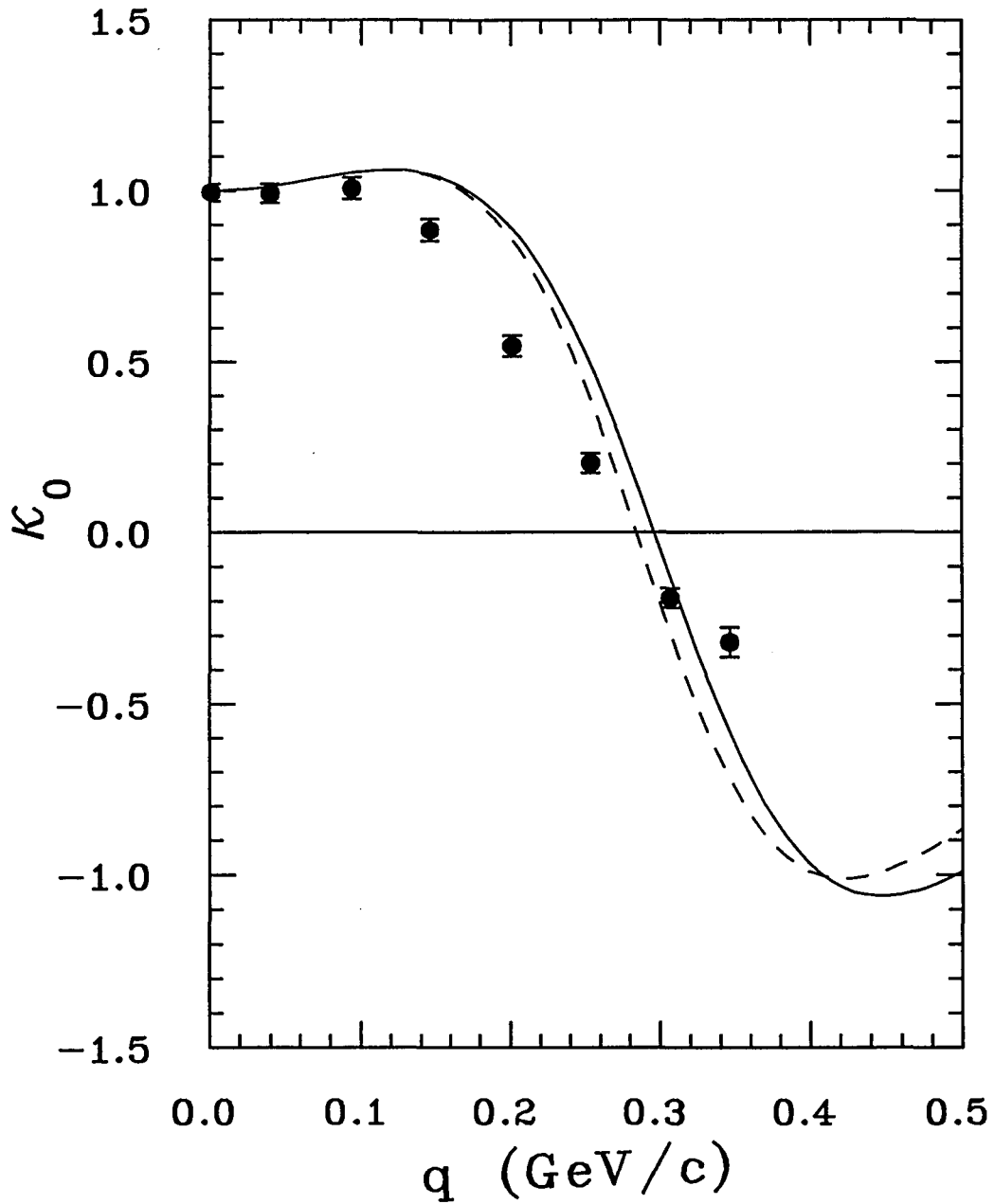


Figure 4-8: Relativistic impulse approximation calculation for κ_0 using the Gross wave function (dashed line). The solid line is the non-relativistic IA prediction using the Paris wave function.

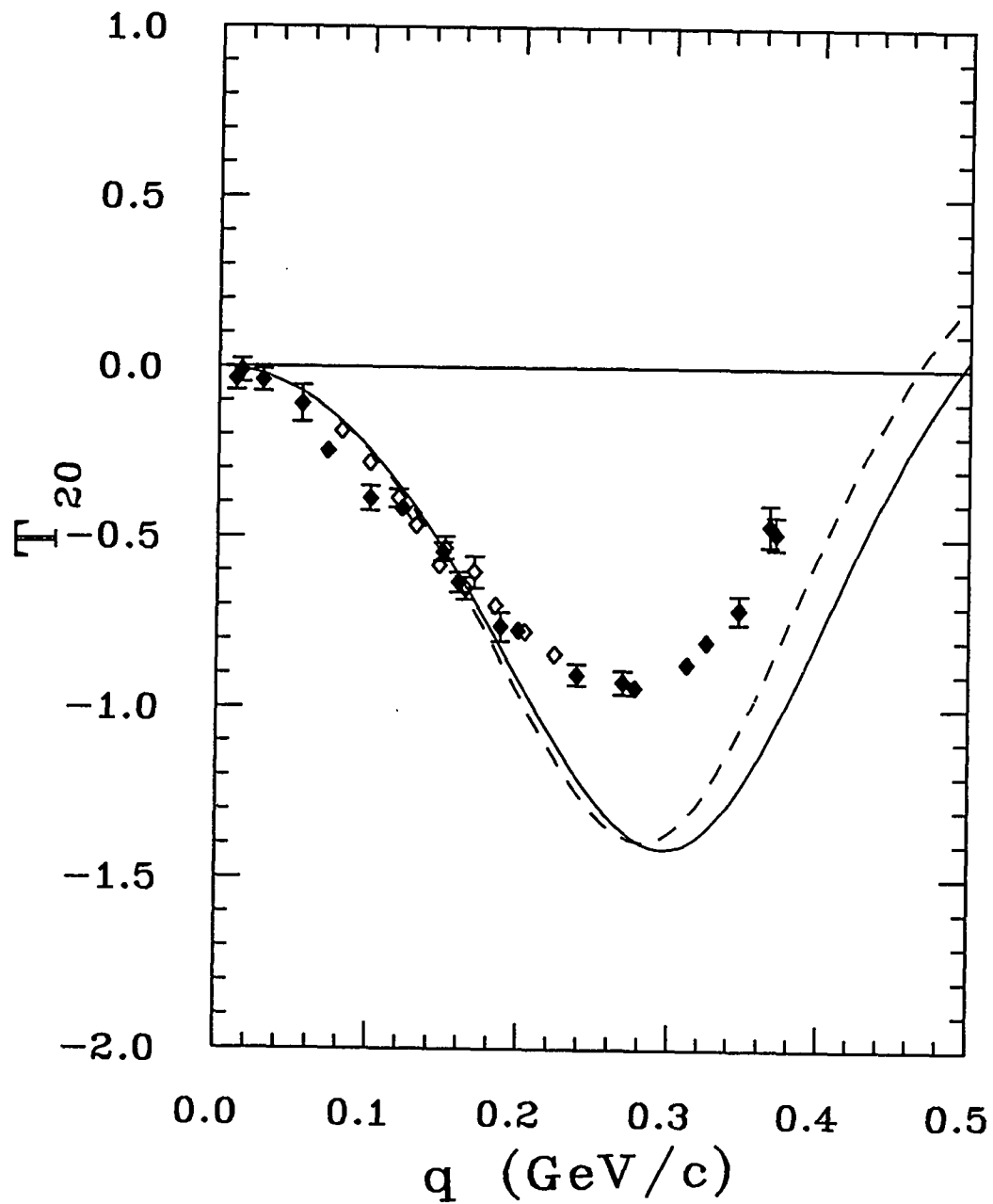


Figure 4-9: Relativistic impulse approximation calculation for T_{20} using the Gross wave function (dashed line). The solid line is the non-relativistic IA prediction using the Paris wave function.

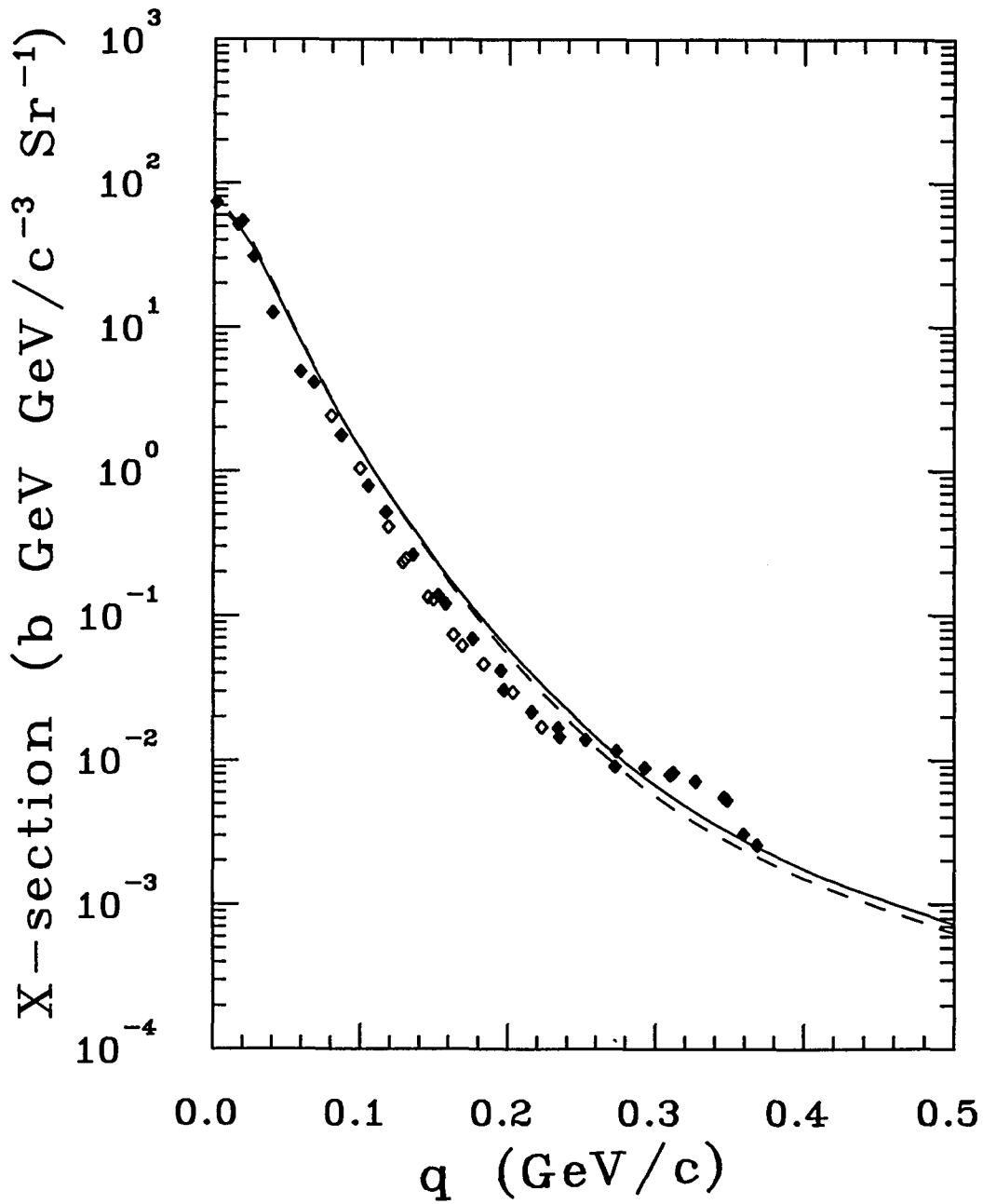
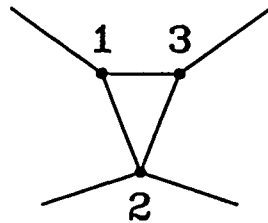


Figure 4-10: Relativistic impulse approximation calculation for the invariant cross section using the Gross wave function (dashed line). The solid line is the non-relativistic IA prediction using the Paris wave function.



Feynman diagram

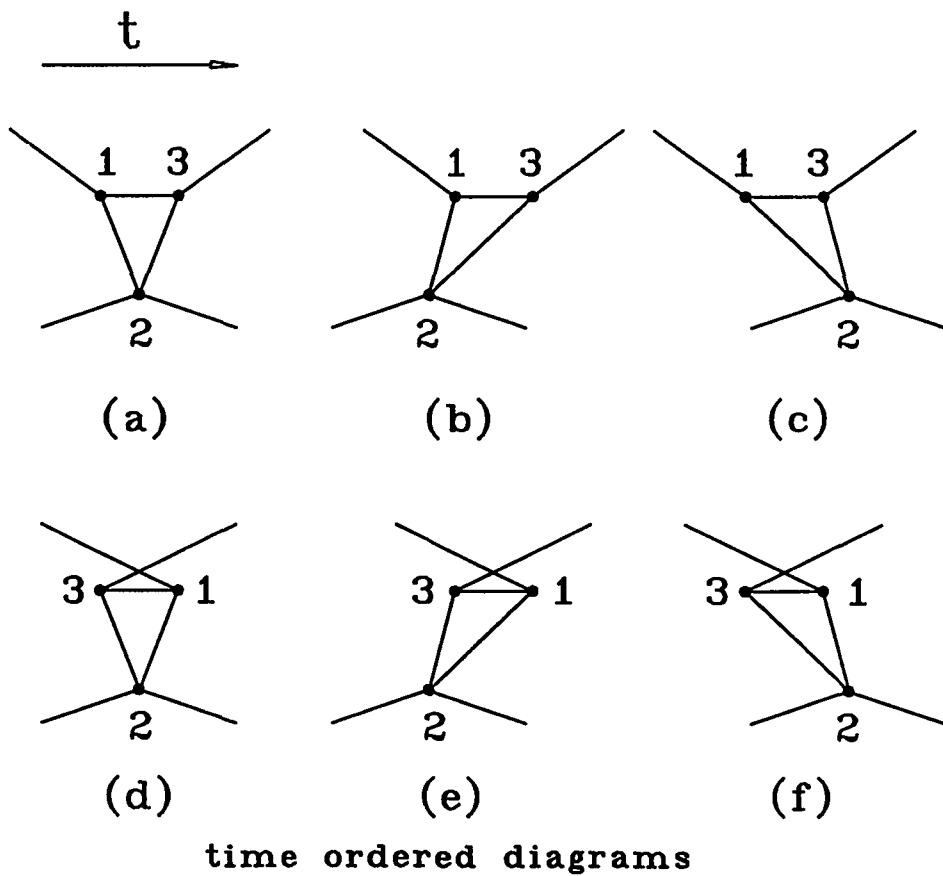


Figure 4-11: A Feynman diagram with 3 vertices and its 6 corresponding time-ordered diagrams.

closely related to the non-relativistic deuteron wave function, such as the Paris or the Bonn wave functions.

In Reference [DL92], Dorodnykh and Lykasov calculated the invariant cross section and the polarization observables for the deuteron breakup reaction with an outgoing proton at 0° using the IMF approach. First, the wave function Ψ_{IMF} was expressed in the following form:

$$\Psi_{IMF}^2(\alpha, k_{IMF}) = \left[\frac{m_N^2}{4\alpha(1-\alpha)} \right]^{\frac{1}{2}} \Psi_d^2(k_{IMF}) \quad (4-38)$$

where Ψ_d is the non-relativistic deuteron wave function. Both α and k_{IMF} are new variables defined as

$$\alpha = \frac{p_p + E_p}{p_d + E_d} = \frac{q + E_q}{m_d}, \quad (4-39)$$

$$k_{IMF}^2 = \frac{m_N^2}{4\alpha(1-\alpha)} - m_N^2 \quad (4-40)$$

where m_d and m_N are the deuteron and nucleon mass. E_p , p_p , E_d and p_d are the energy and momentum of the detected proton and beam deuteron, respectively, while q is the the proton momentum in the deuteron c.m. frame and E_q is the corresponding energy given by

$$E_q^2 = q^2 + m_p^2. \quad (4-41)$$

k_{IMF} , sometime called the light cone variable (LCV) internal momentum, has been proposed as the proper relativistic scaling variable. Its definition depends on the Lorentz invariant α . In the IMF, α is the fraction of the projectile deuteron momentum carried by the proton, and has a value between 0 and 1.

With the wave function Ψ_{IMF} , Dorodnykh and Lykasov calculated both κ_o and T_{20} . They included four additional diagrams besides the impulse approximation. The five diagrams they used are shown in Figure 4-12. In graph (a) is the IA process with the proton from the deuteron nucleus as a spectator. Graph (b) is the proton non-spectator process where the proton from either the deuteron or the target was scattered before

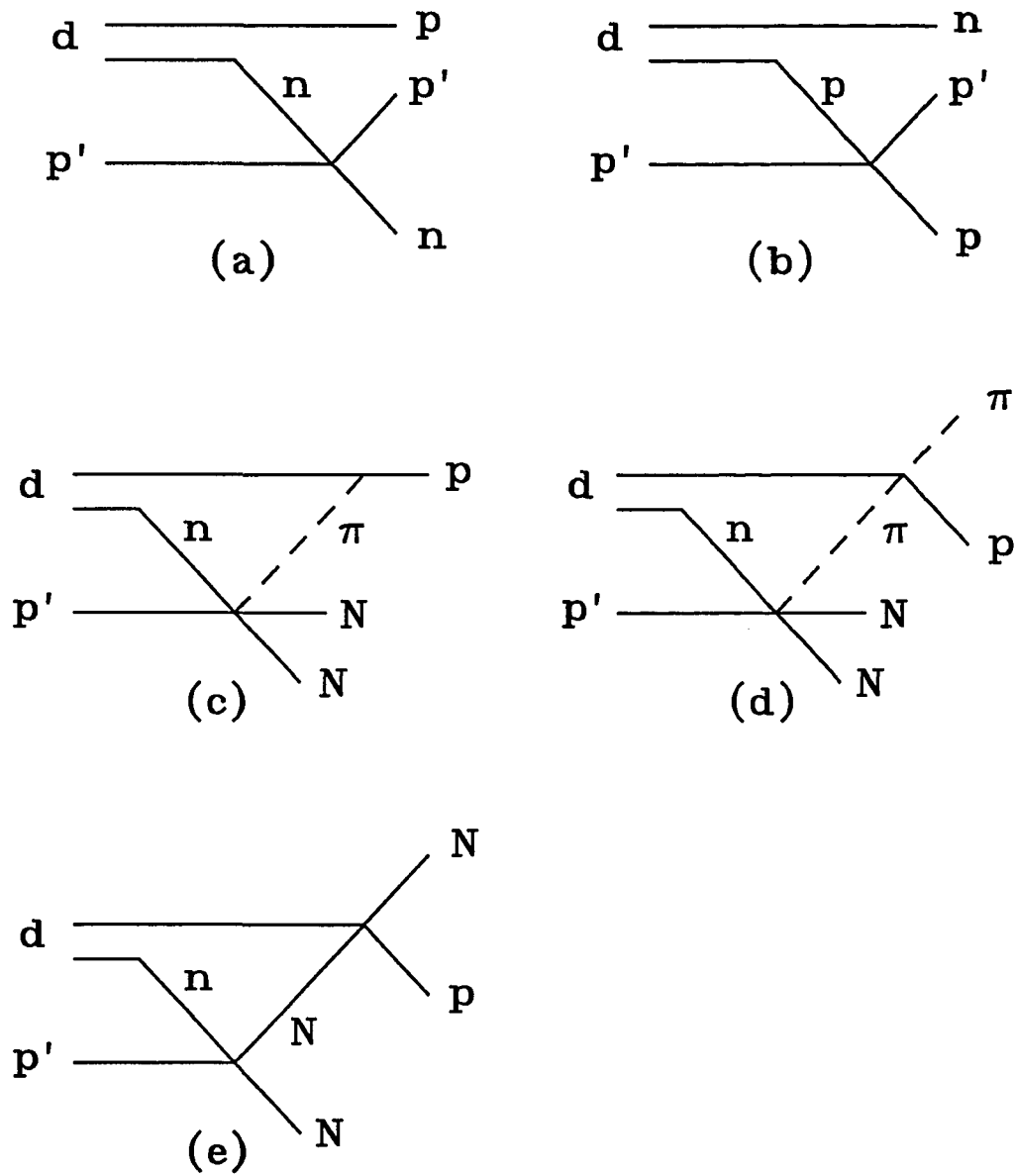


Figure 4-12: The diagrams for the infinite momentum frame (IMF) calculation.

being detected. The other three diagrams are for the higher order “two-step” processes. A pion is created and re-absorbed between the two vertices in graph (c). Only the contributions from the pseudoscalar mesons are included in the intermediate state for this graph. Graph (d) represent the creation and re-scattering of a pion during the deuteron breakup reaction, while graph (e) is for the re-scattering of a nucleon at the upper vertex.

The results of the IMF calculation for κ_o , T_{20} and the invariant cross section are given in Figure 4-13, 4-14 and 4-15, respectively. The solid lines are the non-relativistic IA predictions from the Paris wave function. The dashed lines are the IA predictions using the IMF approach. There is a one-to-one relationship between the momentum q and the variable k_{IMF} , given by Equation 4-39 and 4-40. As a result, the new IA prediction is just a re-scaling of the old prediction by compressing the curve to the left.

The dotted lines are for the complete calculation that included all five time-ordered graphs. These curves, calculated in Reference [DL92], are for a deuteron beam momentum of 9 GeV/c, not 3.5 GeV/c as for the data shown. The amplitudes of the multiple scattering processes besides the IA are in general energy dependent, and so is the result of the complete calculation. Unfortunately, the IMF prediction for the deuteron beam momentum of 3.5 GeV/c is not yet available. We included the results from the 9 GeV/c calculation just to have an idea of how well the IMF approach does. As shown in Figure 4-13, the dotted line provided the best fit to the κ_o data so far. In Figure 4-14, the complete calculation fit the T_{20} nicely up to $q = 0.25$ GeV/c. It predicts the minimum of the data at -0.9 very well. This agreement is a bit surprising since the calculation was not done at the beam energy of the experiment.

4.4 Conclusion

In this thesis, results of the measurement of the polarization transfer coefficient, κ_o , from the deuteron to the proton in the deuteron breakup reaction at 0° are presented.

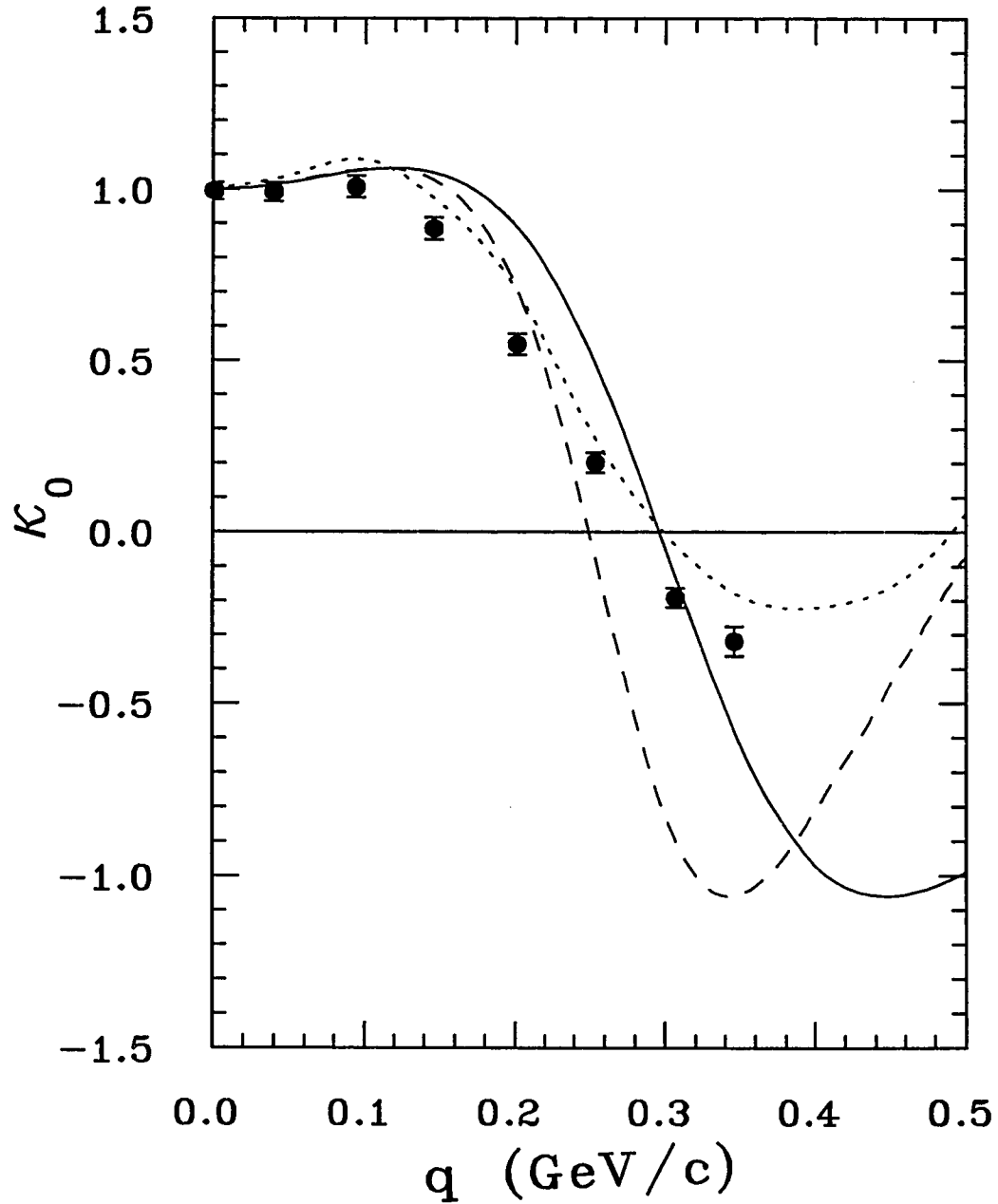


Figure 4-13: Calculation for κ_0 in the infinite momentum frame, using the Paris wave function and the light cone variables. The dashed line and the dotted line are for the IA and the complete calculation in IMF, respectively. The solid line is the non-relativistic IA prediction using the Paris wave function.

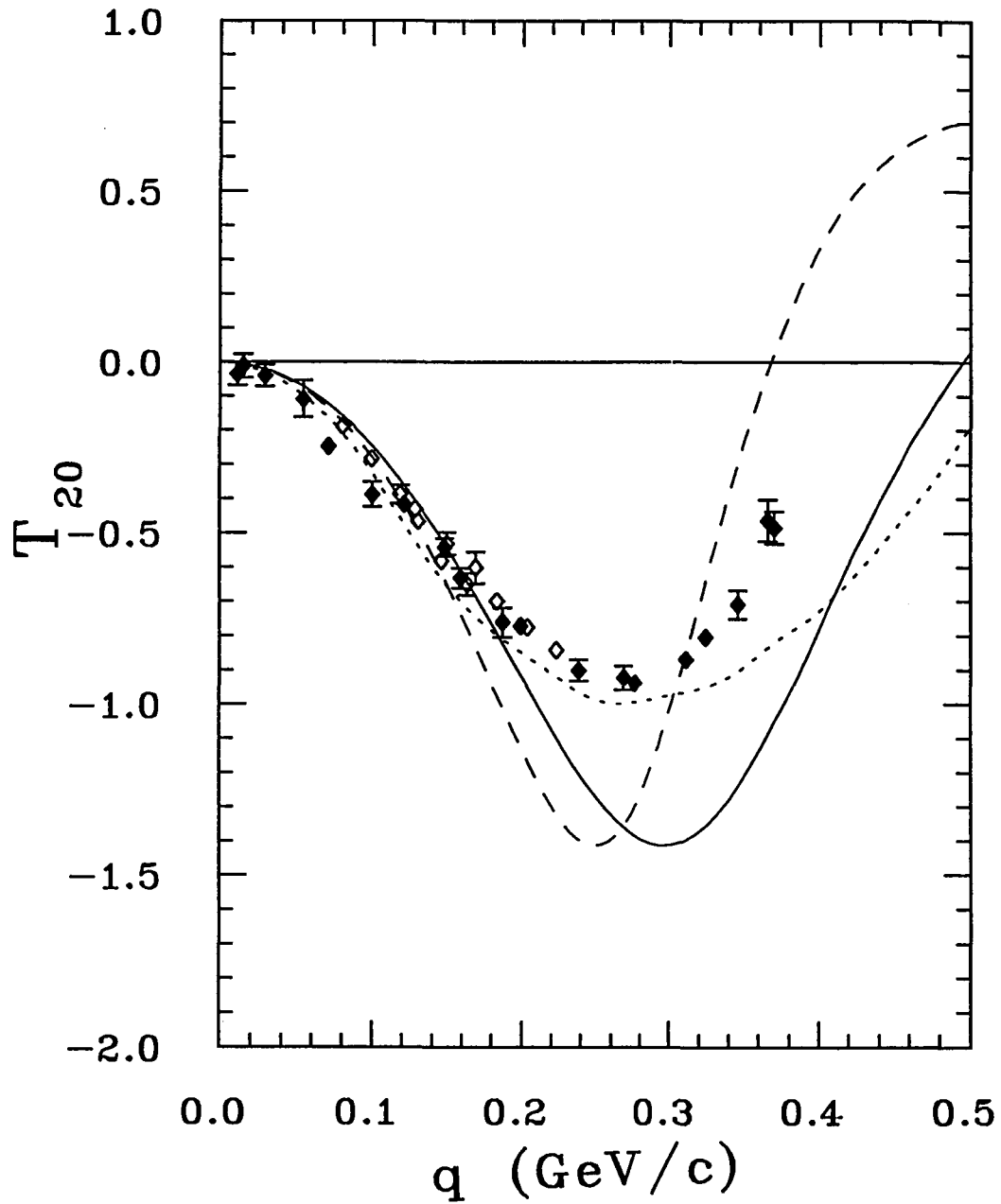


Figure 4-14: Calculation for T_{20} in the infinite momentum frame, using the Paris wave function and the light cone variables. The dashed line and the dotted line are for the IA and the complete calculation in IMF, respectively. The solid line is the non-relativistic IA prediction using the Paris wave function.

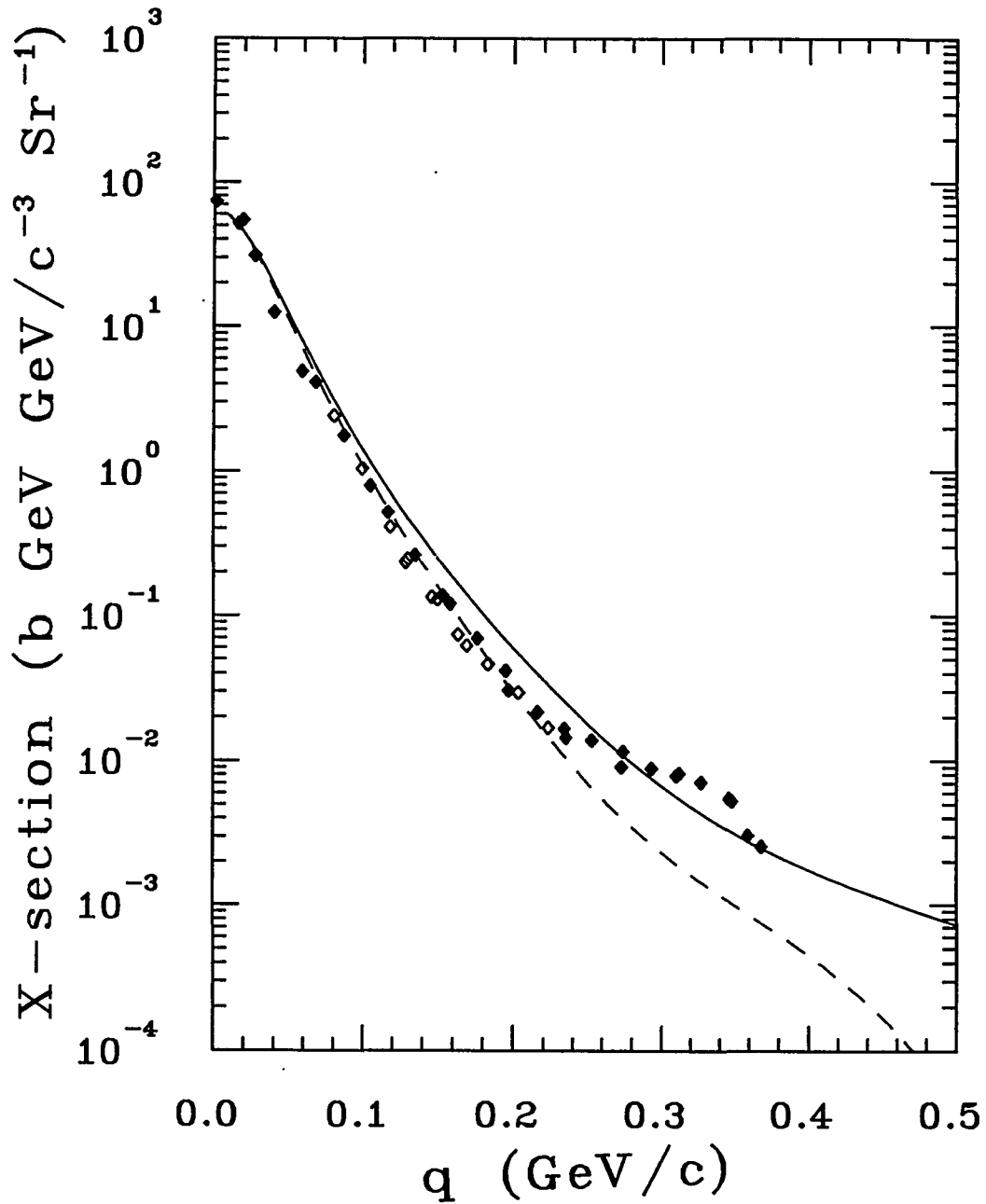


Figure 4-15: Calculation for the invariant cross section in the infinite momentum frame, using the Paris wave function and the light cone variables. The dashed line is for the IA calculation in IMF. The solid line is the non-relativistic IA prediction using the Paris wave function.

The experiment consisted of a 2.1 GeV vector polarized deuteron beam breaking up on a 4 cm liquid hydrogen target. Then the momentum and polarization of the outgoing protons were measured at 0° . Eight κ_o data points at various proton momenta were measured. The κ_o data are discussed together with another polarization observable, the analyzing power T_{20} , measured in previous experiments [PP90].

The results indicate that the impulse approximation with the proton spectator process can describe both polarization observables when the proton momentum in the deuteron c.m. frame, q , is less than 100 MeV/c. The non-relativistic multiple scattering calculation done by Perdrisat and Punjabi [PP90] cannot describe both sets of data beyond $q = 200$ MeV/c. The impulse approximation with the relativistic deuteron wave function (Gross wave function), calculated by Gross et. al. using field theory and one-boson-exchange forces [BG79, GOH92], cannot fully explain the data either. The multiple scattering calculation done by Dorodnykh and Lykasov [DL92] using the infinite momentum frame approach provides the best fits to both κ_o and T_{20} data so far.

From the study of different model dependent calculations, we conclude that the proton spectator approximation together with a non-relativistic deuteron wave function (Paris wave function in this thesis) can describe the general trends of the data of both κ_o and T_{20} in the region where q is between 0 and 400 MeV/c. Meanwhile, the relativistic effects, from both the deuteron wave function itself and the interaction processes, as well as the higher-order multiple scattering processes must be included in the calculations in order to have a better understanding of the deuteron breakup reaction, especially in the region where q is greater than 150 MeV/c.

APPENDIX A

The Madison Convention

The Third International Symposium on Polarization Phenomena in Nuclear Reaction was held at the University of Wisconsin, Madison between August 31 and September 4, 1970. For several months before the symposium, a number of participants discussed the need for conventions concerning notations and coordinate systems for describing polarization phenomena, especially for spin-one particles. During the symposium, about twenty-five physicists met and worked on this subject. The recommendations of this working group were presented to the whole conference and were accepted without dissent. P. Huber proposed that these recommendations be called "The Madison Convention," and this proposal was adopted unanimously. The followings are the substance of the Madison Convention [BH71].

I

Polarization effects involving spin-one particles should be described either by spherical tensor operators τ_{kq} , with normalization given by $Tr\{\tau_{kq}\tau_{k'q'}^\dagger\} = 3\delta_{kk'}\delta_{qq'}$ or by Cartesian operator S_i , $(3/2)(S_iS_j + S_jS_i) - 2\delta_{ij}$ ($i = x, y, z$). S_i denotes the usual spin-one angular momentum operators.

II

The state of spin orientation of an assembly of particles, referred to as *polarization*, should be denoted by the symbols t_{kq} (spherical) or p_i, p_{ij} (Cartesian). These quantities should be referred to a right-handed coordinate system in which the positive z -axis is along the direction of momentum of the particles, and the positive y -axis is along

$\vec{k}_{in} \times \vec{k}_{out}$ for the nuclear reaction which the polarized particles initiate, or from which they emerge.

III

Terms used to describe the effect of initial polarization of a beam or target on the differential cross section for a nuclear reaction should include the modifiers *analyzing* or *efficiency*, and should be denoted by T_{kq} (spherical) or A_i, A_{ij} (Cartesian). These quantities should be referred to a right-handed coordinate system in which the positive z -axis is along the beam direction of the incident particles and the y -axis is along $\vec{k}_{in} \times \vec{k}_{out}$ for the reaction in question.

IV

In the expression for a nuclear reaction $A(b, c)D$ an arrow placed over a symbol denotes a particle which is initially in a polarized state or whose state of polarization is measured.

□ □ □ □ □ □

Beside the Madison Convention, some other slightly different notations are also being used. For instance, in this thesis, capital P_i and P_{ij} are used to denote the polarization in Cartesian coordinate while p_i are reserved for momenta.

Based on the above guide lines, the reactions involving polarization can be divided into the following classes:

- (i) $A(b, \vec{c})D$ polarization experiment
- (ii) $A(\vec{b}, c)D$ analyzing power experiment
- (iii) $A(\vec{b}, \vec{c})D$ polarization transfer
- (iv) $\vec{A}(\vec{b}, c)D$ spin correlation (initial channel)
- (v) $A(b, \vec{c}\vec{D})$ spin correlation (final channel).

In discussing polarization effects involving spin-one particles, either spherical tensors or Cartesian tensors should be used. The set of Cartesian tensor operators are given below in terms of the spin-one angular momentum operators and unit matrix.

$$I = \begin{pmatrix} 1 & 0 & 0 \\ 0 & 1 & 0 \\ 0 & 0 & 1 \end{pmatrix}; S_x = \frac{1}{\sqrt{2}} \begin{pmatrix} 0 & 1 & 0 \\ 1 & 0 & 1 \\ 0 & 1 & 0 \end{pmatrix}; S_y = \frac{1}{\sqrt{2}} \begin{pmatrix} 0 & -i & 0 \\ i & 0 & -i \\ 0 & i & 0 \end{pmatrix}; S_z = \begin{pmatrix} 1 & 0 & 0 \\ 0 & 0 & 0 \\ 0 & 0 & -1 \end{pmatrix}$$

Cartesian Operators

$$\begin{aligned} \mathcal{P}_0 &= I & \mathcal{P}_{xy} &= \frac{3}{2}(S_x S_y + S_y S_x) \\ \mathcal{P}_x &= S_x & \mathcal{P}_{xz} &= \frac{3}{2}(S_x S_z + S_z S_x) \\ \mathcal{P}_y &= S_y & \mathcal{P}_{yz} &= \frac{3}{2}(S_y S_z + S_z S_y) \\ \mathcal{P}_z &= S_z & \frac{1}{2}(\mathcal{P}_{xx} - \mathcal{P}_{yy}) &= \frac{3}{2}(S_x S_x - S_y S_y) - 2I \\ & & \mathcal{P}_{zz} &= 3S_z S_z - 2I \end{aligned} \tag{A-1}$$

The relationships between the spherical and Cartesian tensor operators are given by

Spherical Operators

Cartesian Operators

$$\begin{aligned} \tau_{00} &= I & \mathcal{P}_0 &= I \\ \tau_{10} &= \sqrt{\frac{3}{2}}\mathcal{P}_z & \mathcal{P}_x &= -\frac{2}{\sqrt{3}}\text{Re}\tau_{11} \\ \tau_{11} &= -\frac{\sqrt{3}}{2}(\mathcal{P}_x + i\mathcal{P}_y) & \mathcal{P}_y &= -\frac{2}{\sqrt{3}}\text{Im}\tau_{11} \\ \tau_{20} &= \frac{1}{\sqrt{2}}\mathcal{P}_{zz} & \mathcal{P}_z &= \sqrt{\frac{2}{3}}\tau_{10} \\ \tau_{21} &= -\frac{1}{\sqrt{3}}(\mathcal{P}_{xz} + i\mathcal{P}_{yz}) & \mathcal{P}_{xy} &= \sqrt{3}\text{Im}\tau_{22} \\ \tau_{22} &= \frac{1}{2\sqrt{3}}(\mathcal{P}_{xx} - \mathcal{P}_{yy} + 2i\mathcal{P}_{xy}) & \mathcal{P}_{xz} &= -\sqrt{3}\text{Re}\tau_{21} \\ & & \mathcal{P}_{yz} &= -\sqrt{3}\text{Im}\tau_{21} \\ \tau_{k-q} &= (-1)^q \tau_{kq}^* & \frac{1}{2}(\mathcal{P}_{xx} - \mathcal{P}_{yy}) &= \sqrt{3}\text{Re}\tau_{22} \\ & & \mathcal{P}_{zz} &= \sqrt{2}\tau_{20} \end{aligned} \tag{A-2}$$

In the *beam polarization coordinate system* ($\mathcal{X}, \mathcal{Y}, \mathcal{Z}$), where the polarization axis of the beam, \hat{s} , is chosen to be the \mathcal{Z} -axis and the \mathcal{X} - and \mathcal{Y} -axes are arbitrary, the polarization can be completely determined by two quantities. They are the \mathcal{P}_z and

P_{ZZ} . In the spherical tensor representation the corresponding quantities are ρ_{10} and ρ_{20} . They are related as:

Spherical Polarization	Cartesian Polarization	
$\rho_{10} = \sqrt{\frac{3}{2}}P_Z$	$P_Z = \sqrt{\frac{2}{3}}\rho_{10}$	(A-3)
$\rho_{20} = \frac{1}{\sqrt{2}}P_{ZZ}$	$P_{ZZ} = \sqrt{2}\rho_{20}$	

The Madison Convention chooses the coordinate systems that depend on the particle trajectories and the scattering angles. For particles scattered into different directions, the coordinate systems used to describe the reaction will be different. According to this convention, the positive z -axis is along the direction of the incoming particle momentum, \vec{k}_{in} . The positive y -axis is along $\vec{k}_{in} \times \vec{k}_{out}$, where \vec{k}_{out} is the outgoing particle momentum, it should be explicitly stated whether it is in c.m. or lab. system. The x -axis is determined by $\hat{y} \times \hat{z}$. This coordinate system, denoted by (x,y,z) in Figure A-1, is used when describing the polarization of the incoming particles, and is called the *projectile helicity coordinate system*.

Another coordinate system (x',y',z') is used to describe the polarization of the outgoing particle. The z' -axis of this *outgoing reactant helicity coordinate system* is along \vec{k}_{out} , and the y' -axis is in the same direction as y -axis. The x' -axis is chosen to form a right handed coordinate system.

Meanwhile, if a polarized beam is used in the experiment and the polarization symmetry axis of the incoming particles, \hat{s} , is fixed in the laboratory frame, we can define a *laboratory coordinate system* with z_{lab} -axis along \vec{k}_{in} , and \hat{s} lies on the $y_{lab}-z_{lab}$ plane. This laboratory coordinate system is shown in Figure A-1 as $(x_{lab},y_{lab},z_{lab})$. Unlike the projectile helicity frame, the lab. frame is fixed for all particles regardless of their scattering angles.

The angle between the polarization axis \hat{s} and the z_{lab} -axis is labeled as β in Figure A-1. The azimuthal angle, ϕ , is defined by the Madison Convention to be the angle

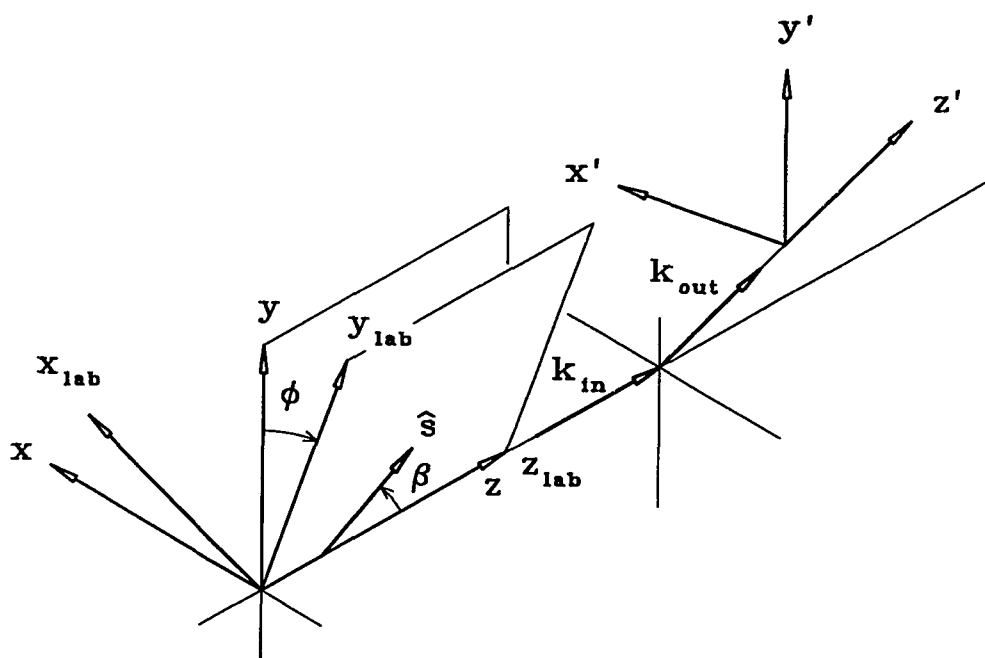


Figure A-1: Relationship between the projectile helicity frame (x, y, z) , the outgoing reactant helicity frame (x', y', z') and the lab. frame $(x_{lab}, y_{lab}, z_{lab})$.

direction of the scattered particle in lab. frame	azimuthal angle ϕ	
	in Madison Convention	in spherical coordinates
left	0°	0°
up	270°	90°
right	180°	180°
down	90°	270°

Table A-1: Comparison of ϕ between the Madison Convention and the usual spherical coordinates.

measured from the y -axis to the y_{lab} -axis. This definition of ϕ is different from the usual spherical coordinate system. The comparison of the values of ϕ between the two systems when the particle is scattered to the left, up, right and down, respectively, in the lab. frame is given in Table A-1.

In the beam polarization coordinate system, $(\mathcal{X}, \mathcal{Y}, \mathcal{Z})$, the beam polarization is described by ρ_{10} and ρ_{20} . In the projectile helicity frame, (x, y, z) , the polarization becomes [Dar70, Hae74]

$$\begin{array}{ll}
 \text{Vector Polarization} & \text{Tensor Polarization} \\
 t_{10} = \rho_{10} \cos \beta & t_{20} = \frac{1}{2} \rho_{20} (3 \cos^2 \beta - 1) \\
 t_{11} = -i \frac{1}{\sqrt{2}} \rho_{10} \sin \beta e^{i\phi} & t_{21} = -i \sqrt{\frac{3}{2}} \rho_{20} \sin \beta \cos \beta e^{i\phi} \\
 & t_{22} = -\sqrt{\frac{3}{8}} \rho_{20} \sin^2 \beta e^{2i\phi}
 \end{array} \tag{A-4}$$

In Cartesian coordinates, one has [Ohl72]

$$\begin{array}{ll}
 \text{Vector Polarization} & \text{Tensor Polarization} \\
 P_x = -P_Z \sin \beta \sin \phi & P_{xy} = -\frac{3}{4} P_{ZZ} \sin^2 \beta \sin 2\phi \\
 P_y = P_Z \sin \beta \cos \phi & P_{xz} = -\frac{3}{2} P_{ZZ} \sin \beta \cos \beta \sin \phi \\
 P_z = P_Z \cos \beta & P_{yz} = \frac{3}{2} P_{ZZ} \sin \beta \cos \beta \cos \phi \\
 & \frac{1}{2} (P_{xx} - P_{yy}) = -\frac{3}{4} P_{ZZ} \sin^2 \beta \cos 2\phi \\
 & P_{zz} = \frac{1}{2} P_{ZZ} (3 \cos^2 \beta - 1)
 \end{array} \tag{A-5}$$

The most general form for the cross section of a reaction induced by polarized spin-1 particles is

$$\begin{aligned}
I(\theta, \phi) = I_o(\theta) & \left[1 + \frac{3}{2}P_x A_x(\theta) + \frac{3}{2}P_y A_y(\theta) + \frac{3}{2}P_z A_z(\theta) \right. \\
& + \frac{2}{3}P_{xy} A_{xy}(\theta) + \frac{2}{3}P_{xz} A_{xz}(\theta) + \frac{2}{3}P_{yz} A_{yz}(\theta) \\
& \left. + \frac{1}{6}(P_{xx} - P_{yy})(A_{xx}(\theta) - A_{yy}(\theta)) + \frac{1}{2}P_{zz} A_{zz}(\theta) \right], \tag{A-6}
\end{aligned}$$

where I_o is the cross section for an unpolarized beam, and A 's are the analyzing powers of the reaction. The ϕ -dependence of the cross section is contained in P_i and P_{ij} as described in Equation A-5. In terms of spherical tensors, the cross section is given by

$$\begin{aligned}
I(\theta, \phi) = I_o(\theta) & \left[1 + t_{10}T_{10}(\theta) + 2\text{Re}t_{11}\text{Re}T_{11}(\theta) + 2\text{Im}t_{11}\text{Im}T_{11}(\theta) \right. \\
& + t_{20}T_{20}(\theta) + 2\text{Re}t_{21}\text{Re}T_{21}(\theta) + 2\text{Im}t_{21}\text{Im}T_{21}(\theta) \\
& \left. + 2\text{Re}t_{22}\text{Re}T_{22}(\theta) + 2\text{Im}t_{22}\text{Im}T_{22}(\theta) \right]. \tag{A-7}
\end{aligned}$$

The T_{qk} are the analyzing powers in the spherical tensors representation. The relationships between the T_{qk} 's and A 's are similar to those between their corresponding operators in Equation A-2.

Spherical Analyzing Power	Cartesian Analyzing Power	
$T_{10} = \sqrt{\frac{3}{2}}A_z$	$A_x = -\frac{2}{\sqrt{3}}\text{Re}T_{11}$	
$T_{11} = -\frac{\sqrt{3}}{2}(A_x + iA_y)$	$A_y = -\frac{2}{\sqrt{3}}\text{Im}T_{11}$	
$T_{20} = \frac{1}{\sqrt{2}}A_{zz}$	$A_z = \sqrt{\frac{2}{3}}T_{10}$	
$T_{21} = -\frac{1}{\sqrt{3}}(A_{xz} + iA_{yz})$	$A_{xy} = \sqrt{3}\text{Im}T_{22}$	(A-8)
$T_{22} = \frac{1}{2\sqrt{3}}(A_{xx} - A_{yy} + 2iA_{xy})$	$A_{xz} = -\sqrt{3}\text{Re}T_{21}$	
	$A_{yz} = -\sqrt{3}\text{Im}T_{21}$	
$T_{k-q} = (-1)^q T_{kq}^*$	$\frac{1}{2}(A_{xx} - A_{yy}) = \sqrt{3}\text{Re}T_{22}$	
	$A_{zz} = \sqrt{2}T_{20}$	

For a nuclear reaction, conservation of parity requires some of those analyzing powers to vanish and the expression becomes

$$I(\theta, \phi) = I_o(\theta) \left[1 + \frac{3}{2} P_y \underline{A_y}(\theta) + \frac{2}{3} P_{xz} \underline{A_{xz}}(\theta) + \frac{1}{6} (P_{xx} - P_{yy})(A_{xx}(\theta) - A_{yy}(\theta)) + \frac{1}{2} P_{zz} A_{zz}(\theta) \right]. \quad (\text{A-9})$$

The underlined coefficients are odd in the scattering angle θ . It means that those terms are zero when $\theta = 0$. Under the same parity conservation requirement, the polarization of the outgoing protons from the (\vec{d}, \vec{p}) reaction is given by

$$\begin{aligned} P_{x'} I(\theta, \phi) &= I_o(\theta) \left[\frac{3}{2} P_x \underline{\mathcal{K}_x^{x'}}(\theta) + \frac{3}{2} P_z \underline{\mathcal{K}_z^{x'}}(\theta) + \frac{2}{3} P_{xy} \underline{\mathcal{K}_{xy}^{x'}}(\theta) + \frac{2}{3} P_{yz} \underline{\mathcal{K}_{yz}^{x'}}(\theta) \right] \\ P_{y'} I(\theta, \phi) &= I_o(\theta) \left[\underline{\mathcal{P}_{y'}} + \frac{3}{2} P_y \underline{\mathcal{K}_y^{y'}}(\theta) + \frac{2}{3} P_{xz} \underline{\mathcal{K}_{xz}^{y'}}(\theta) + \frac{1}{6} (P_{xx} - P_{yy})(\underline{\mathcal{K}_{xx}^{y'}}(\theta) - \underline{\mathcal{K}_{yy}^{y'}}(\theta)) + \frac{1}{2} P_{zz} \underline{\mathcal{K}_{zz}^{y'}}(\theta) \right] \\ P_{z'} I(\theta, \phi) &= I_o(\theta) \left[\frac{3}{2} P_x \underline{\mathcal{K}_x^{z'}}(\theta) + \frac{3}{2} P_z \underline{\mathcal{K}_z^{z'}}(\theta) + \frac{2}{3} P_{xy} \underline{\mathcal{K}_{xy}^{z'}}(\theta) + \frac{2}{3} P_{yz} \underline{\mathcal{K}_{yz}^{z'}}(\theta) \right], \end{aligned} \quad (\text{A-10})$$

where \mathcal{K} 's are the polarization transfer coefficients, and $\mathcal{P}_{y'}$ is the polarization of the outgoing spin-1/2 particles for an unpolarized incident beam. The polarization of the protons is measured in the corresponding outgoing reactant helicity frame, (x', y', z') . Again, the underlined coefficients are odd in θ .

For the deuteron breakup experiment (\vec{d}, \vec{p}) discussed in this dissertation, the polarization symmetry axis of the incident deuterons was perpendicular to the beam momentum direction so that the angle β , shown in Figure A-1, was equal to 90° . The emerging protons were measured at $\theta = 0^\circ$. Introducing these conditions into Equation A-5, and substituting the results into Equation A-9 and A-10, the cross section and the proton polarization become

$$\begin{aligned} I &= I_o \left[1 - \frac{1}{4} P_{ZZ} (A_{zz} - (A_{xx} - A_{yy}) \cos 2\phi) \right] \\ P_{x'} I &= I_o \left[-\frac{3}{2} P_Z \underline{\mathcal{K}_x^{x'}} \sin \phi \right] \\ P_{y'} I &= I_o \left[\frac{3}{2} P_Z \underline{\mathcal{K}_y^{y'}} \cos \phi \right] \end{aligned} \quad (\text{A-11})$$

$$P_{z'}I = I_0[-\frac{1}{2}P_{ZZ}\mathcal{K}_{xy}^{z'} \sin 2\phi].$$

Since θ is 0° for this experiment, ϕ is not defined and we can use any value for it. The cross section of this particular breakup reaction should not dependent on how we define ϕ . This implies $A_{xx} = A_{yy}$ when $\theta = 0^\circ$.

We pick $\phi = 0$ for obvious convenience. Together with $\theta = 0$ and $\beta = 90^\circ$, the three coordinate systems, $(x, y, z), (x', y', z')$ and $(x_{lab}, y_{lab}, z_{lab})$, are all overlapping with each others. Then, Equation A-11 becomes

$$\begin{aligned} I &= I_0[1 - \frac{1}{4}P_{ZZ}A_{zz}] \\ P_{x'}I &= 0 \\ P_{y'}I &= I_0[\frac{3}{2}P_Z\mathcal{K}_y^{y'}] \\ P_{z'}I &= 0 \end{aligned} \tag{A-12}$$

In this thesis, we define the ratio between the proton polarization, $P_{y'}$, and the deuteron vector polarization, P_Z , to be κ , such that

$$\kappa = \frac{P_{y'}}{P_Z} = \frac{\frac{3}{2}\mathcal{K}_y^{y'}}{1 - \frac{1}{4}P_{ZZ}A_{zz}} = \frac{\frac{3}{2}\mathcal{K}_y^{y'}}{1 - \frac{1}{2}T_{20}\rho_{20}}. \tag{A-13}$$

When $P_{ZZ} = 0$, as in this experiment, we can define

$$\kappa_0 = \kappa|_{P_{ZZ}=0} = \frac{3}{2}\mathcal{K}_y^{y'} \tag{A-14}$$

APPENDIX B

Dead-time correction for the deuteron beam polarimeter

After the deuteron ions are being produced in the polarized source, their polarization is measured in the deuteron beam polarimeter (DBP). The analyzing reaction used is ${}^2H(\vec{d}, p){}^3H$ with the incoming deuteron energy equal to 386 keV. The beam enters the polarimeter through a collimator with an circular opening of 10mm in diameter. The outgoing protons are detected at 0° and $\pm 120^\circ$ with silicon detectors as shown in Figure 2-7. The number of protons scattered into the two 120° detectors, located at left and right, are given by:

$$\begin{aligned}n_L &= n_o(1 + \epsilon) \\n_R &= n_o(1 - \epsilon),\end{aligned}\tag{B-1}$$

where ϵ is the asymmetry given by

$$\epsilon = \frac{n_L - n_R}{n_L + n_R}$$

and n_o is the number of particles per burst scattered towards the 120° detector for an unpolarized deuteron beam. The number of counts detected by the detectors are given by:

$$\begin{aligned}m_L &= n_L \exp(-n_L \frac{\tau}{T}) \\m_R &= n_R \exp(-n_R \frac{\tau}{T}),\end{aligned}\tag{B-2}$$

where τ is the dead-time of the detector after being hit by a proton, and T is the duration of the beam burst. For the deuteron beam polarimeter at Saturne, τ was measured to be $2.78 \pm 0.79 \mu\text{s}$ and T is about 1 ms.

The measured asymmetry is defined as

$$\begin{aligned}
 x_m &\equiv \frac{m_L - m_R}{m_L + m_R} \\
 &= \frac{n_L \exp(-n_L \frac{\tau}{T}) - n_R \exp(-n_R \frac{\tau}{T})}{n_L \exp(-n_L \frac{\tau}{T}) + n_R \exp(-n_R \frac{\tau}{T})} \\
 &= \frac{[\exp(-\epsilon n_o \frac{\tau}{T}) - \exp(+\epsilon n_o \frac{\tau}{T})] + \epsilon [\exp(-\epsilon n_o \frac{\tau}{T}) + \exp(+\epsilon n_o \frac{\tau}{T})]}{\epsilon [\exp(-\epsilon n_o \frac{\tau}{T}) - \exp(+\epsilon n_o \frac{\tau}{T})] + [\exp(-\epsilon n_o \frac{\tau}{T}) + \exp(+\epsilon n_o \frac{\tau}{T})]} \quad (\text{B-3})
 \end{aligned}$$

For the cases when $\epsilon n_o \frac{\tau}{T} \ll 1$,

$$\exp(-\epsilon n_o \frac{\tau}{T}) \approx 1 - \epsilon n_o \frac{\tau}{T} + \frac{1}{2!} (\epsilon n_o \frac{\tau}{T})^2 - \frac{1}{3!} (\epsilon n_o \frac{\tau}{T})^3 \quad (\text{B-4})$$

$$\exp(+\epsilon n_o \frac{\tau}{T}) \approx 1 + \epsilon n_o \frac{\tau}{T} + \frac{1}{2!} (\epsilon n_o \frac{\tau}{T})^2 + \frac{1}{3!} (\epsilon n_o \frac{\tau}{T})^3. \quad (\text{B-5})$$

Keeping only the terms up to the second order of ϵ , Equation B-3 becomes

$$\begin{aligned}
 x_m &= \frac{\epsilon(1 - n_o \frac{\tau}{T})}{1 - \epsilon^2 (n_o \frac{\tau}{T})(1 - \frac{1}{2} n_o \frac{\tau}{T})} \\
 \epsilon^2 [(n_o \frac{\tau}{T})(1 - \frac{1}{2} n_o \frac{\tau}{T}) x_m] + \epsilon [(1 - n_o \frac{\tau}{T})] - x_m &= 0 \quad (\text{B-6})
 \end{aligned}$$

The ratios between x_m and ϵ for different values of n_o are given in Figure B-1.

The deuteron beam polarimeter was calibrated by J. Arvieux, et al. and the result was published in 1988 [A⁺88]. The measured $(iT_{11}P_Z)_m$ was 0.1139 ± 0.0016 . Since

$$x_m = \sqrt{3}(iT_{11}P_Z)_m, \quad (\text{B-7})$$

that means that x_m was 0.1973 ± 0.0028 . The counting rates for their calibration experiment were of the order of 50 counts per beam burst in the 0° detector and 25 counts per burst in the $\pm 120^\circ$ detectors. The dead time correction had not been taken into account in the 1988 published calibration result. We re-analyzed the experiment and corrected for the dead time. With

$$n_o \approx 25$$

$$x_m = 0.1973 \pm 0.0028$$

$$\frac{\tau}{T} = 2.78 \times 10^{-3},$$

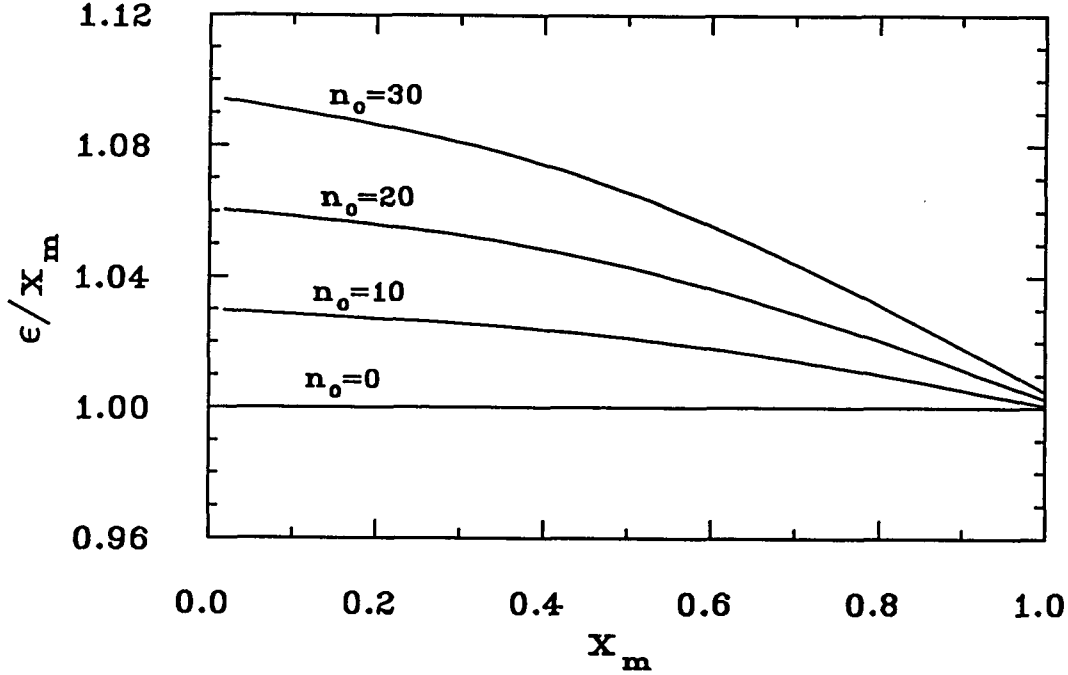


Figure B-1: Ratio between the true asymmetry, ϵ , and the measured asymmetry, x_m .

we have

$$\begin{aligned} \epsilon &\approx 1.07x_m \\ &= 0.2114 \pm 0.0030 \end{aligned} \quad (\text{B-8})$$

In Arvieux's experiment, the deuteron beam vector polarization, P_Z , was measured by means of the pp quasi-free deuteron breakup reaction, $p(\vec{d}, 2p)$ at $T_d = 1.45$ GeV. A high energy proton polarimeter was setup to measure the pp quasi-elastic scattering and to determine the proton polarization, P_N . P_N was measured to be 0.5775 ± 0.061 . Assuming that the momentum distribution of the bound proton inside the deuteron nucleus followed the Paris potential wave function, one has

$$P_N = \alpha P_Z. \quad (\text{B-9})$$

After taking into account the solid angle of the detectors, α was calculated to be 0.98 ± 0.01 . This gives $P_Z = 0.5889 \pm 0.0086$.

With

$$\epsilon = \frac{3}{2} A_{DBP} P_Z, \quad (\text{B-10})$$

we have

$$A_{DBP} = 0.2393 \pm 0.0049, \quad (\text{B-11})$$

compared with the published value of 0.2234 ± 0.0046 , which does not include the dead-time correction.

References

- [A⁺84] J. Arvieux et al. Elastic scattering of polarized deuterons by protons at intermediate energies. *Nuclear Instruments and Methods in Physics Research*, A 431:613–636, 1984.
- [A⁺88] J. Arvieux et al. Deuteron polarimetry studies at low and intermediate energies. *Nuclear Instruments and Methods in Physics Research*, A 273:48–58, 1988.
- [Arn88] R.C. Arndt. Uncertainties in the np interaction at medium energies. *Physical Review D*, 37(9):2665–2667, 1988.
- [B⁺87] M. Bedjidian et al. A detection system using drift chambers for the SPES4 spectrometer at Laboratoire National Saturne. *Nuclear Instruments and Methods in Physics Research*, A 257:132–138, 1987.
- [B⁺90] B. Bonin et al. Measurement of the inclusive p-C analyzing power and cross section in the 1 GeV region and calibration of the new polarimeter POMME. *Nuclear Instruments and Methods in Physics Research*, A 288:379–388, 1990.
- [Bet53] Hans Bethe. What holds the nucleus together? *Scientific American*, 189(3):58–63, 1953.
- [BG79] W.W. Buck and Franz Gross. Family of relativistic deuteron wave functions. *Physical Review D*, 20(9):2361–2379, 1979.
- [BH71] H.H. Barschall and W. Haeberli, editors. *1970 Proc. 3rd Int. Symp. on Polarization Phenomena in Nuclear Reactions*, pages xxv–xxix. Madison, University of Wisconsin Press, first edition, 1971.
- [BS57] R.J. Blin-Stoyle. *Theories of nuclear moments*, page 5. Oxford University Press, Oxford University Press, Amen House, London, E.C.4, first edition, 1957.
- [C⁺90] P.A. Chamouard et al. Saturne latest results for polarized beams. In A. Boudard and Y. Terrien, editors, *Colloque de Physique*, pages 569–572, 1990. International conference on polarization phenomena in nuclear physics (7th: 1990: Paris, France).
- [C⁺92] E. Cheung et al. Polarization transfer in $^1\text{H}(\vec{d}, \vec{p})X$ at 2.1 GeV. *Physics Letters*, B 284:210–214, 1992.
- [Dar70] S.E. Darden. Description of polarization and suggestions for additional conventions. In H.H. Barschall and W. Haeberli, editors, *Polarization Phenomena in Nuclear Reaction; proceedings*, pages 39–56, 1970. International Symposium on Polarization Phenomena in Nuclear Reactions (3rd: 1970: University of Wisconsin).
- [DB89] H. Dijk and B.L.G. Baller. Multiquark effect in the 1S_0 and $^3S_1 - ^3D_1$ neutron-proton scattering states and the deuteron. *Nuclear Physics*, A 494:438, 1989.

- [DL90] M.G. Dolidze and G.I. Lykasov. Sensitivity of t_{20} in $dA \rightarrow pX$ to the reaction mechanism and relativistic effects. *Zeitschrift fur Physik, A* 336:339–344, 1990.
- [DL92] Yu. L. Dorodnykh and G. I. Lykasov. Fragmentation process of the deuteron and its structure at small N-N distances. Russian Academy of Sciences (preprint INR - 781/92), 1992.
- [FL91] H. Fanet and J.C. Lugol. Measurement of charge with an active integrator in the presence of noise and pileup effects. *Nuclear Instruments and Methods in Physics Research, A* 301:295–304, 1991.
- [G⁺80] W. Gruebler et al. Determination of the asymptotic D- to S-state normalization of the deuteron wave function. *Physics Letters, B* 92:279–282, 1980.
- [G⁺81] E. Grorud et al. Performance of a 4 GeV/c magnetic spectrograph taking advantage of the third integral resonant extraction properties to operate in the energy loss mode. *Nuclear Instruments and Methods in Physics Research*, 188:549–554, 1981.
- [G⁺86] G.L. Greene et al. New determination of the deuteron binding energy and the neutron mass. *Physical Review Letter*, 56(8):819–822, 1986.
- [Gla70] H.F. Glavish. Atomic beam sources. In H.H. Barschall and W. Haeberli, editors, *Polarization Phenomena in Nuclear Reaction; proceedings*, pages 267–291, 1970. International Symposium on Polarization Phenomena in Nuclear Reactions (3rd: 1970: University of Wisconsin).
- [GOH92] Franz Gross, J.W. Van Orden, and Karl Holinde. Relativistic one-boson-exchange model for the nucleon-nucleon interaction. *Physical Review C*, 45(5):2094–2132, 1992.
- [Hae74] W. Haeberli. Polarized beams. In Joseph Cerny, editor, *Nuclear Spectroscopy and Reactions, Part A*, pages 151–191. Academic Press, Inc., 1974.
- [Hei32] W. Heisenberg. Structure of atomic nuclei: part I. *Zeits. f. Physik*, 77:1–11, 1932.
- [K⁺85] V.M. Krasnopol'sky et al. The deuteron structure and NN-phase shifts for realistic local superdeep NN-potential with an extra state. *Physics Letters, B* 165:7, 1985.
- [KPS93] B. Kuhn, C.F. Perdrisat, and E.A. Strokovsky. Correlations between polarization observables in inclusive deuteron breakup. to be published in Proc. of the 1993 Dubna Deuteron Symposium, 1993.
- [L⁺80] M. Lacombe et al. Parameterization of the Paris N-N potential. *Physical Review C*, 21(3):861–873, 1980.
- [L⁺81] M. Lacombe et al. Parameterization of the deuteron wave function of the Paris N-N potential. *Physics Letters, B* 101:139–140, 1981.

- [Lem90] J.L. Lemaire. Present result on the polarized proton and deuteron source at Saturne (LNS-Saclay). In *Proceedings of the international workshop on polarized ion source and polarized gas jet*, pages 116–137, 1990. Workshop on the polarized sources, KEK, Tsukuba, Japan.
- [Lev60] J.S. Levinger. *Nuclear photo-disintegration*, page 47. Oxford University Press, Oxford University Press, Amen House, London, E.C.4, first edition, 1960.
- [Mac89] R. Machleidt. The meson theory of nuclear forces and nuclear structure. In J.W. Negele and Erich Vogt, editors, *Advances in Nuclear Physics*, pages 189–376. 1989 Plenum Press, New York, 1989. vol. 19.
- [Mul90] H. Muller. Deuteron fragmentation $d + A \rightarrow p + X$ at relativistic energies and the role of particle production processes. *Zeitschrift fur Physik, A* 336:103–112, 1990.
- [Mul91] H. Muller. Deuteron fragmentation $d + A \rightarrow p + X$ at relativistic energies and the role of the target nucleus. *Zeitschrift fur Physik, A* 339:409–415, 1991.
- [Nii90] T.O. Niinikoski. Polarized sources. In A. Boudard and Y. Terrien, editors, *Colloque de Physique*, pages 191–203, 1990. International conference on polarization phenomena in nuclear physics (7th: 1990: Paris, France).
- [Ohl72] G.G. Ohlsen. Polarization transfer and spin correlation experiments in nuclear physics. *Rep. Prog. Phys.*, 35:717–801, 1972.
- [P+89] V. Punjabi et al. Deuteron breakup at 2.1 and 1.25 GeV. *Physical Review C*, 39(2):608–618, 1989.
- [P+93] C.F. Perdrisat et al. Polarization observables in elastic backward $dp \rightarrow dp$ scattering. *News from Saturne*, 17:104–105, 1993.
- [PP90] C.F. Perdrisat and V. Punjabi. Deuteron structure from $(p, 2p)$ and (d, p) breakup data at medium energies. *Physical Review C*, 42(5):1889–1910, 1990.
- [Rei68] R.V. Reid Jr. Local phenomenological nucleon-nucleon potentials. *Ann. of Phys.*, 50:411–418, 1968.
- [Sat87] Laboratoire National Saturne. *Saturne*. Laboratoire National Saturne, 91191 Gif-sur-Yvette Cedex France, 1987.
- [Sat90] Laboratoire National Saturne. *SARI manual*. Laboratoire National Saturne, 91191 Gif-sur-Yvette Cedex France, 1990.
- [TG92a] E. Tomasi-Gustafsson. *Analyzing power fit for POMME*, 1992. private communication.
- [TG92b] E. Tomasi-Gustafsson. *POMME - Polarimetre Mobile Moyenne Energie manual*. Laboratoire National Saturne, 91191 Gif-sur-Yvette Cedex France, 1992. LNS/Ph/92-07 Centre National de la Recherche Scientifique.
- [Won90] Samuel S. M. Wong. *Introductory Nuclear Physics*, page 66. Prentice Hall, Inc., Englewood Cliffs, New Jersey 07632, first edition, 1990.

VITA

Naipor Eric Cheung

Cheung was born in Hong Kong on April 29, 1963. Graduated from Kwun Tong Government Secondary Technical School, in that city in June, 1982. Received an Honours Diploma in Physics from the Hong Kong Baptist College in May, 1985. In August of 1986, he began his graduate studies at the College of William and Mary in Virginia.